Stability and Kinetics Enhancement of Hydrated Vanadium Oxides via Chemical Pre-intercalation for Aqueous Zinc-Ion Batteries

Xiaoxiao Jia

A dissertation

submitted in partial fulfillment of the

requirements for the degree of

Doctor of Philosophy

University of Washington

2024

Reading Committee:

Guozhong Cao, Chair

Jun Liu

Bo Zhang

Program Authorized to Offer Degree:

Materials Science and Engineering

University of Washington

Abstract

Stability and Kinetics Enhancement of Hydrated Vanadium Oxides via Chemical Pre-intercalation for Aqueous Zinc-Ion Batteries

Xiaoxiao Jia

Chair of the Supervisory Committee:
Guozhong Cao
Department of Materials Science and Engineering

Aqueous zinc ion batteries (ZIBs) are promising candidates for large-scale energy storage due to their cost-effectiveness, environmental friendliness, intrinsic safety, and competitive energy density. However, strong electrostatic interactions between divalent zinc ions and host materials pose challenges for transport kinetics and structural stability during cycling. This dissertation investigates the enhancement of hydrated vanadium oxides ($V_2O_5 \cdot nH_2O$, VOH) as cathode materials for ZIBs through chemical pre-intercalation strategies. The focus is on understanding the mechanisms and benefits of chemical pre-intercalation, as well as identifying key factors determining pre-intercalation effects and influencing overall electrochemical performance for both metal and organic cation pre-intercalated vanadium oxides. The modified VOH usually shows increased capacity, reduced voltage polarization, improved rate capability, and enhanced electrochemical

reversibility and stability. Key findings include: (1) metal cations can be favorably intercalated into the VOH structure, replacing hydrogen bonded water (H_3O^+) between bilayers, resulting in changes in interlayer distance, structure water amount, and V^{4+} content. (2) The formation of additional chemical bonds between pre-intercalated metal cations and the V–O lattice contributes to the improved structural and electrochemical stability. (3) Pre-inserting organic cations (trimethylphenylammonium, $TMPA^+$) benefits the effects of both ionic and molecular pre-intercalation, reducing electrostatic interactions between Zn^{2+} and the V–O lattice, improving structural stability and reaction kinetics during cycling. (4) Interlayer spacing of metal cation pre-intercalated $M_xV_2O_5{\cdot}nH_2O$ materials is influenced by interlayer water content/hydration number, while interlayer spacing of organic cation pre-intercalated $(Org)_xV_8O_{20}{\cdot}nH_2O$ materials is determined by the ionic radius of organic cations. (5) No direct correlations exist between interlayer spacing and cycling stability or rate performance for both $M_xV_2O_5{\cdot}nH_2O$ and $(Org)_xV_8O_{20}{\cdot}nH_2O$ materials. (6) The electrochemical stability and kinetics of $(Org)_xV_8O_{20}{\cdot}nH_2O$ are primarily influenced by the polarity of organic cations. Weaker-polarized methylammonium (MA^+) ions facilitate easier Zn^{2+} ion transport, similar to singly charged ion-stabilized VOH; while the effects of stronger-polarized tetramethylammonium (TMA^+) ions align more closely with Mg^{2+} and Al^{3+} ions, which exert stronger electrostatic interactions with Zn^{2+} ions.

TABLE OF CONTENTS

LIST OF FIGURES

LIST OF TABLES

ACKNOWLEDGEMENTS

As I conclude this final chapter of my academic journey, I would like to express my deepest gratitude to my principal investigator, Prof. Guozhong Cao, for his invaluable guidance, support, and encouragement. Without his mentorship, my time at UW would not have been so wonderful and rewarding.

I am also grateful to my committee members, Prof. Jun Liu, Prof. Gerald Seidler, and Prof. Bo Zhang, for their constructive feedback and encouragement.

Special thanks to my colleagues and friends in the Cao Lab, especially Dr. Chaofeng Liu, for creating a collaborative and inspiring environment.

My heartfelt thanks go to my family for their unconditional love and encouragement. Their belief in me has been my source of strength and motivation, making this achievement possible.

Lastly, I am grateful for every moment I've experienced, every scenery I've seen, and every person I've met along this journey. Thank you all for being a part of shaping who I am today.

Chapter 1. Introduction

Adapted with permission from Xiaoxiao Jia, Chaofeng Liu, Zachary G. Neale, Jihui Yang, and Guozhong Cao. "Active Materials for Aqueous Zinc Ion Batteries: Synthesis, Crystal Structure, Morphology, and Electrochemistry." *Chemical Reviews* 120, 15, 7795–7866 (2020). https://doi.org/10.1021/acs.chemrev.9b00628.

1.1 Overview of Aqueous Zn-ion Batteries

1.1.1 *Electrical Energy Storage Systems: Background and Deployment*

The growing energy consumption and environmental concerns have been driving an ever-increasing demand for efficient and reliable electrical energy storage (ESS) systems for the utilization of renewable and clean energy resources (such as wind, solar and tide).[1,2] The most essential criteria for developing the ideal large-scale EES systems are low cost, high reliability, good safety, environmental friendliness, energy efficiency, long cycle life, and high energy and power densities. Among numerous candidates, lithium-ion batteries (LIBs), benefiting from high gravimetric energy density, long cycle life, and light weight, have long been the most attractive and widely used EES systems, especially in communication and transportation industry.[3,4] LIBs possess the overwhelmingly competitive advantage on gravimetric energy density , which already exceeds 240 Wh kg^{-1} and has the potential to be pushed to 500 Wh kg^{-1}, at least in theory.[4–6] However, the application of LIBs as large-scale energy storage systems is hindered by its high cost and the safety and environmental issues. In LIBs, highly toxic and combustible organic electrolytes are used, the possible reactions between electrodes and electrolytes pose additional risks.[7] Moreover, the energy efficiency and gravimetric power density of LIBs are unsatisfactory due to the low ionic conductivity of organic electrolytes and the formation of solid-electrolyte

interphases.[8,9] In addition, the cost of LIBs is relatively high due to not only the high price of materials, but also the stringent cell assembly requirements (rigorously moisture-free manufacturing conditions).[7,10] Considerable research efforts have been made to address the above concerns. One is the development of solid-state electrolytes for all-solid-state lithium batteries.[11–13] There is also a growing interest on the design of ionic liquid as alternative electrolytes for LIBs.[14,15] Recently, a surge of research activities have been conducted on bringing lithium metal back as the anode through surface passivation and morphology design in combination with the tailored electrolyte chemistry.[16,17] Search for cobalt-free cathodes with large capacity and high voltage is also making steady progress.[18] There is no doubt that new progress is going to be made on the development of LIBs with better performance, reduced cost and higher safety. In spite of the concentrated work in Li-based rechargeable batteries, an increased attention has also been paid to the exploration of other promising EES systems.

Sodium ion batteries (SIBs), for example, have been extensively investigated and considered as a promising alternative battery technology, due to the wide abundance and low cost of sodium, as well as their similar electrochemical mechanisms to LIBs.[19,20] The development of SIBs towards large-scale applications, however, still encounters some inevitable challenges. First, the operation voltage of SIBs is low (~0.3 V lower than Li). Second, the ionic size of Na^+ (1.02 Å) is much larger than that of Li^+ (0.76 Å), leading to a sluggish reaction kinetics and poor electrode stability. Third, the desired electrode materials with satisfied Na^+ ion storage capacity and long-term cyclability are still lacking.[21] There has also been a growing interest in developing potassium ion batteries (PIBs) lately, because the very low redox potential of K/K^+ (−2.92 V) endows PIBs a high operation voltage.[22–24] However, the ionic radius of potassium (1.38 Å) is even larger than that of sodium ion,[24] and thus PIBs face much severer issues in transport kinetics and cycling

stability. Multivalent ion batteries are other promising contenders because multivalent ions enable more than one electron transfer. Divalent magnesium ion batteries, for instance, in principle offer a high volumetric energy density of 3833 mA h cm^{-3} (almost two times of Li: 2062 mA h cm^{-3}) and has a low reduction potential (−2.4 V vs. SHE).[25,26] Challenges that hamper the progress of magnesium ion batteries, however, come from the strong electrostatic interactions between the divalent Mg^{2+} ions and the host lattice of cathode materials. Not only does such strong electrostatic interaction lead to the sluggish Mg^{2+} diffusion kinetics, but also prevent the high-performance cathode to reach its full storage capacity. In addition, the lack of compatible electrolytes is another big hurdle in realizing the practical application of magnesium ion batteries.[27] Responding to the green and safe chemistry, exploration of battery technologies based on the safe, non-toxic and low-cost aqueous electrolytes also becomes desirable.[28,29] First, the safety issue of flammable organic electrolytes is avoided. Second, the higher ionic conductivity of aqueous electrolytes (aqueous electrolytes: ~1 S cm^{-1}, organic electrolytes: ~1-10 mS cm^{-1}) enables a fast charge/discharge rate.[30] Moreover, compared to organic LIBs, the aqueous rechargeable batteries are more cost-effective and easier to be assembled.[10,31] In recent years, research efforts in the rechargeable aqueous batteries also begin to shift to the other naturally abundant and low-cost metal ions, including Na-,[32] K-,[33] Zn-,[34] Ca-,[35] Mg-,[36] and Al-ion.[37]

Among the "beyond lithium" technologies, aqueous zinc-ion batteries (ZIBs) are particularly attractive owing to the following inherent advantages of Zn (Table *1.1*): low cost arising from its natural abundance and massive production, non-toxicity, easy and mature processing, high volumetric energy density (5851 mA h mL^{-1}),[34] high stability and compatibility in aqueous electrolyte, and the two-electron-redox properties of Zn ion leads to a high theoretical metal anode capacity (820 mA h g^{-1}).[38] Therefore, the aqueous ZIBs, which employ Zn metal as the anode, Zn-

intercalating materials as the cathode, and neutral or slightly acidic Zn-containing solutions as the electrolyte, are compelling alternative battery systems for large-scale application. The relatively high gravimetric energy and power density of aqueous ZIBs as compared with those of other EES systems are shown by the Ragone plot in Figure 1.1.

Table 1.1. Comparison of Zn^{2+} and other metal cations as charge carriers for rechargeable batteries. Reproduced with permission from ref [34]. Copyright 2020, American Chemical Society.

Charge Carrier	Ionic Radius (Å)	Standard Potential (V *vs*. SHE)	Theoretical Capacity		Abundance in the Earth's crust (ppm)	Cost ($/lb)
			Gravimetric (mA h g^{-1})	Volumetric (mA h cm^{-3})		
Li	0.76	-3.04	3862	2062	17	8-11
Na	1.02	-2.71	1166	1128	23,000	1.1-1.6
K	1.38	-2.92	686	610	15,000	3-9
Zn	0.74	-0.76	820	5851	79	0.5-1.5
Mg	0.72	-2.36	2205	3833	29,000	1-1.5
Ca	1.00	-2.86	1340	2073	50,000	—
Al	0.54	-1.67	2980	8046	82,000	0.5-1.5

Note: The price of metals is collected from METALARY (https://www.metalary.com/lithium-price/).

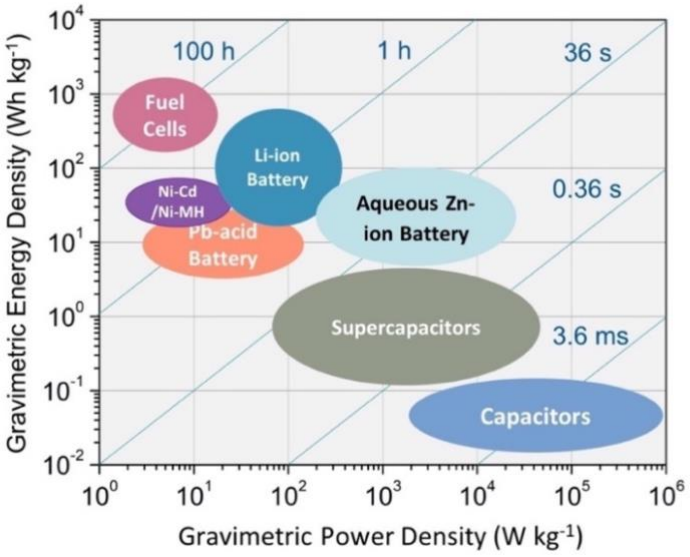

Figure 1.1. Ragone plot of several EES systems. Redox reaction dominated batteries present higher gravimetric energy density and surface adsorption supported capacitors render higher gravimetric power density. The aqueous zinc ion batteries (ZIBs) probably possess the highest gravimetric energy and power density combination owing to its fast reaction kinetics endowed by the smaller working ions and the open frameworks of the cathode materials, especially the layered vanadate hydrates. Note: the gravimetric energy and power density data of aqueous ZIBs are collected from the current research publications.[58] In the commercial cells, they should be a little bit lower. Reproduced with permission from ref [34]. Copyright 2020, American Chemical Society.

1.1.2 *Components and Working Principle of Aqueous Zinc-ion Batteries*

Figure 1.2a schematically outlines the device structure and the working mechanism of aqueous ZIBs, the Zn^{2+} intercalation cathodes are separated by a glass fiber or a cellulose filter from the zinc metal anode. The electrolyte is a water-based Zn^{2+}-containing salt solution. During the working processes, Zn^{2+} ions will strip from/plate on the metallic anode, and insert into/extract from the cathode material. The working mechanism of ZIB is similar to that of LIBs (Figure 1.2b). Li ions shuttle back and forth between cathodes and anodes, which are separated by a porous polymer film in a nonaqueous electrolyte. Figure 1.2c depicts the principles for the selection of LIBs electrode materials with a matching electrolyte. Commonly, the chemical potential of the cathode reaction (μ_C) must be higher than the highest occupied molecular orbital (HOMO) of the nonaqueous electrolyte, and the chemical potential of anode (μ_A) should be lower than the lowest unoccupied molecular orbital (LUMO) of the electrolyte. Otherwise, the electrolyte will be reduced on the anode side or oxidized on the cathode. The redox reaction of an electrolyte will produce passivating layers on the electrode materials.[39,40] The thin layer formed on the anode side from electrolyte decomposition is called as solid electrolyte interphases (SEIs), which consist of

organic and inorganic components including LiF, Li_2CO_3 and polymer-like gel. SEI is easy to form in the current LIB systems because most of the organic solvents will be reduced below 1.2 V *vs*. Li^+/Li.[8,41] On the cathode side, electrolytes could be decomposed when the charging voltage exceeds 4.3 V. The formed passivating layer is called as the cathode electrolyte interphases (CEIs), which have similar compositions as the SEIs.[8,42] The formation of SEIs or CEIs will increase the internal resistance of batteries and consume the active Li-ions from the cathode, leading to a low Coulombic efficiency (CE) in the initial cycles. However, once the formation of SEI or CEI is completed, they will protect the electrode materials from contacting with the electrolyte directly, thus suppress the side reactions to ensure the cycling stability of batteries.[8] In addition, the difference between μ_C and μ_A is the open circuit voltage of the battery. Choosing a high voltage cathode and a low voltage anode endows a battery with higher open circuit voltage if the compatible electrolyte is available.[43] The biggest difference between LIBs and aqueous ZIBs comes from the electrolyte solvent they used. The Pourbaix diagram of water in Figure 1.2d indicates the decomposition window as a function of pH value. Similar to the HOMO and LUMO in nonaqueous electrolytes, water molecules will be decomposed to release oxygen or hydrogen when the applied voltage is higher or lower than a certain value.[38] Therefore, designing an aqueous ZIB should consider the following aspects, (1) the redox potential of cathode materials should be below the upper voltage of water decomposition, (2) the pH of the electrolyte should satisfy the redox reactions of cathodes, (3) the current collector should be chemically stable within the working voltage range, taking into account the pH variation in the charge/discharge processes. Zinc metal has a higher standard potential than lithium or sodium (as listed in Table *1.1*) and it is chemically stable in air. Therefore, zinc metal is a promising anode material for ZIBs, fewer efforts have been made on the exploration of new anode materials in the past, except for developing

strategies to improve its reversibility and plating/stripping efficiency. Exploiting a cathode with a high working voltage and a large specific capacity is the primary focus, with the goal of increasing the gravimetric energy density of ZIBs to be competitive with LIBs.

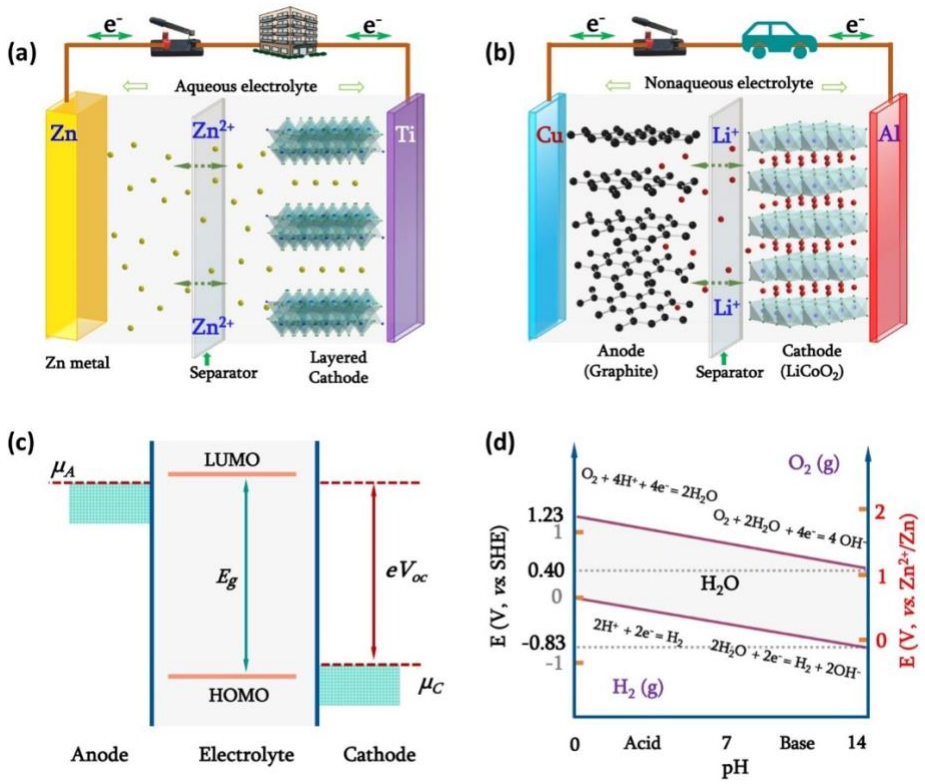

Figure 1.2. (a) Configuration of ZIBs. The metallic zinc anode is separated by a porous film from the intercalation cathode in an aqueous electrolyte. In the energy storage processes, Zn^{2+} ions strip from or plate on the anode, and intercalate into or de-intercalate from the cathode. (b) Schematic illustration of the LIB configuration. Intercalating-type electrode materials pasted on the Cu or Al current collectors are separated by a porous polymer film in a nonaqueous electrolyte. (c) Relationship between energy levels of electrodes and electrolytes. In a battery design, μ_C should be higher than the HOMO of electrolyte and μ_A could be lower than LUMO. The chemical potential difference between both electrodes is the open circuit voltage of the battery. (d) Pourbaix diagram of water. It provides a map for the electrolyte formulation to ensure the maximum gravimetric energy density of a battery. Reproduced with permission from ref [34]. Copyright 2020, American Chemical Society.

1.2 Progress and Challenges in Aqueous ZIBs

Aqueous ZIBs hold great promises for practical applications in large-scale energy storage due to their cost-effectiveness, environment-friendliness, intrinsic safety, and relatively high gravimetric energy and power densities. Prior research has firmly established and demonstrated the availability and feasibility of the active materials to construct a working ZIB device. Divalent zinc ions allow a high theoretical storage capacity. Such a great capacity does come with a price, the strong electrostatic interactions between the divalent Zn^{2+} ions and host materials significantly impact the transport kinetics and the structural stability during cycling. The incorporation of modifying ions, clusters, or molecules has shown to be able to circumvent such hurdles. Compositing/coating with highly conductive materials, introducing defects and developing disordered atomic arrangement also show the possibility to address the kinetics and stability issues of cathode materials (Figure 1.3). Low discharge voltage of the current cathode materials largely prevents the attainment of the full zinc ion storage capacity. In theory and in practice, zinc ion batteries are unlikely, if not impossible, to achieve a specific energy density higher or even comparable to that of lithium-ion batteries as schematically illustrated in Figure 1.1. Studies on anode materials have been largely concentrated on zinc metal. Zinc metal has a hexagonal structure and shows a strong tendency to grow along the high surface energy facets, favoring dendrite growth. Such preferential growth of high surface energy facets also offers a great possibility for manipulating the dendrite growth through surface passivation, for example, by adsorption of surfactants on the high surface energy facets, or by epitaxial electrodeposition or crystal seeding to confine the preferential growth of Zn along the substrate surface (Figure 1.3). Aqueous electrolytes offer the unmatched safety and ionic conductivities in comparison to the organic electrolytes, and its low cost and environmental benignity are other significant merits. Additional work is very much needed to explore the aqueous

electrolytes with wide electrochemical stability window and good compatibility with electrodes and other components. So far, the choice of current collecting materials, which are electrochemically stable in aqueous electrolytes, is quite limited. And they are all hard materials, thus hindering the intimate contact between current collectors and electrode materials. Much of the research are focused on the individual material or components; studies on the whole integrated batteries and their performance are still limited. Holistic considerations in the pursuit of promising cathode materials with high discharge voltage, fast kinetics and long cycling stability, the stable Zn anodes with high Zn stripping/plating Coulombic efficiency, high dendrite- and corrosion-resistance are needed. Additional work is very much needed to explore the low-cost electrolytes with wide electrochemical stability window and good compatibility with electrodes, and more attention should also be paid on the search for current collectors with desirable chemical, mechanical and electrochemical stability. The issues and prospective strategies towards the future development of the cathode, anode and electrolyte is schematically summarized in Figure 1.3.

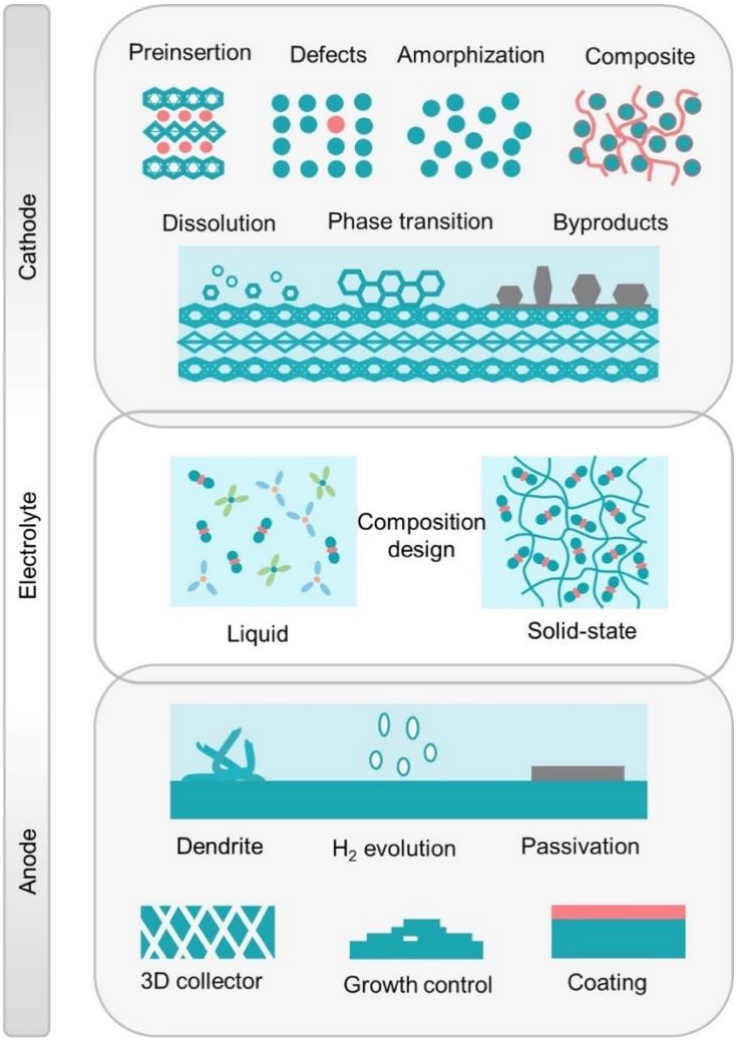

Figure 1.3. An overview of the issues and prospective strategies towards the future development of the cathode, anode and electrolyte for aqueous ZIBs.[34] Cathode materials usually suffer from issues like material dissolution, irreversible byproduct formation, and surface passivation, thus posing threats to battery stability and reversibility, especially under low current densities. The developed strategies can be categorized into the guest species pre-insertion, amorphization, defects introduction as well as the composite design. For the anode, challenges mainly arise from dendrite growth, hydrogen evolution and passivation. The optimization of Zn anode could be achieved through designing the 3D current collector, controlling the preferential Zn growth and introducing an artificial interphase. The further design of electrolytes towards expanding the electrochemical stability windows and alleviating the electrode issues is highly desirable. Reproduced with permission from ref [34]. Copyright 2020, American Chemical Society.

1.2.1 *Anode Materials*

As a naturally-abundant, low-cost, nontoxic and inherently safe metal with high theoretical capacity, metallic zinc has been widely investigated as an ideal anode material for primary alkaline Zn–MnO_2 battery,[44] Zinc-air battery,[45] and now aqueous ZIBs.[46] The redox potential of Zn^{2+}/Zn is higher than that of Li^+/Li or Na^+/Na, hence resulting in a relatively low battery voltage.[47] This restricts the selection of anode materials for ZIBs other than the zinc metal. Similar to the lithium metal anode in LIBs, the practical application of metallic zinc anodes is also challenged by the low utilization of Zn, and issues like dendrite formation and insufficient plating/stripping efficiency caused by the uneven deposition of zinc cations. Strategies towards addressing these issues follow two main directions, electrolyte optimization and anode design. The electrolyte optimization approach, such as using highly concentrated electrolytes or adding electrolyte additives, although facile and effective, is inevitably against the low-cost advantages of ZIBs. In light of this, more efforts should be devoted to the optimization of Zn anode, which includes surface modification and structure design.

3D nanostructured anode construction is one of the most effective and well-established approaches to ensure the uniform Zn^{2+} ion deposition and achieve high stripping/plating efficiency, which is simply electrodepositing Zn onto a highly conductive, nano- or micro-structured substrate. The favorable substrate/current collector should possess attributes like a high electroactive surface area to ensure the even current distribution, the well confined nucleation sites to enable the uniform Zn plating/striping, and a porous structure to accommodate the dendrite formation and the volume change. As a result, a reduced polarization, high Coulombic efficiency, as well as prolonged cycling stability can be achieved by employing the 3D nanostructured Zn anode. So far, 3D porous copper skeleton,[48] carbon film,[49] graphene foam,[50] carbon fibers,[51] carbon nanotube yarns,[52] and

graphite felt,[53] have been studied and demonstrated to be the promising substrates/current collectors for the electroplated zinc anodes. Furthermore, the surface morphology, texture and crystallographic orientation of the electrodeposited zinc anode could be further tailored by adding organic/inorganic additives into the electrodepositing electrolyte.[54,55] Tuning the electrodeposited zinc electrodes with high-surface areas and favorable particle shapes could further inhibit the dendrite growth and hence improve the rechargeability and plating/stripping efficiency of Zn anode.[56,57] In addition, microstructures of the electrodeposited zinc anode could also be modified to yield better electrochemical performance, many well-controlled microstructures, including the zinc fibers, foams, flakes, ribbons and needles, have been studied for zinc anode.[57–59] Surface coating can be applied on the Zn anode to further improve the interfacial stability and cycling stability. The ideal coating layer should be dense, flexible, ionic conductive, as well as highly water and O_2 resistant, so as to effectively alleviate the Zn dendrite formation and simultaneously avoid side reactions.

Although all the above-described anode design approaches could help to minimize the zinc dendrite formation and contribute to a highly reversible Zn plating/stripping behavior, obviously, they all have limitations that prevent their practical applications. For example, constructing a 3D hierarchical Zn architecture requires an expensive and complex synthesis process; modification of surface morphology has limited impacts, and the added organic/inorganic additives might be expensive and toxic; surface coating, however, might increase the electrical resistance and discount the gravimetric energy density. Therefore, integrating the previous modification methods together or developing some new facile and low-cost strategies is highly desired to achieve the well-preformed Zn anode with long lifespan. More efforts should be made to explore new Zn electrodeposition chemistry, or to incorporate different surfactants, levelling and brightening

agents to the zinc deposition solution. Further fundamental understanding of the effects of chemical composition and additives in electrolytes on the electrolysis and electroplating processes on the zinc anode surface is also very essential. Data mining from literature in electrometallurgy, electrolysis, electroplating, and the other battery technologies should shed some lights on the development of new strategies for protecting and improving the performance of zinc anode.

1.2.2 *Electrolytes and Current Collectors*

So far, the most extensively used aqueous electrolytes for ZIBs are the mild $Zn(CF_3SO_3)_2$ and $ZnSO_4$ aqueous solutions (pH~4). ZIBs with the $ZnSO_4$ electrolyte usually suffer from rapid capacity decay due to the dissolution of active materials. Though it can be largely suppressed by the introduction of additives, the overall performance of $ZnSO_4$ electrolyte is inferior to that of $Zn(CF_3SO_3)_2$. The large-scale application of $Zn(CF_3SO_3)_2$ electrolyte is, however, hindered by its prohibitive cost. Although ZIBs based on these neutral/mild electrolytes will not suffer from sever Zn dendrite growth at low current densities, dendrite issues and low Zn stripping/platting CE cannot be neglected at large current densities or with high cathodic loading mass. Due to the existence of a large amount of free water, side reactions, such as the corrosion and passivation of anode, the active material dissolution from cathode, as well as the byproduct formation on both electrodes, are currently inevitable in aqueous electrolytes. Though the highly concentrated (water-in-salt) aqueous electrolytes could alleviate these water-induced side reactions and expand the electrochemical stability window (to ~ 3.0 V), its high cost remains as the big problem. Regarding aqueous electrolytes, therefore, more work is urgently needed on the search for new zinc salts and additives with affordable prices, as well we the modification of electrolyte concentrations, with the aim of achieving an expanded electrochemical stability window, high Coulombic efficiency and prolonged cycling stability.

Another promising way to suppress the water activity is to develop the solid/gel polymer electrolytes (GPEs), which is also of great significance for the future application of ZIBs in wearable and portable electronics. To this end, GPEs need to be specially designed with a high ionic conductivity, high mechanical tolerance, good interfacial contact with electrodes, a large Zn^{2+} transfer number, as well as the wide electrochemical and thermal stability windows. More efforts should be made to explore new polymer matrix and zinc salts for GPEs, or modify the specific properties of GPEs by copolymerization, composite formation, or addition of functional groups, *etc*. Overall, for the future development of both the aqueous and the solid-state electrolytes for ZIBs, special attention should be paid on the fundamental understandings of the degradation mechanisms of electrolytes, as well as the interplay between electrolytes and the other battery components (electrodes and the current collectors). Moreover, standard evaluation methods need to be designed in order to characterize and compare the electrochemical performance and the mechanical properties (for solid-state electrolyte) of electrolytes.

The compatible current collector is also limited to a few less ideal metals; so far only stainless steel and titanium are the promising choices for ZIBs, while their insufficient electrical conductivity and high hardness will compromise the battery performance. New current collector materials or new structures, such as laminar structures with different chemical compositions, may permit designing, selecting, and tailoring the desired mechanical and electrical properties for current collectors in ZIBs.

1.2.3 *Cathode Materials*

The cathode is inarguably the most extensively investigated component of the aqueous ZIB system so far. The main obstacle that hinders the further advancement of aqueous ZIBs is the lack of

desirable cathode materials that meet all the requirements including large capacity, high voltage, fast Zn^{2+} insertion/extraction kinetics, good structure stability, and good compatibility with the electrochemical stability window. Searching for the new cathode candidates or developing approaches to tailor the current cathode materials is a crucial prerequisite to achieve the stable high-performance aqueous ZIBs. A comparative summary of the gravimetric energy/power density of aqueous ZIBs with various types of cathode materials is present in Figure 1.4. Manganese based cathodes offer the highest energy density due to the high operating voltage (~1.3 V) and the moderate capacity (~300 mA h g^{-1}). The open crystal structure endows vanadium- and dichalcogenide- based cathodes with the highest power output. Organics cathode, though show great potential in the flexible solid state ZIBs, are uncompetitive for the high power density application due to their intrinsically poor electronic conductivities. The performance of Prussian Blue analogues and polyanion compounds is limited by the slow kinetics and inadequate active sites.

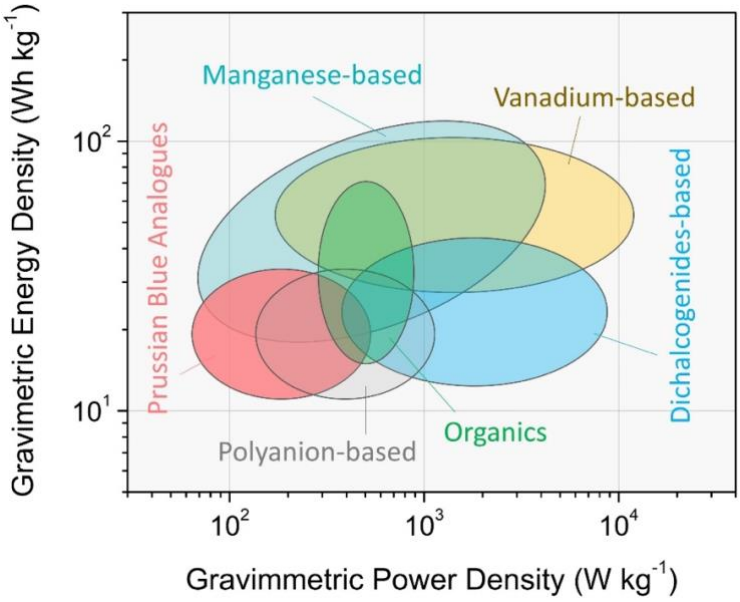

Figure 1.4. Ragone plot of the reported aqueous ZIBs with typical cathode materials. The high operating voltage (~1.3 V) and moderate capacity (~300 mA h g^{-1}) endow the Mn-based oxides

with a high energy output. The open crystal structure of vanadium-based compounds and dichalcogenides allows the fast ions diffusion, thus enabling a competitive power density. The slow kinetics or inadequate active sites or poor electronic conductivities largely limit the energy/power output of the Prussian Blue analogues, polyanion compounds and organic cathodes. Reproduced with permission from ref [34]. Copyright 2020, American Chemical Society.

Mn-based oxides are the earliest and the most extensively investigated Zn^{2+} host materials.[60] Their Zn-ion storage mechanisms, however, are still controversial. Five different mechanisms have been reported so far, which are Zn^{2+} insertion/extraction, H^+ and Zn^{2+} co-insertion/extraction, chemical conversion reaction, the combined intercalation and conversion reaction, and the dissolution-deposition mechanism. The reversible Zn^{2+} ion intercalation/de-intercalation has been by far the most widely accepted mechanism. A thorough understanding of the reaction mechanisms through a combination of *in-situ* and operando characterization techniques and theoretical calculations would contribute to the future exploration of new cathode materials and the modification of the known cathode materials. In addition, the poor structural stability and the low electrical conductivity are the two main obstacles that hinder the applications of Mn-based cathodes. Their intrinsically poor electrical conductivity is currently circumvented by doping with transition metal cations or compositing with the conductive carbon-based materials. More serious issue is the rapid capacity fading and limited lifetime due to the dissolution of divalent Mn ions during charge/discharge cycles, similar to that of Mn-based cathodes in LIBs. This could be partially mitigated by the pre-addition of Mn^{2+} salts in electrolytes. However, more efficient approaches are still needed to better stabilize the Mn-based cathode materials. Surface coating of the cathode may be effective to suppress the dissolution of divalent Mn ions, as what has been employed to improve the stability and cyclability of the NCA-based ($LiNi_{1-x-y}Co_xAl_yO_2$) or NCM-based ($LiNi_xCo_yMn_{1-}$

$_{x-y}O_2$) or NCMA-based ($LiNi_{0.89}Co_{0.05}Mn_{0.05}Al_{0.01}O_2$) cathodes for LIBs.[61–63] Doping may also be applicable for stabilizing the crystal structure and, thus, reduce the dissolution of active materials.

The open framework with large diffusion channels makes Prussian blue (PB) and its analogues (PBAs) the potential cathode materials for LIBs and SIBs.[64–67] However, when working as the Zn ion hosts, PBs/PBAs show very limited specific capacities as well as poor cycling stability. This might be attributed to the irregularity of the PBA crystal structure. The large amount of randomly distributed $Fe(CN)_6$ vacancies and coordinated water molecules would not only decrease the available sites for the Zn^{2+} ions insertion, but also break down the Fe-C≡N-M bridges forming an unstable, distorted crystal structure, and interrupt the electronic conduction along Fe-C≡N-M. Though PBAs with improved crystallinity may offer much improved cycling stability, their Zn^{2+} ion storage capacity is only around 60 mA h g^{-1}, far lower than that of Mn-based or V-based materials. Despite a high theoretical operating voltage (~1.7 V), the further development of PBAs as ZIB cathode is largely hindered by its low capacity.

Organic/polymeric materials with light weight, high structural diversity and good molecular-level tunability are also promising cathode alternatives for ZIBs, especially for the flexible solid-state ZIBs. Moreover, using organic electrodes makes ZIBs possible to work under the extreme environment, such as a large temperature window or a wide pH range. However, redox-active polymers, such as quinone, usually suffer from rapid capacity fading due to the inherent instability and solubility of the discharged product in electrolyte. Therefore, a supporting solid matrix [68] or an ion-selective membrane [69], is usually required. Towards the future application of organic cathodes, significant advance is required in understanding the energy storage mechanism of Zn/organic batteries, and developing new organic/polymetric cathodes with two important concerns— a high electronic conductivity and a low solubility in electrolyte.

Vanadium-based compounds have attracted an increasing attention as promising cathode materials for multivalent batteries due to their large theoretical capacity, versatile crystal structures, resource abundance, and low cost.[70–72] The multiple oxidation states of vanadium (V^{2+}, V^{3+}, V^{4+}, V^{5}) and the facile distortion of V-O polyhedron give rise to a variety of vanadium oxides with different compositions and structural frameworks (Figure 1.5). So far, a few types of vanadium-based materials have been studied as ZIB cathodes and demonstrated a favorable zinc ion storage ability, including vanadium oxides, metal vanadates, vanadium phosphates, and so on. Vanadium-based cathode materials possess, so far, the highest capacity (generally exceeding 300 mA h g^{-1} or even more than 400 mA h g^{-1}); however, they suffer from unsatisfactory cycling performance due to the structural instability, and a relatively low operating voltage (~0.9 V). Battery voltage is partially limited by the narrow electrochemical stability window of aqueous electrolytes. To realize ZIBs with a higher gravimetric energy density, cathode materials with a high and flat discharge plateau are always desirable. Some work has demonstrated such feasibility, for example, $Co_{0.247}V_2O_5{\cdot}0.944H_2O$ nanobelt display a high operational voltage of 1.7 V because the interactions between Co 3*d* and V 3*d* orbitals shifts the redox potential to a higher level.[73] A new redox couple activated by phase transition would rise the discharging voltage of CuO cathode by 0.25 V when Cu^{+}/Cu couple participates in the electrochemical reaction.[74] The introduction of anionic redox chemistry could also promote the electrochemical activity of the cathode materials.[75] For example, the oxygen redox reaction can be activated by introducing the P-O covalent bonds in the V_xO_y layer; in this way the V–O covalence will be weakened and, thus, enhance the electron density of oxygen centers.[76] For the Zn/$VOPO_4$ battery, in addition to the conventional vanadium redox reaction, the oxygen redox reaction ($O^{2-} \leftrightarrow O^{-}$) will occur in the high-voltage region, giving rise to a wide voltage window of 0.8–2.1 V, an enhanced average working voltage of 1.56

V, and a capacity increase of 27%.[76] Besides, other promising strategies to modulate the electrochemical potential of redox couples include but are not limited to (1) cation or anion doping through either substitution or pre-insertion; such doping would affect the electronic structure of cathode materials due to the varied ionic radius, valence state, vacancy creation or interstitial ion introduction, (2) surface chemistry modification through controlled annealing, ionic exchange, and coating to tune the surface potential and minimize the energy barrier for Zn^{2+} intercalation and de-intercalation, (3) tuning the crystallinity or amorphization of the cathode materials through kinetically controlled synthesis approaches, and (4) inducing the formation of metastable phase with desired electronic configuration. To push the advance of ZIBs to the next level, new chemistry might want to focus on the development of cathode materials that provide both high voltage (>1.2 V) and large capacity (>400 mA h g^{-1}).

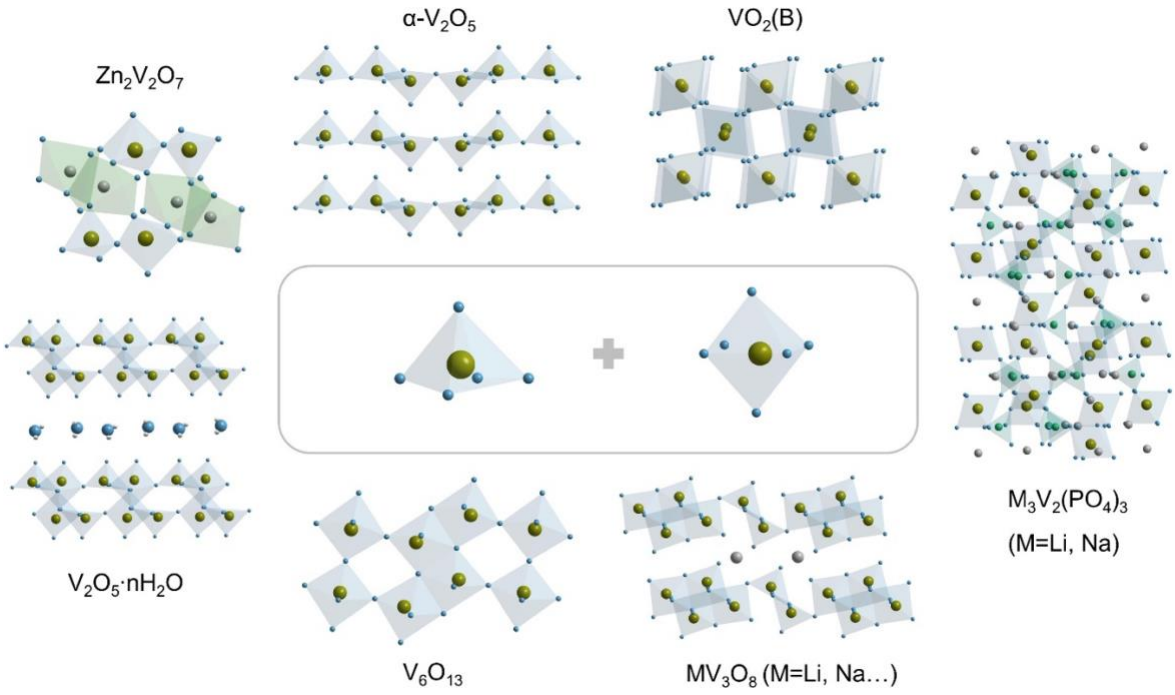

Figure 1.5. Crystal structures of typical vanadium oxides: orthorhombic α-V_2O_5; monoclinic VO_2(B), $V_2O_5{\cdot}nH_2O$, and MV_3O_8 (M=Li, Na, K…), trigonal V_6O_{13} and $M_3V_2(PO_4)_3$ (M=Li, Na,

K…); and triclinic $Zn_2V_2O_7$. Reproduced with permission from ref [34]. Copyright 2020, American Chemical Society.

1.3 Vanadium Oxides and Pre-intercalation Strategy

1.3.1 *Vanadium Oxides*

Vanadium, a transition metal element, possesses the electronic configuration $[Ar]3d^34s^2$. This configuration enables vanadium to exhibit a wide range of oxidation states, resulting in the formation of four single valent oxides: V_2O_5 (+5), VO_2 (+4), V_2O_3 (+3), and VO (+2). Each of these oxides exhibit distinct colors: orange/yellow for +5, blue for +4, green for +3, and violet for +2.[77] Moreover, vanadium forms mixed valance oxides, such as V^{5+}/V^{4+} mixed oxides, known as the Wadsley phase (V_nO_{2n+1}), which includes compounds like V_6O_{13}, V_4O_9, and V_3O_7. And there are V^{4+}/V^{3+} mixed oxides, referred to as the Magnéli phase (V_nO_{2n-1}), including compounds likeV_8O_{15}, V_7O_{13}, V_6O_{11}).[78]

Vanadium also exhibits a variety of polyhedral coordination with oxygen atoms, including tetrahedron, distorted octahedron, trigonal bipyramids, rectilinear octahedron, and square pyramids.[79] Figure 1.6 illustrates the correlation between coordination types and oxidation states.[79] For example, both V^{4+} and V^{5+} ions can be found in distorted octahedrons, trigonal bipyramids, or square pyramids. V^{5+} can also appear in tetrahedrons while V^{4+} not. V^{3+} cations exclusively coordinate with oxygen in rectilinear octahedrons. These polyhedra can be linked through sharing corners or edges, thus forming the vanadium oxide network in the sequence of polyhedron→ chain→ layer→ three-dimensional framework.

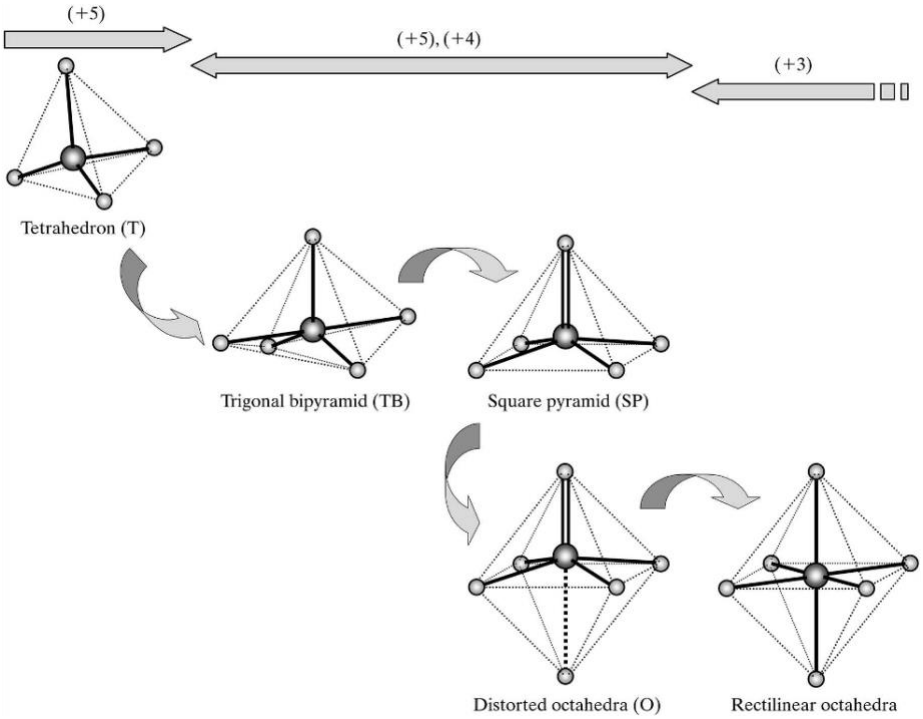

Figure 1.6. Schematic of the vanadium coordination polyhedra. Reproduced with permission from ref [79]. Copyright 1999, International Union of Crystallography.

Owing to their multiple oxidation states and diverse crystal structures, vanadium oxides have found applications in various industries. The interplay of *d* electrons within partially filled orbitals, renders their structural and chemical transformations exceptionally responsive to subtle changes in external stimuli, such as temperature, pressure, electrical charge, and photon radiation.

Several vanadium oxides, such as VO_2, V_2O_3, and V_2O_5, undergo a metal-insulator transition at specific temperature. For instance, VO_2 behaves as a semiconductor below 340 K. However, upon crossing this threshold, its electrical conductivity experiences a remarkable increase by a factor of 10^4 to 10^5 due to the first-order structural phase transitions. Above 340 K, VO_2 exhibits metallic behavior.[80,81] These phase transitions are reversible and accompanied by significant and rapid changes in optical, electrical, and magnetic properties, making these oxides as promising candidates for high-speed electronics, thermally activated switches, and thermal sensors. Moreover,

vanadium oxides possess excellent catalytic activities, good intercalation capabilities for hosting guest molecules/ions, and strong electron-electron correlations. Such attributes make them suitable for applications in catalysis, energy conversion and storage devices, smart windows, sensors, and beyond.[77]

1.3.2 *Vanadium Pentoxides*

Among the big family of vanadium-oxides, V_2O_5 stands out with its highest oxidation state and exceptional chemical stability. Depending on growth conditions, V_2O_5 can exist in various polymorphs, including α-V_2O_5 (orthorhombic), β-V_2O_5 (monoclinic or tetragonal), δ-V_2O_5 (a modification of β-V_2O_5), γ-V_2O_5 (orthorhombic), ζ-V_2O_5, and ε-V_2O_5. Among these, α-V_2O_5 is the most thermodynamically stable one, characterized by a P*mmn* space group (59), with lattice parameters a = 11.51 Å, c = 3.56 Å, and c = 4.37 Å.[77,82]

As shown in Figure 1.7, α-V_2O_5 features a layered structure constructed from [VO_5] square pyramids.[83] When considering oxygen atoms from adjacent layers, the coordination geometry can be described as distorted octahedra. The [VO_5] pyramids form double chains along (010) through edge sharing, and these chains are cross-linked to form layers by sharing corners along (100). Adjacent layers are weakly bonded along the *c*-axis via weak interactions between vanadium and oxygen atoms from neighboring layers (with a V–O distance of 2.79 Å).[84]

In the α-V_2O_5 structure, vanadium atoms form five bonds with three inequivalent oxygen atoms (Figure 1.7d). One is vanadyl oxygen (O_1), which is singly coordinated and positioned directly above or below the V atom along the *c*- axis, forming the strongest and shortest bond ($V–O_1$ =1.58 Å).[83,84] The vanadyl oxygen from the adjacent layers form an extended bond (longer $V---O_1$ = 2.79 Å), contributing to the forces that bond the layers together along the *c*-axis.[84] There are three triply

coordinated chain oxygens (O_2), with two at 1.88 Å and one at 2.02 Å, creating the chain linkages along the *b*-axis. One doubly coordinated bridge oxygen (O_3) connects the chains in the *a*-direction, forming two bonds (V–O_3=1.77 Å) with an angle of V–O_3–V =125°.[85]

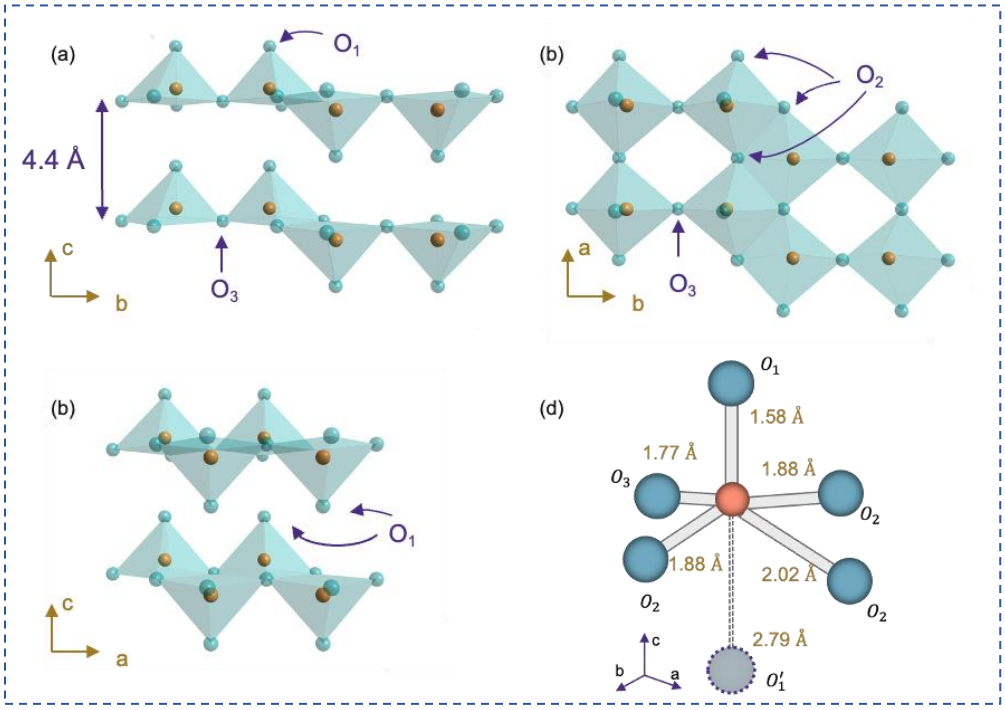

Figure 1.7. Crystal structure of orthorhombic α-V_2O_5, viewing from (a) *a*-axis, (b) *c*-axis, and (c) *b*-axis. (d) The oxygen coordination of one vanadium atom in α-V_2O_5, three inequivalent oxygen sites are marked accordingly (V atoms are in orange and O atoms are in blue).

V_2O_5 demonstrates significantly diverse structural, optical, conductivity, and electrical properties deponing on the growth techniques and conditions.[77,86] This variability allows for structural and morphological manipulation tailored to specific properties of interest. Benefiting from this versatility, along with its inherent characteristics, such as high chemical and thermal stability, abundance in nature, low cost, and ease of preparation, V_2O_5 has attracted significant interests in various applications, including energy conversion and storage, catalysis, sensors (UV, gas, humidity, or optical), optoelectronic devices, and electrochromic devices.[77]

1.3.3 *Hydrated Vanadium Pentoxides*

In electrochemical applications, a specific type of vanadium pentoxide, known as the hydrated vanadium oxide ($V_2O_5 \cdot nH_2O$), has attracted more attention. This is primarily due to its larger interlayer spacing (~11.5Å), mixed valence states (V^{5+} and V^{4+}), and its capability for facile ion-exchange. $V_2O_5 \cdot nH_2O$ is often referred to as "amorphous V_2O_5", due to the lack of long-range crystalline order. But it exhibits a well-ordered stacking of VO_5 bilayers on the nanoscale and can be considered as nanocrystalline. Due to this low crystallinity, $V_2O_5 \cdot nH_2O$ experiences less mechanical stress during guest ion insertion/release, potentially offering more active sites for ion insertion.

As illustrated in Figure 1.8, the bilayered monoclinic $V_2O_5 \cdot nH_2O$ (Space Group C2/*m*) comprises two layers of [VO_6] octahedral, separated by interlayer water molecules.[87] The presence of water molecules within the interlayer not only help to expand the interlayer spacing but also plays a crucial role in stabilizing the V–O layer. Unlike in crystalline α-V_2O_5, where [VO_5] square pyramids face up-up-down-down (Figure 1.7), all vanadyl oxygen atoms within a single chain point in the same direction (towards the outside of the layer) in the $V_2O_5 \cdot nH_2O$ phase. The distance between two single chains is approximately 2.9 Å.

The basal distance (d_{001}) is contingent upon the amount of water (n) in $V_2O_5 \cdot nH_2O$ and is influenced by the growth condition. d_{001} undergoes increments of Δd_{001}= 2.8 Å (the van der Waals radius of a water molecule),[88,89] and ranges from 8.8 Å under vacuum (n=0.6) to 11.5 Å under ambient conditions (n=1.8).[89] The interlayer water in $V_2O_5 \cdot nH_2O$ is considered to include both H_2O molecules and solvated protons (H_3O^+) at the interface of the interlayer.[90] Based on the thermogravimetric measurements, weakly-bonded water molecules are the first to leave the gel upon heating, starting from room temperature to about 120 °C. Water adsorption remains highly reversible during this stage.[91–93]

Subsequently, some water is lost between 210-270 °C, believed to be the water more strongly bonded to the vanadium oxide. Chemically bound water is then removed upon heating above 300 °C, followed by the immediate crystallization of orthorhombic V_2O_5 at 350 °C. [91–93] The entire process is described by the equation:[91–93]

$$V_2O_5 \cdot 1.6H_2O \xrightarrow{120℃} V_2O_5 \cdot 0.5H_2O \xrightarrow{250℃} V_2O_5 \cdot 0.1H_2O(amorphous) \xrightarrow{350℃} V_2O_5(crystalline) \quad (1.1)$$

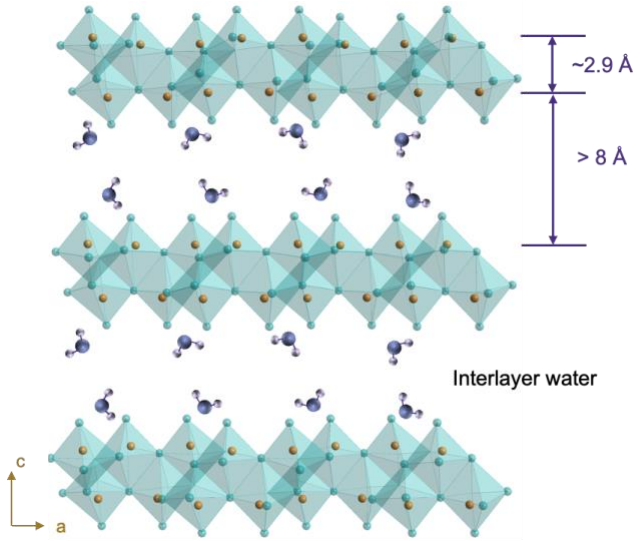

Figure 1.8. Schematic illustration of the crystal structure of $V_2O_5 \cdot nH_2O$.

1.3.4 *Formation of $V_2O_5 \cdot nH_2O$*

In general, the formation of $V_2O_5 \cdot nH_2O$ involves the formation of vanadic acid (at pH=2) and its subsequent polymerization into a gel. Several solution methods have been developed for synthesizing $V_2O_5 \cdot nH_2O$, including quenching molten V_2O_5 in H_2O,[94] hydrolysis and condensation of vanadium alkoxides or vanadates,[95] ion exchange in a resin from sodium metavanadate,[96,97] and the reaction of crystalline V_2O_5 with peroxide. Compared to the other methods, the V_2O_5—H_2O_2 preparation route is more reliable and easier to perform. Additionally,

it avoids the presence of foreign ions, and allows for previse control over the concentration of vanadium.

When dissolved in water (at room temperature), V^{5+} ions become solvated as $[V(OH_2)_6]^{5+}$. Due to the strong polarization of V^{5+} and Lewis acid properties of H_2O, some electrons transfer from the $3a_1$ orbital of H_2O to the empty $3d$ orbital of V^{5+}, reducing the electron density within the bonding orbitals of H_2O and weakening the O–H bonds.[98] Consequently, deprotonation of coordinated water molecules occurs spontaneously (as below), leaving the solution more acidic:[98]

$$[V(OH_2)_6]^{5+} + hH_2O \Longrightarrow [V(OH)_h(OH_2)_{6-h}]^{(5-h)+} + hH_3O^+ \qquad (1.2)$$

h is the hydrolysis ratio and changes with pH.

At room temperature, a large variety of vanadate species can be found in aqueous solutions, primarily depending on pH and vanadium concentration (Figure 1.9).[99]

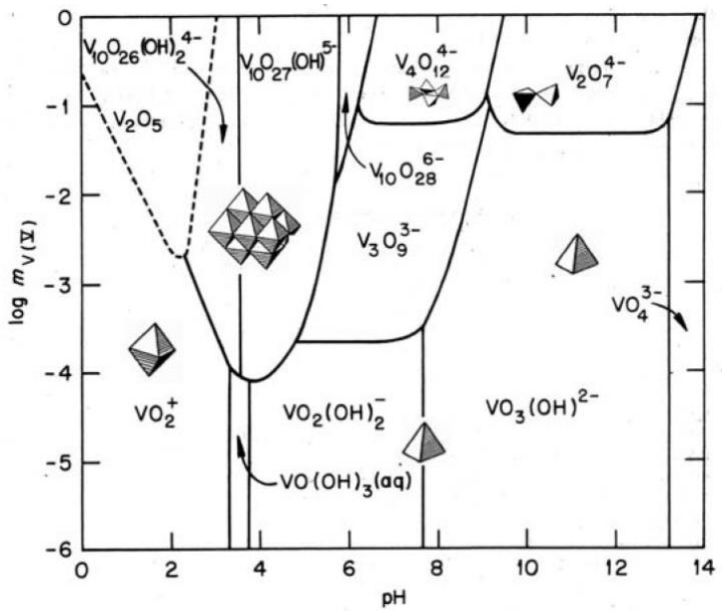

Figure 1.9. V^V species equilibrium in aqueous solutions as a function of pH and concentration. Reproduced with permission from ref [99]. Copyright 2010, by the authors.

At pH=0, the less deprotonated species should correspond to $[V(OH)_4(OH_2)_2]^+$ (h=4), but some internal proton transfer occurs between the adjacent OH groups and form the V=O double bonds. So the stable form at low pH (<2) is then the $[VO_2(OH_2)_4]^{2+}$, or $[VO_2]^+$ species (Figure 1.9).[98] Notably, as deprotonation progresses, the positive partial charge of vanadium decreases as more electrons transfer from the coordinated O to the empty 3*d* orbital of the V^{5+} atom. The V–O bond becomes more covalent, and the coordination of V^{5+} decreases from six-fold to four-fold. This coordination change of V^{5+} occurs around pH at 6, and can be observed from the color change from yellow/orange ($[VO_6]$) to colorless ($[VO_4]$). At high pH (>13), the stable form of vanadium species is tetrahedral $[VO_4]^{3-}$. Monomeric species can only be observed when the aqueous solutions is very diluted.

Normally, in the pH range where V–OH groups are formed ($2 \leq pH \leq 13$), condensation occurs via the following two reactions:[98]

Oxolation:

$$V - OH + HO - V \Longrightarrow V - O - V + H_2O \qquad (1.3)$$

Olation:

$$H_2O - V - OH + H_2O - V - OH \Longrightarrow H_2O - V - OH - V - OH + H_2O \qquad (1.4)$$

In the presence of hydrogen peroxide, V_2O_5 powder can be completely dissolved, releasing O_2 gas and forming a clear orange solution containing diperoxo species $[VO(O_2)_2]^-$. The unstable $[VO(O_2)_2]^-$ gradually decomposes into the monoperoxo species $[VO(O_2)]^+$, causing the color of solution turns to deep red.[100] Eventually, all of the peroxo species decompose, resulting in an orange/yellow solution of decavanadic acid $[H_2V_{10}O_{28}]^{4-}$ and $[VO_2]^+$ cations.[100] The decavanadic acid species $[H_2V_{10}O_{28}]^{4-}$ consists of 10 edge-sharing $[VO_6]$ units, and acts as a reservoir for V^V precursor. Then the spontaneously dissociation of decavanadic acid give rise to the polymerization

of $V_2O_5 \cdot nH_2O$ gels.[101] The conversion reactions during this process can be represented by the following equations:[100]

$$V_2O_5 + 2H^+ + 2H_2O_2 + 3H_2O \longrightarrow 2VO(O_2)(OH_2)_3{}^+ \quad (1.5)$$

$$2VO(O_2)(OH_2)_3{}^+ + H_2O_2 \leftrightarrow VO(O_2)_2(OH_2)^- + 2H^+ + 2H_2O \quad (1.6)$$

$$2VO(O_2)_2(OH_2)^- + 2H^+ \longrightarrow [V(O_2)_2(OH_2)]_2O + H_2O \quad (1.7)$$

$$[V(O_2)_2(OH_2)]_2O + 3H_2O + 2H^+ \longrightarrow 2VO(O_2)(OH_2)_3{}^+ + O_2 \quad (1.8)$$

$$2VO(O_2)(OH_2)_3{}^+ \longrightarrow 2VO_2{}^+ + O_2 + 6H_2O \quad (1.9)$$

$$10VO_2{}^+ + 8H_2O \leftrightarrow H_2V_{10}O_{28}{}^{4-} + 14H^+ \quad (1.10)$$

$$VO_2{}^+ \longrightarrow solid \quad (1.11)$$

Condensation/gelation only occurs when $[VO_2]^+$ species are present in the solution. The exact precursor for the polymerization of $V_2O_5 \cdot nH_2O$ is still unclear, but $[VO_2]^+$ is believed to be involved.[100] According to Livage *et al.*, the neutral species $[VO(OH)_3(OH_2)_2]^0$ ($h=5$) can be a precursor,[98,99] which formed via the hydrolysis of $[VO_2]^+$:[100]

$$VO_2{}^+ + 2H_2O \leftrightarrow H^+ + [VO(OH)_3(OH_2)_2]^0 \quad (1.12)$$

As shown in Figure 1.10, the structure of this six-fold coordinated V^V precursor features one water molecule aligned along the *z*-axis, opposite to the short V=O bond. The other water molecule lies in the *xy* plane, opposite to one OH group. Thus, in the *xy* plane, there is one V–OH_2 and three V–OH bonds, with the *x* and *y* directions being non-equivalent.

When the pH is around 2, condensation occurs via olation and oxolation within the *xy* plane, resulting in a 2-D vanadium oxide network. Olation proceeds along the H_2O–V–OH direction (*b*-axis), leading to the formation of corner-sharing chains. Meanwhile oxolation proceeds along the HO–V–OH direction (*a*-axis), forming edge-sharing double chains. Due to the faster rate of the

olation reaction compared to oxolation, $V_2O_5 \cdot nH_2O$ exhibits a ribbon/fiber-like morphology instead of platelets.

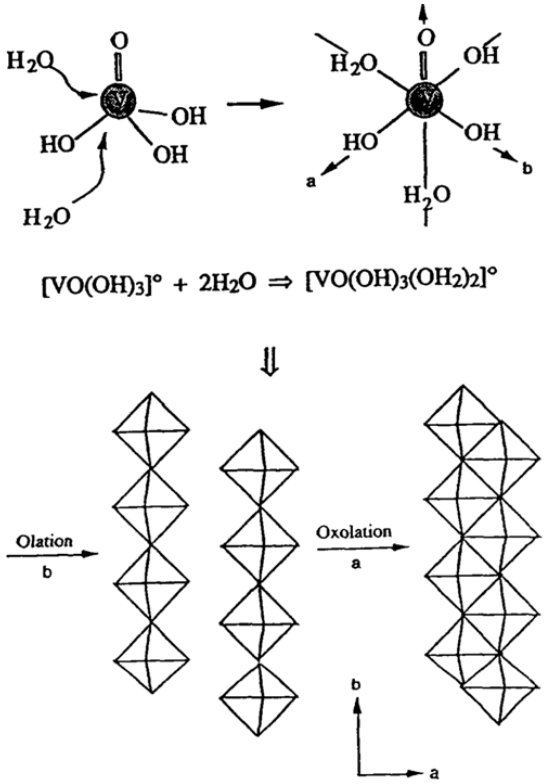

Figure 1.10. Schematic illustration of the $V_2O_5 \cdot nH_2O$ formation via condensation of $[VO(OH)_3(OH_2)_2]^0$. Reproduced with permission from ref [102]. Copyright 2011, The Materials Research Society.

1.3.5 *Ion Exchange and Intercalation Properties of $V_2O_5 \cdot nH_2O$*

$V_2O_5 \cdot nH_2O$ is of particular interest for its ion-exchange properties. At the oxide/water interface of $V_2O_5 \cdot nH_2O$, water absorption and dissociation occur, resulting in the formation of surface hydroxyl groups (–V–OH). These surface hydroxyl groups, influenced by the strong polarizing of small and highly charged V^{5+} ions, then participate in acid dissociation reactions (as below), yielding acid protons:[95,103]

$$V - OH + H_2O \rightarrow V - O^- + H_3O^+ \quad (1.13)$$

This accounts for the acidic and ion-exchange properties of $V_2O_5 \cdot nH_2O$. It has been found that there are two H_3O^+ groups per six $V_2O_5 \cdot nH_2O$ molecules, suggesting a description of $V_2O_5 \cdot nH_2O$ as poly-vanadic acid ($H_2V_{12}O_{31} \cdot nH_2O$).[92] The acid protons (H_3O^+) tend to migrate along the interlayer surface and can be readily exchanged by other ions or molecules, endowing $V_2O_5 \cdot nH_2O$ with intercalation capability.

Intercalation reactions in $V_2O_5 \cdot nH_2O$ are notably faster and easier compared to crystalline V_2O_5, owing to its versatile host structure: the V–O ribbons in $V_2O_5 \cdot nH_2O$ are linked via weakly hydrogen bonded water molecules, and its basal distance is relatively large. Intercalation in $V_2O_5 \cdot nH_2O$ occurs spontaneously at room temperature within a few minutes. The internal structure and the 1-D stacking of V_2O_5 ribbons will not be destroyed, with only basal spacing changing after intercalation.[88]

$V_2O_5 \cdot nH_2O$ gels have demonstrated excellent abilities to intercalate a wide range of ionic species (metal cations, polycations, or organic cations) as well as molecular species (organic molecules). Intercalation of metal cations primarily involves ion exchange reactions with the acid protons of the gel, although redox reactions may also occur, leading to the formation of V^{4+}. The exchange capacity for monovalent cations is close to 0.3, a value that correlates well with the number of acid protons in $V_2O_5 \cdot nH_2O$.[95] The kinetics of exchange reactions are determined by the ion diffusion rate through the gel, rather than the concentration of intercalated ions. [88]

Polar organic solvents can also be intercalated within the layered structure of $V_2O_5 \cdot nH_2O$ through various processes, such as redox reactions, protonation, or dipolar adsorption.[95] Additionally, organic monomers, like aniline and pyrrole, can undergo *in situ* intercalation/polymerization

within $V_2O_5 \cdot nH_2O$. This process is driven by the high redox potential of the gels, leading to the oxidative polymerization of organic monomers into electrically conductive polymers, with some vanadium reduced to V^{4+}.[95]

1.3.6 *Pre-intercalation Strategy*

$V_2O_5 \cdot nH_2O$ has been extensively studied as intercalation host materials for monovalent (Li^+, Na^+, and K^+) and multivalent (Mg^{2+}, Zn^{2+}, and Al^{3+}) ions, owing to its:

(1) 2-D channels with large interlayer spacing: facilitate ion transport.

(2) V^{5+}/V^{4+} and V^{4+}/V^{3+} redox pairs: offer high theoretical capacity.

(3) Interlayer water: help shield the effective charge of Zn^{2+} ions.

(4) Mixed valence states: allow for the hopping of unpaired electrons.

(5) Lack of long-range order: buffer against the strain induced by ion insertion/extraction.

(6) Ion-exchange properties: enable facile structure and chemistry modification.[87]

When used as cathode materials for ZIBs, $V_2O_5 \cdot nH_2O$ typically demonstrates a high initial capacity (> 300 mA h g^{-1} at 0.5 mA g^{-1}).[104,105] However, over cycling, $V_2O_5 \cdot nH_2O$ exhibits significant capacity decay (as shown in Figure 1.11a, b), attributed to the loss of stacking order upon deintercalation of charge carriers.[106] As illustrated in Figure 1.11 c and d, upon insertion of Na^+ ions, the overall structure undergoes re-organization with both long-range and short-range order. However, upon extraction of Na^+ ions, $V_2O_5 \cdot nH_2O$ loses its long-range order, while preserving short-range order. Although this order-disorder transition is believed to be reversible, repeated cycling can intensify this structural change, leading to capability decay.[106] Additionally, another issue contributing to structural degradation is the dissolution of vanadium in aqueous solutions, resulting from the strong polarization of V^{5+} ions and

Lewis acid properties of H_2O. As shown in Figure 1.9, the stable form of vanadium species in weakly acidic aqueous solution is VO_2^+ ($V_2O_5 + 2H^+ = 2VO_2^+ + H_2O$).[107]

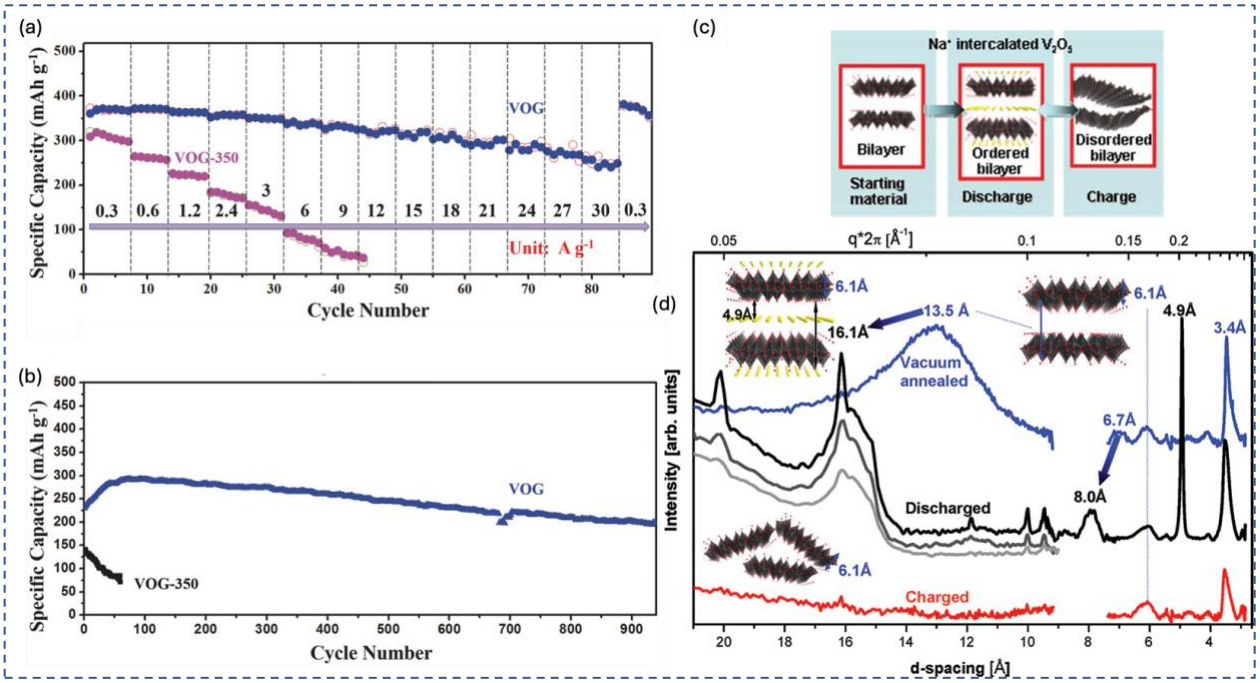

Figure 1.11. (a, b) Electrochemical performance of $V_2O_5 \cdot nH_2O$ in ZIBs. (a) Rate capability at various current densities. (b) Cycling performance at 6 A g^{-1}. (VOG: $V_2O_5 \cdot nH_2O$/graphene, VOG-350: annealing VOG at 350 °C in air). Reproduced with permission from ref [108]. Copyright 2017, WILEY-VCH Verlag GmbH & Co. KGaA, Weinheim. (c, d) Order-disorder transition in $V_2O_5 \cdot nH_2O$ electrodes in sodium ion batteries. (c) Schematic illustration of the structural order change upon Na^+ insertion and extraction. (d) *in situ* (non-operando) small and wide-angle X-ray scattering measurements for the pristine, charged, and discharged $V_2O_5 \cdot nH_2O$ samples. Reproduced with permission from ref [106]. Copyright 2012, American Chemical Society.

For ZIBs, another significant challenge stems from the intrinsic behavior of Zn^{2+} ions. Despite their small ionic radius (0.74 Å), Zn^{2+} ions typically exists in the solvated form of $[Zn(H_2O)_6]^{2+}$ (4.3 Å) in mild aqueous electrolytes.[109–111] The compact size and high charge density of divalent Zn^{2+} cations pose inherent kinetics challenges, including big charge transfer resistance and sluggish diffusion across the electrode interface due to the high de-solvation energy barrier. Additionally, challenges arise from

insufficient capacity resulting from the inadequate utilization of diffusion depth, and cycle life deterioration due to the distortion or collapse of the structure caused by strong electrostatic interactions between Zn^{2+} and the host lattice.[112] Therefore, there is a pressing need for the development of vanadium-based cathodes with a more robust framework, enabling faster, deeper, more stable, and more reversible ion intercalation and de-intercalation.

Various strategies, including defect engineering, nanosizing, doping, surface coating, have been developed to optimize the performance of V-based cathodes.[34] Among these strategies, pre-intercalation of foreign species stands out as one of the most effective and facile one. This approach is not only applicable to vanadium oxides but also to manganese oxides and other tunnel- or layer-structured materials.[113,114] Guest species, including both ionic (main group or transition group ions) and molecular species (organic molecules),[104,105,113,115,116] can undergo pre-intercalation into the tunnels or layers of a material, interacting with the host lattice and charge carriers through chemical bonding, electrostatic interactions, or coordination.[107,117] Generally, the benefits of pre-intercalation strategy include the regulation of interlayer spacing, the strengthening of structural integrity, the reduction of electrostatic interactions between Zn^{2+} ions and the host structure, thereby facilitating fast Zn ion insertion and extraction kinetics.

However, various pre-intercalated guest species exhibit fundamental distinctions, influencing the host structure and its energy storage properties differently. For instance, main group metal ions with low electronegativity tend to form robust bonds with the host lattice, thereby effectively promoting structural stability.[107] Transition metal ions, featured by tunable *d* orbitals, interact with the V 3*d* orbital, thereby shifting the redox couple to a higher level and significantly improving open circuit voltage and operation voltage.[107,118] Organic molecules contribute to a more expanded interlayer

distance (exceeding 13 Å) and effectively alleviate electrostatic interactions between Zn^{2+} and the host structure, facilitating ionic diffusion kinetics and enhancing stability upon cycling.[107,119,120]

1.4 MOTIVATION AND OBJECTIVES

The global shift towards sustainable and renewable energy sources has intensified the demand for efficient and reliable energy storage systems. Among various candidates, aqueous ZIBs stand out due to their inherent safety, cost-effectiveness, and environmental friendliness. The use of air-stable zinc metal anodes and nonflammable water-based electrolytes makes ZIBs particularly promising for large-scale energy storage applications. However, practical deployment of ZIBs is hindered by challenges related to the development of stable and high-performance cathode materials. Hydrated vanadium oxides ($V_2O_5 \cdot nH_2O$) have emerged as potential cathode candidates due to their layered structure and ability to host various guest ions, enhancing their electrochemical properties. This dissertation is motivated by the need to optimize these vanadium-based cathodes through pre-intercalation strategies to improve their stability and kinetics in ZIBs.

The primary objectives of this dissertation are:

First, chemical pre-intercalation of Na^+ ions:

- Investigate the feasibility of pre-inserting metal ions into the $V_2O_5 \cdot nH_2O$ structure.
- Assess the impacts of pre-intercalation on the structural properties of $V_2O_5 \cdot nH_2O$.
- Evaluate how the pre-intercalation approach enhances the electrochemical performance of Na^+ pre-intercalated $V_2O_5 \cdot nH_2O$ in aqueous ZIBs.

Second, comparison of a series of metal species, including monovalent (Na^+, K^+, and Rb^+), bivalent (Mg^{2+}), and trivalent (Al^{3+}) cations:

- Establish correlations between metal cation properties (e.g., size, charge, electronegativity), the structure of $M_xV_2O_5{\cdot}nH_2O$ (morphology, interlayer spacing, structural water content, V^{4+} amount), and their electrochemical performance (capacity, stability, kinetics).

Third, pre-intercalation of large and weakly polarized organic trimethylphenylammonium cations ($TMPA^+$):

- Determine the structural and zinc ion storage capability changes induced by organic cation pre-intercalation.
- Assess whether organic cation pre-intercalation combines the advantages of both ionic and molecular pre-intercalation.

Forth, comparison of different organic species, $CH_3NH_3^+$ and $N(CH_3)_4^+$, with NH_4^+ pre-intercalated vanadium oxide:

- Identify key factors influencing the effects of organic cation pre-intercalation.
- Compare the structure, properties, and electrochemical performance of organic cation preintercalated phases with those metal cation pre-intercalated phases.

By achieving these objectives, this dissertation aims to provide a comprehensive understanding of the pre-intercalation strategies and their potential to enhance the performance of vanadium-based cathodes in aqueous zinc-ion batteries, thereby contributing to the development of efficient and sustainable energy storage systems.

Chapter 2. Experimental Methodology

2.1 Materials Synthesis

In a typical synthesis of guest species pre-intercalated $V_2O_5 \cdot nH_2O$, a facile hydrothermal method is used. In the first beaker, 2 mmol of V_2O_5 powder and 2 mL of H_2O_2 (30 wt.%) are added to 50 mL of deionized water and magnetically stirred for 30 minutes. Meanwhile, in the second beaker, 1 mmol of guest species precursor is dissolved in 30 mL of deionized water and stirred for 30 minutes. Then, the two solutions are mixed and stirred for another 30 minutes. The resulting mixed solution is then transferred and sealed in a 100 mL Teflon-lined stainless-steel autoclave. The hydrothermal synthesis is conducted at 120 °C for 6 hours. After cooling to room temperature, the precipitates are collected by centrifugation, washed with ethanol and deionized water, and then dried in an oven overnight at 60 °C. Finally, the obtained products are further dried in a vacuum oven at 120 °C for 2 hours. For comparison, $V_2O_5 \cdot nH_2O$ was synthesized using the same procedure, but without the addition of pre-intercalated species precursors, and is dried using a freeze dryer instead of an electric oven.

2.2 Materials Characterization

2.2.1 *X-ray Diffraction*

X-ray diffraction (XRD) was employed to analyze the phase and crystal structure of synthesized materials. XRD measurements in this work were performed using a Bruker D8 Discover Powder X-ray diffractometer equipped with a IμS 2-D detection system and utilizing the Cu K-alpha radiation source. The detector angle 2θ ranged from 6–72°. For each sample, the interlayer spacing d will be determined from the (001) diffraction peak using the Bragg's law:

$$n\lambda = 2d \sin\theta \tag{2.1}$$

where λ is the X-ray wavelength (1.542 Å for this X-ray instrument), θ is the incident angle, n is an integer.

2.2.2 *Scanning Electron Microscopy and Transmission Electron Microscopy*

Morphological analysis and elemental composition studies were conducted using a FEI XL30 scanning electron microscope (SEM), which provides high resolution low kV secondary electron imaging and is equipped with an integrated Energy Dispersive X-ray Spectrometer (EDS) from Oxford, offering elemental analysis and mapping. Transmission electron microscopy (TEM) images were obtained either on a JEM-2100F TEM or an FEI Tecnai G^2 F20 SuperTwin 200 keV TEM equipped with an EDAX Elite-T EDS.

2.2.3 *X-ray Photoelectron Spectroscopy*

X-ray photoelectron spectroscopy (XPS) was conducted using a Kratos AXIS Ultra DLD instrument to identify elements and their chemical states on the sample surface through the photoelectric effect. In this study, XPS was mainly instrumental in quantifying the content of V^{4+} and determining the average oxidation state of vanadium. Additionally, XPS provided valuable bonding information regarding interactions between pre-intercalated foreign species and the vanadium oxide network. The collected XPS data were calibrated based on adventitious carbon with a binging energy of 285.0 eV.

2.2.4 *Thermogravimetric Analysis/Differential Scanning Calorimetry*

A dual thermogravimetric analysis and differential scanning calorimetry instrument (Mettler Toledo TGA/DSC 3+) was used to explore the thermal stability and structural water content of the synthesized materials. In this study, TGA/DSC tests were performed within a temperature range of 30–700 °C with a heating rate of 10 °C/min. The experiments were conducted in either air (for

organic cation-preinserted VOH) or a N_2 atmosphere (at a flow rate of 50 ml/min, for metal cation-preinserted VOH).

2.2.5 *Raman Spectroscopy*

Raman spectroscopy offers useful information on the type and characteristics of chemical bonds within the investigated materials, relying on the interaction of light with matter. Ramen spectra were collected in the range of 100-1200 cm^{-1} using a Renishaw InVia Raman Microscopy system equipped with the Leica DMIRBE inverted optical microscope. An Ar^+ laser excitation sources at 514 nm was employed for the measurements.

2.2.6 *Fourier-Transform Infrared Spectroscopy*

Fourier transform infrared spectroscopy (FTIR) was employed to confirm the presence of functional groups and detect local changes in the bonding environment of specific bonds. In this study, FTIR was used to confirm the presence of pre-intercalated organic functional groups, and to determine the bonding characteristics between pre-intercalated species and the V–O matrix. FTIR spectra were collected in the wavelength range of 500 to 4000 cm^{-1} using a Thermo Scientific Nicolet iS10 FT-IR instrument with laser excitation source at 514 nm.

2.3 ELECTROCHEMICAL CHARACTERIZATION

2.3.1 *Electrochemical Testing Setup*

For aqueous ZIBs, the cathode was prepared by blending the synthesized active material, conductive agent (carbon black), and binding agent (polyvinylidene fluoride, PVDF, dispersed in N-Methyl-2-Pyrrolidone (NMP) solvent) in a weight ratio of 7:2:1. The resulting slurry was then coated onto a titanium foil current collector (with a diameter of 10 mm) and air-dried at 60 ˚C. The

fully dried electrodes were then transferred to a vacuum oven for further drying at 120 ˚C for 12 hours. The mass loading of the active materials was about 1.5-2.5 mg·cm^{-2}.

For aqueous ZIBs, zinc metal foil (Thermo Scientific) was cut into the 12 mm circular disk and used as the anode. Glass fiber (Whatman, Grade GF/A) served as the separator, and a 3 M zinc trifluoromethanesulfonate ($Zn(CF_3SO_3)_2$, 98%) aqueous solution was used as the electrolyte. CR2032 type coin cells were assembled according to the configuration depicted in Figure 2.1.

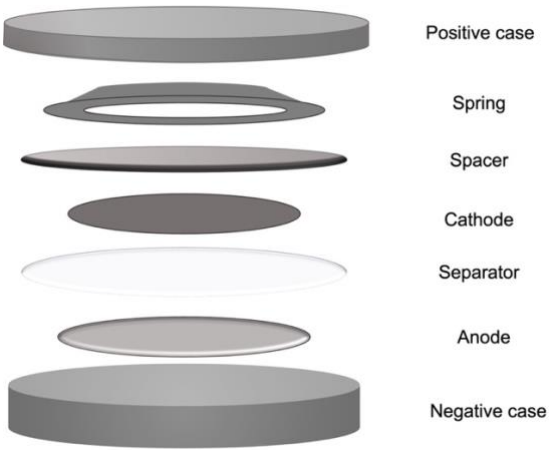

Figure 2.1. Schematic illustration of the CR2032 coin cell assembly.

2.3.2 *Galvanostatic Charge-Discharge Test*

In this study, galvanostatic charge-discharge (GCD) tests were carried out using a NEWARE electrochemical testing station. During a GCD test, a constant current is applied to charge or discharge the coin cell within a predetermined voltage range (0.2–1.6 V vs. Zn^{2+}/Zn), while the voltage variation over time is recorded. The data derived from GCD tests can be used to evaluate specific capacity, coulombic efficiency, cycling stability, and rate capability, using the following equations:

$$\text{Specific capacity (mA h g}^{-1}) = \frac{I(mA) \times t(h)}{m\,(g)} \qquad (2.2)$$

where I (mA) is the applied current, t (h) is discharge/charge time, m (g) is the mass of the active material.

$$\text{Coulombic Efficiency (\%)} = \frac{Discharge\ capacity}{Charge\ capacity} \times 100\% \quad (2.3)$$

$$\text{Energy efficiency (\%)} = \frac{Discharge\ specific\ energy}{Charge\ specific\ energy} \times 100\% \quad (2.4)$$

Cycling stability can be evaluated by plotting the specific capacity *vs*. cycle number, and calculating the capacity retention of the N^{th} cycle by:

$$\text{Capacity retention (\%)} = \frac{Specific\ capacity\ of\ the\ N^{th}\ cycle}{Highest\ specific\ capacity} \times 100\% \quad (2.5)$$

Rate capability can be investigated by performing the GCD tests at different current densities (0.5, 1.0, 2.0, 4.0, and 8.0 A g^{-1}), and evaluated as:

$$\text{Rate capability (\%)} = \frac{Specific\ capacity\ at\ 8.0\ A g^{-1}}{Specific\ capacity\ at\ 0.5\ A g^{-1}} \times 100\% \quad (2.6)$$

2.3.3 *Cyclic Voltammetry*

Cyclic voltammetry (CV) is used to investigate the redox reactions, overpotentials, reversibility, and charge storage kinetics. In a CV test, the cell is cycled within a specific voltage window (0.2–1.6 V vs. Zn^{2+}/Zn in this work) at a constant scan rate (mV s^{-1}), and the data is typically presented as response current or current density *vs*. applied voltage. In this research, CV tests were carried out using the Solartron electrochemical working station (SI 1287).

To study the electrochemical kinetics, CV tests were conducted at various scan rates (0.1, 0.2, 0.3, 0.5, 0.8, and 1.2 mV s^{-1}) The total current can be decomposed into two components: a slow diffusion-controlled process (i_{diff}) and a fast surface-controlled capacitive process (i_{cap}), according to the following empirical equation:[121]

$$i(v) = i_{cap} + i_{diff} = av^b \quad (2.7)$$

$$\log i(v) = \log a + b \log v \quad (2.8)$$

Where both *a* and *b* are adjustable parameters. The *b*-value can be derived from the slope of the plot of log *i* vs. log *v*. Generally, the *b*-value varies in the range of 0.5-1.0, and there are two well defined conditions: *b*-value = 0.5 and *b*-value = 1.0. A *b*-value of 0.5 represents a complete diffusion-controlled redox charge storage, promoted by the faradaic intercalation/de-intercalation of charge carriers; while a *b*-value of 1.0 is indicative of a fast surface-controlled capacitive charge storage, resulting from the pseudocapacitance formed via the adsorption and desorption of charge carriers at the near surface of the electrode. Generally, the larger the *b* value is, the larger the contribution from capacitive process.

Notice that the capacitive-controlled current varies linearly with the sweep rate *v*, while the diffusion-controlled current obeys a linear relationship with $v^{1/2}$. So, the contribution of each component can be determined based on the following equations:[121]

$$i\,(v) = i_{cap} + i_{diff} = k_1 v + k_2 v^{\frac{1}{2}} \tag{2.9}$$

$$i\,(v)/v^{\frac{1}{2}} = k_1 v^{\frac{1}{2}} + k_2 \tag{2.10}$$

By plotting $i\,(v)/v^{\frac{1}{2}}$ vs. $v^{\frac{1}{2}}$, the coefficients k_1 and k_2 can be determined from the slope and intercept of the line, providing insights into the relative contributions of capacitive effect ($k_1 v$) and diffusion-controlled processes ($k_2 v^{1/2}$).

The charge storage can be estimated by:

$$Q = \frac{\int i(E)dE}{2mv} \tag{2.11}$$

Where Q is the average charge during the charge/discharge process (C/g), *m* is the mass of the active material (g), *i* is the current response (A), *v* is the scan rate (V s^{-1}). Then the diffusion-controlled and capacitive controlled charge storage can be quantified.

2.3.4 *Electrochemical Impedance Spectroscopy*

Electrochemical impedance spectra (EIS) were measured in a frequency range from 10^5 to 0.01 Hz, with an AC amplitude of 5 mV. This wide frequency range allows for the discrimination of different charge transfer processes and mass transport effects, each exhibiting distinct time behaviors ranging from very fast to very slow. The electrochemical process can be visualized using an equivalent circuit, where each component represents a specific physical aspect of the system.

As depicted in the Nyquist plot in Figure 2.2, the intersection of the semicircle with the *x* axis at the highest frequency represents the total resistance (R_u) from electrolytes and the electrode surface. The diameter of the semicircle in the middle frequency region corresponds to the charge transfer resistance (R_{ct}) in the electrodes. The straight line at low frequency (< 1 Hz) is associated with the slow mass transfer process, which can be represented by a complex resistive element, W (Warburg element).

The ion diffusion coefficient can be calculated in the Warburg region by:[122,123]

$$D_{Zn^{2+}}^{EIS} = \frac{1}{2}\left[\left(\frac{V_M}{AF\sigma_W}\right) \times \left(\frac{\partial E}{\partial x}\right)\right]^2 \quad (2.12)$$

$$D_{Zn^{2+}}^{EIS} = \left(\frac{RT}{\sqrt{2}An^2F^2C\sigma_W}\right)^2 = 3.54 \times 10^{-14}(An^2C\sigma_W)^{-2} \quad (2.13)$$

where R is the gas constant, T is the absolute temperature, F is the Faraday constant, A is the contact area of electrode/electrolyte, *n* is the charge transfer number, *C* is the concentration of charge carriers in the electrolyte, σ_w is the Warburg coefficient, which can be obtained from the slope of Z' vs. $\omega^{-1/2}$ plot in the Warburg region (1-0.1 Hz).

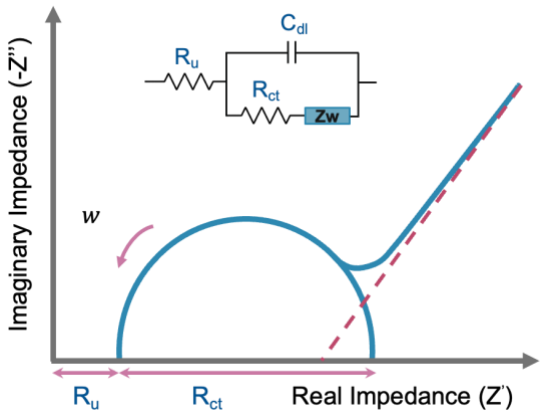

Figure 2.2. A typical Nyquist plot and its Randles equivalent circuit.

2.3.5 *Galvanostatic Intermittent Titration Technique*

The Galvanostatic Intermittent Titration Technique (GITT) was employed to determine the ion diffusion coefficients during the charging/discharging process. In a GITT test, a current pulse of 50 mA g^{-1} was applied for an interval of 600 s, followed by a relaxation time of 600 s to allow the cutoff voltage to reach equilibrium. The chemical diffusion coefficient of Zn^{2+} ions ($D_{Zn^{2+}}$) in cathode materials can be calculated using the following equation:[124]

$$D_{Zn^{2+}}^{GITT} = \frac{4}{\pi\tau}\left(\frac{m \cdot V_M}{M \cdot S}\right)^2 \left(\frac{\Delta E_s}{\Delta E_\tau}\right)^2 \left(\tau \ll \frac{L^2}{D}\right) \quad (2.14)$$

Where τ (s) is the current pulse duration time; m, M, and V_M are the mass (g), molar weight (g mol^{-1}), and molar volume (cm^3 mol^{-1}) of the active materials, respectively; S (cm^2) is the contact area of the electrode/electrolyte interface; ΔE_s (V) is the steady state voltage change; ΔE_τ (V) is the total voltage change during a current pulse, neglecting the IR-drop.

The internal resistance (Ω) is calculated from the IR drop by:[125]

$$\text{Internal resistance}(\Omega) = \frac{IR\ drop}{i} \quad (2.15)$$

Where *i* is the applied constant current during current pulses (A), and IR (V) is illustrated in Figure 2.3:

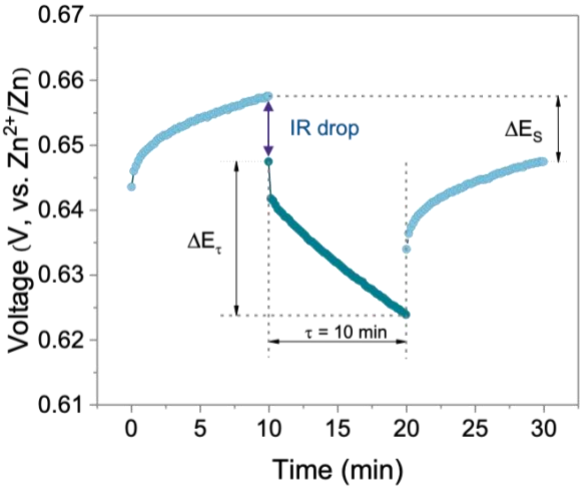

Figure 2.3. Schematic illustration of ΔE_τ, ΔE_s, and IR drop in a GITT test.

Chapter 3. How Chemical Pre-intercalation Works

Adapted with permission from Xiaoxiao Jia, Ruixue Tian, Chaofeng Liu, Jiqi Zheng, Meng Tian, and Guozhong Cao. "Stability and kinetics enhancement of hydrated vanadium oxide via sodium-ion pre-intercalation." *Materials Today Energy* 28, 101063 (2022). https://doi.org/10.1016/j.mtener.2022.101063.

3.1 Background and Approach

Pre-intercalation of metal cations has been recognized for modifying interlayer spacing and tuning the structure of $V_2O_5{\cdot}nH_2O$ phase, leading to higher capacities and improved cycling stability. Despite its widespread use, the specific mechanisms behind these enhancements have not been systematically investigated. Most studies attributed the enhanced performance of pre-intercalated $V_2O_5{\cdot}nH_2O$ to the increased lattice spacing and the pillar effect of the pre-intercalated species.[126,127] However, some work, contradicted this explanation by showing that reduced interplanar spacing, as seen with K^+ cations, can also improve the zinc ion storage capacity and cycling stability.[105]

This chapter focuses on the use of Na^+ as an example to illustrate the effects of pre-intercalating metal cations. The study investigated the cation-exchange mechanism in $V_2O_5{\cdot}nH_2O$, the interplay between interlayer water and pre-intercalated metal cations, and factors affecting electrochemical performance beyond interlayer distance. The goal is to define material properties that enhance the electrochemical performance of $V_2O_5{\cdot}nH_2O$ in aqueous ZIBs, such as the amount of tetravalent vanadium ions, and the content of interlayer water.

3.2 MATERIALS CHARACTERIZATION

The SEM image (Figure 3.1a) shows that the Na^+ preintercalated $V_2O_5 \cdot nH_2O$ phase (NaVOH) has a highly interweaved foam-like architecture, built from ultrathin nanoribbons. In the HRTEM image of NaVOH, a set of lattice fringes with a interplanar spacing of 2.17 Å (Figure 3.1b) is observed, which corresponds to the (005) planes of NaVOH and agrees well with the peak at 41.1° from XRD (d_{005} = 2.19 Å). Another set of lattice fringes, which are perpendicular to that of (005) planes, shows an interplanar spacing of 1.96 Å and corresponds to the spacing of (510) plane of NaVOH. The TEM-EDS elemental mapping images (Figure 3.1c) reveal the homogenous distribution of the Na, V and O in the NaVOH nanoribbons, confirming the successful introduction of Na ions in the VOH. From the EDS spectra of NaVOH, the absence of sulfur peaks (S) confirms that all unreacted Na_2SO_4 salts was removed upon washing and centrifuging. All sodium here is the chemically preintercalated Na^+ ions in NaVOH. The Na:V ratio in NaVOH is estimated to be 1:7.5, with a chemical formula of δ-$Na_{0.27}V_2O_5 \cdot nH_2O$.

Figure 3.1d shows the XRD patterns of NaVOH and VOH. Diffraction peaks of VOH could be well indexed to the standard $V_2O_5 \cdot 1.6H_2O$ pattern (JCPDS No.40-1296).[115] The pronounced (00*l*) diffraction peaks of two samples indicate a typical layered structure along *c*-axis. The structure of hydrated vanadium pentoxide has double V_2O_5 sheets, which is constructed by the square pyramidal [VO_5] units and the octahedral [VO_6] units, and contains interlayer guest cations/water molecules (as shown in the inset of Figure 3.1d).[87] NaVOH exhibits almost the same characteristic peaks as that of VOH, suggesting that the bilayered structure of VOH is well-preserved after the introduction of Na^+ cations. The (001) peak of NaVOH (2θ = 8.1°) shifts towards a higher degree comparing to that of VOH (2θ = 7.3°), which corresponds to a decreased interlayer spacing of NaVOH (NaVOH: 11.0 Å, VOH: 12.0 Å).

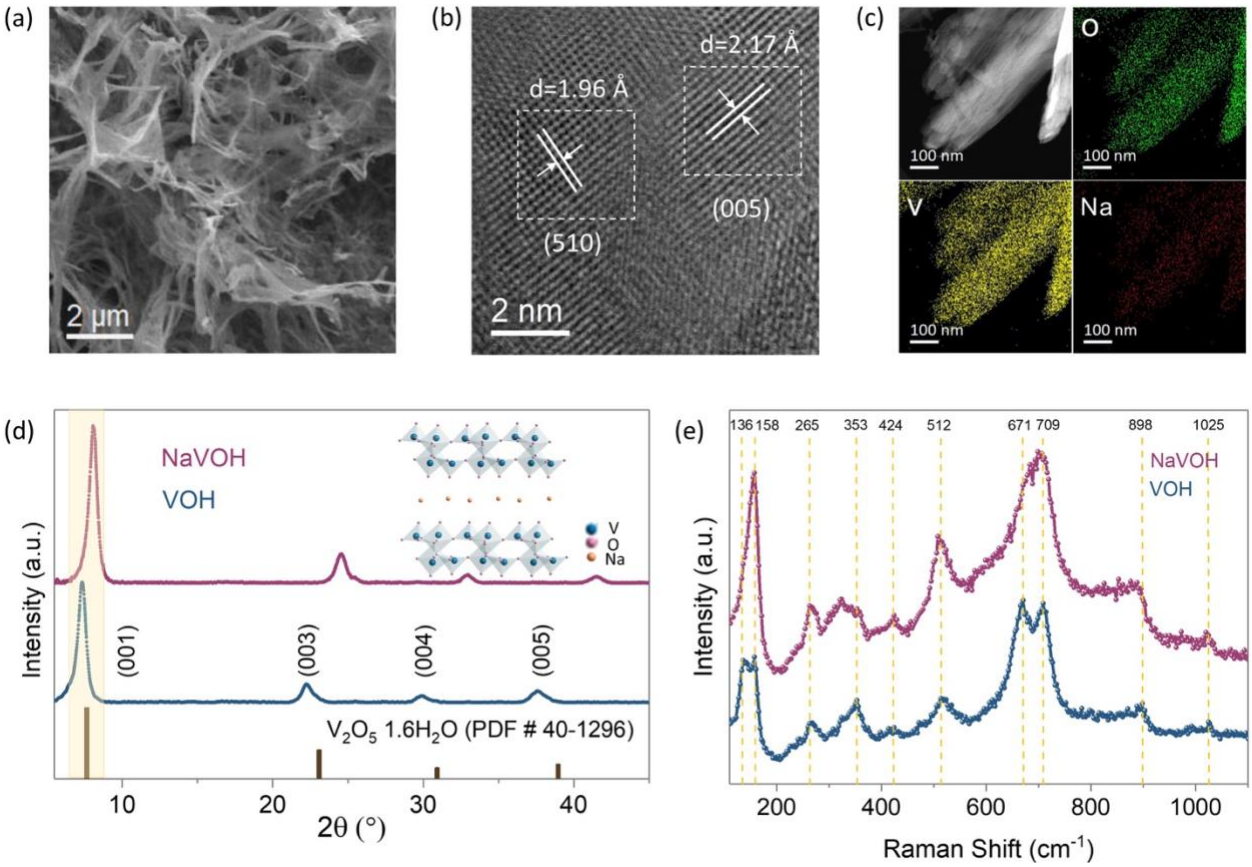

Figure 3.1. (a) SEM image, (b) HR-TEM image, and (c) TEM image with the corresponding EDS elemental mappings of NaVOH. (d) XRD patterns of NaVOH and VOH, with a schematic diagram of the NaVOH crystal structure (inserted). (e) Raman spectra of NaVOH and VOH.

Raman spectra of NaVOH is very similar to that of VOH (shown in Figure 3.1e) and the assignment of the observed modes is given in Table *3.1*. For VOH, the highest frequency mode at 1025 cm^{-1} is attributed to the stretching of the strongest V=O bonds in [VO_5]; the bending of those V=O bonds occurs at around 265 and 424 cm^{-1}.[128] The peak at 898 cm^{-1} in VOH is characteristic of the V-OH_2 stretching vibration.[129] The corresponding mode in NaVOH exhibits a much decreased intensity, suggesting a reduced amount of interlayer water in NaVOH. This is supported by the peak at 353 cm^{-1}, which is attributed to the lattice water vibration.[129] The peak at 709 cm^{-1} for VOH originates from the stretching vibration of V_2–O bonds (doubly coordinated oxygen),[128] whereas the one located at 671 cm^{-1} corresponds to those disordered V_2–O.[130] Such split peak was

not observed in NaVOH. Only a single broad peak was detected at 699 cm^{-1}, suggesting a more ordered vanadium oxide structure due to Na^+ introduction.[105] The peak at 512 cm^{-1} is assigned to the V_3–O (triply coordinated oxygen) stretching vibration.[131] The low-frequency peak at 158 cm^{-1} is associated with the bending vibration of –V–O–V–O– chains.[105,128] VOH exhibits one additional peak at 136 cm^{-1}, which comes from the chain vibration subjected to the compressive deformation along ***a*** direction.[132]

Table 3.1. The observed Raman peak positions and their assignments for VOH and NaVOH.

Frequency/cm^{-1}		Assignment (vibration mode)
NaVOH	VOH	
---	136	-V-O-V-O chain vibration
157	158	-V-O-V-O chain vibration
263	265	V=O bending
424	424	V=O bending
353	353	lattice water vibration
508	512	V_3-O stretching
--	671	V_2-O stretching in distorted V-O-V framework
699	709	V_2-O stretching
898	898	V-OH_2 stretching
1020	1025	V=O stretching

Thermal stability and hydration degree (n in δ-$Na_xV_2O_5{\cdot}nH_2O$) of the samples were examined by TGA and DSC analysis. Figure 3.2a shows there are weight losses with an increasing temperature, attributing to two kinds of interlayer water in $V_2O_5{\cdot}nH_2O$. One is that leaves at 120°C; this is the physically adsorbed and weakly bound water, the amount of which is determined by the water

pressure in the environment. The other type leaves at 250 °C, which corresponds to the water that chemically and tightly bonded to the vanadium oxide network.[95,133,134] According to the weight loss during the two stages, the corresponding water removal process for NaVOH and VOH can be expressed as follows:

$$Na_xV_2O_5 \cdot 0.7H_2O \xrightarrow{120℃} Na_xV_2O_5 \cdot 0.07H_2O \xrightarrow{250℃} Na_xV_2O_5 \quad (3.1)$$

$$V_2O_5 \cdot 1.0H_2O \xrightarrow{120℃} V_2O_5 \cdot 0.38H_2O \xrightarrow{250℃} V_2O_5 \quad (3.2)$$

Overall, the H_2O content of NaVOH and VOH is estimated to be n=0.7 and n = 1.0, respectively. This number is smaller than that in $V_2O_5 \cdot 1.6H_2O$ (n=1.6), as the samples were heated to 120 °C for 2 h prior to the TGA test. A smaller amount of water situated between the bilayers in NaVOH explains its narrower interlamellar spacing than that of VOH. A sharp exothermic DSC peak is observed at ~350 °C for both VOH and NaVOH, which corresponds to the crystallization of the orthorhombic V_2O_5 due to some local reorganizations.[135] The DSC curve of VOH showed a sharp endothermic peak at 679°C, which is assigned to the melting of V_2O_5. It is found that the decomposition of NaVOH does not start within the range of testing temperature, suggesting its better thermal stability than VOH. From the temperature range of 120 to 200°C, it can be estimated that the two samples have the same amount of physically adsorbed H_2O per V_2O_5 (n=0.62), because they were synthesized under the same H_2O vapor pressure. In the second phase (250~400 °C), notably, for VOH, the mass loss is about 3.6%, corresponding to n=0.38 water bonded to the vanadium oxide network. The weight loss of NaVOH during this stage, however, is very limited, suggesting a negligible amount of chemically bonded water in NaVOH (only ~0.07). This probably arises from the replacement of structural water by the intercalated foreign cations (Na^+ ions in our case).

According to Livage *et al.*,[95,103] when water molecules is adsorbed between bilayers, surface hydroxyl groups could be easily involved in the acid dissociation reactions to produce solvated protons ($-V-OH+H_2O \rightarrow -V-O^- + H_3O^+$). These acid protons ($H_3O^+$) tend to move along the bilayer surface and can be easily replaced by the other cations or molecules, endowing VOH with ion-exchange properties. Our thermogravimetric results (Figure 3.2a) reveal that approximately 0.31 water per V_2O_5 was removed when Na^+ ions were preintercalated. This value is in line with the literature data that there is 0.3 H_3O^+ per V_2O_5, and the exchange capacity of $V_2O_5 \cdot nH_2O$ with respect to the monovalent metal cations is about 0.3.[92,95]

The XPS survey spectrum (Figure 3.2b) reveal the embedment of Na^+ into the lattice of NaVOH, where a clear Na 1*s* spectrum is detected at 1071.5 eV. The V $2p_{3/2}$ spectra reveal a mixed V^{5+} and V^{4+} valence states in both NaVOH and VOH samples (Figure 3.2c). The peak centered at a higher binding energy of 517.4 eV was ascribed to the oxidation state of V^{5+}, while a lower binding energy of 516.3 eV was assigned to V^{4+}.[115,136] The molar ratio of V^{4+}/V^{5+} is determined to be 1:7 in NaVOH and 1:10 in VOH, suggesting an average oxidation state of $V^{4.88+}$ and $V^{4.91+}$ for NaVOH and VOH, respectively. The results of XPS confirm the increased concentration of lower valent vanadium in NaVOH.

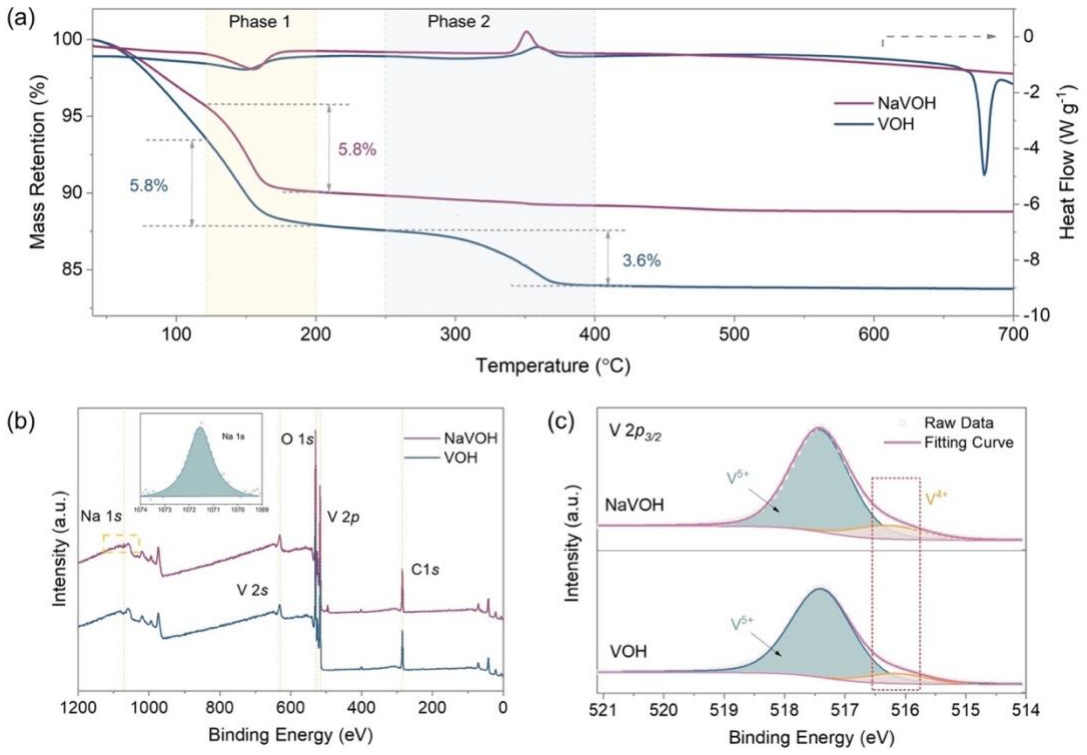

Figure 3.2. (a) TGA/DSC curves of NaVOH and VOH within 30–700 °C. (b) XPS survey spectra, high resolution of Na 1*s* spectra (inserted) and (c) V 2$p_{3/2}$ spectra of NaVOH and VOH.

3.3 Replacement of Interlayer H_3O^+ by Na^+ Pre-insertion

To verify the feasibility of Na^+ pre-intercalation in VOH and its substitution of interlayer water, we performed the first-principals calculations. In $V_2O_5{\cdot}nH_2O$, due to the strong polarizing power of V^{5+}, the coordinate water molecules can undergo acid dissociation reactions on the interlayer surface ($[V(OH_2)_6]^{5+} + hH_2O \Rightarrow [V(OH)_h(OH_2)_{6-h}]^{(5-h)+} + hH_3O^+$), leading to the formation of H_3O^+ ions.[92,95,98] In the calculation model of VOH, there is one H_3O^+ per five H_2O.[133] For the calculations of NaVOH, we replaced one of the H_3O^+ in VOH with one Na atom.

The first-principles calculations were based on the density functional theory (DFT) using the CASTEP code incorporated in Materials Studio.[137] The electron-ion interactions were described with the

projector augmented wave (PAW) potentials.[138] The electronic exchange-correlation was treated by generalized gradient approximation (GGA) in the scheme of Perdew-Burke-Ernzerhof (PBE) functional with a cutoff energy of 500 eV.[139] The DFT + U approach was applied to describe the on-site Coulomb interactions for the V 3*d* states with the U value of 3.0 eV as previously suggested.[140,141] The computational model includes 8 V_2O_5 units and 14 H_2O molecules. The 8 V_2O_5 units match 1 × 2 × 1 supercell of bilayer V_2O_5 or 1 × 2 × 2 supercell of bulk α-V_2O_5. Brillouin zone was sampled by Monkhorst-Pack with a 3 × 5 × 3 *k*-point for geometry optimization, and a dense 5 × 15 × 5 *k*-point was utilized for electronic density of states (DOS). Semi-empirical dispersion potential of the Grimme DFT-D2 correction was employed to accurately estimate van der Waals (vdW) interaction.[142] Both the atomic positions and lattice constants were fully relaxed, and the convergence threshold was set to be 10^{-4} eV per atom in energy and 0.02 eV/Å in force.

The formation energy (E_f) of replacement of one H_3O^+ with one Na^+ was calculated according to the equation:

$$E_f = E_{NaVOH} - E_{VOH} + E_{H_3O^+} - E_{Na^+} \quad (3.3)$$

where E_{NaVOH} and E_{VOH} are the energies of VOH with or without Na^+ insertion, respectively. $E_{H_3O^+}$ and E_{Na^+} are the energies of H_3O^+ and Na^+, respectively.

Table 3.2. The optimized lattice parameters of VOH and NaVOH for theoretical calculations.

	a	b	c	α	β	γ
VOH	12.006	7.262	11.864	88.468	92.472	90.813
NaVOH	12.013	7.247	11.798	88.618	92.722	90.854

The optimized lattice parameters of the VOH and NaVOH structure demonstrate that the interlayer distance (lattice parameter *c*) slightly decreases after Na^+ insertion (as summarized in Table 3.2), which

agrees well with the XRD results of our samples. The formation energy of replacing one H_3O^+ with one Na^+ is calculated to be –0.46 eV, thus confirming that the pre-intercalation of Na^+ ions into VOH is an energetically favorable/spontaneous process. A lower energy of NaVOH also suggests its enhanced thermal stability. This is supported by the TGA results that the decomposition of VOH starts at 679°C, while that of NaVOH does not occur in the range of our testing temperature (30-700°C). The total density of states (TDOS) of NaVOH and VOH (Figure 3.3a) show that, substituting one H_3O^+ with one Na^+ shifts the conduction bond to the left towards the Fermi level. The reduced band gap of NaVOH means the easier excitation of electrons to the conduction band, indicative of an improved electronic conductivity of NaVOH. The bonding interactions between Na^+ and VOH can be seen from the projected density of states (PDOS) (Figure 3.3b). The overlap between the electronic states of Na and the V and O atoms demonstrates the covalent hybridization interactions between inserted Na and the VOH structure.

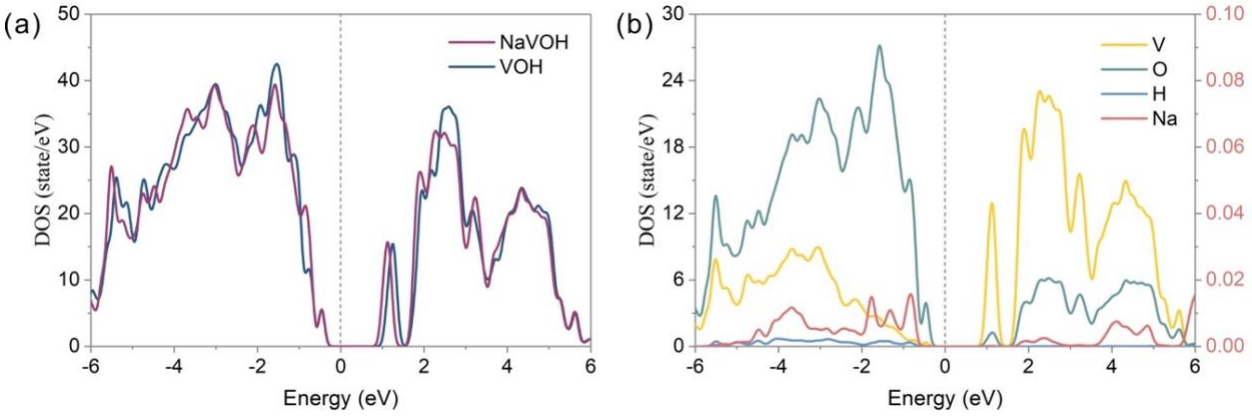

Figure 3.3. (a) The TDOS of VOH and NaVOH. (b) The PDOS of NaVOH, the left axis (black) is the density of states of V, O and H atoms, the right axis (pink) is the DOS of the Na atom. The Fermi energy has been shifted to zero, denoted by the dotted line.

The charge density difference was then calculated to clarify the bonding nature of Na with the adjacent atoms in NaVOH. As shown in Figure 3.4, there is a depletion of electron density (blue region) around

Na and an enrichment of electron density (yellow region) around V and O. This indicates the obvious charge transfer between Na and the surrounding atoms, revealing the formation of ionic bonds between the inserted Na and the host. Quantitatively, the Bader charge analysis confirms there is ~0.9 |e| transferred from Na to the nearby V and O, demonstrating that Na is strongly ionized. In summary, the DFT results show that, by replacing water (H_3O^+) in the interlayer space, the intercalation of Na ions in VOH is thermodynamically favorable and is accompanied by an improved thermostability and electronic conductivity. In addition, strong chemical bonds (predominantly ionic) will form between Na and the VOH structure, contributing to the enhanced host structure stability. These results confirm the Na^+ replacing water mechanism, clarify the benefits of Na^+ pre-intercalation, and help explain the origin of the better Zn^{2+} storage performance in NaVOH.

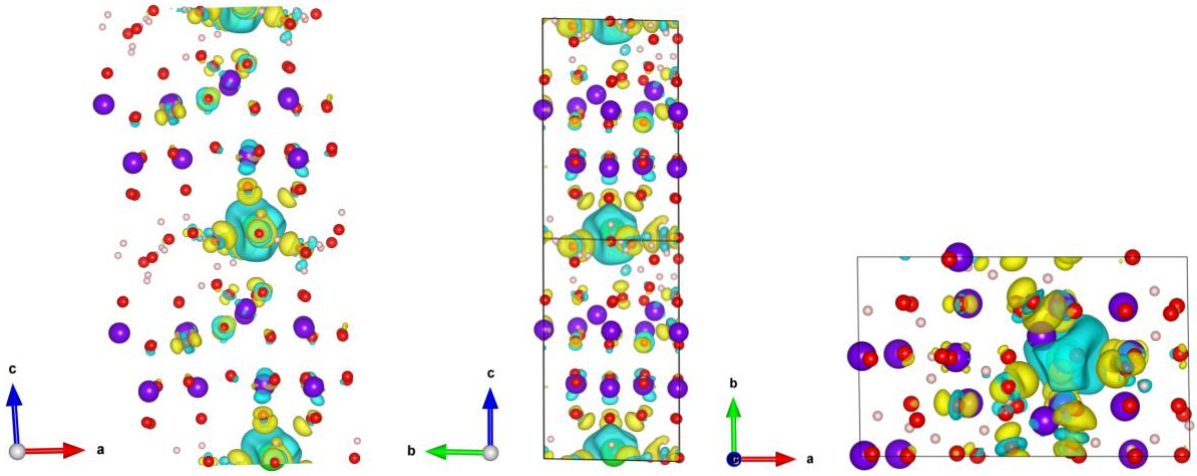

Figure 3.4. The charge density difference of NaVOH on the different side views, showing the electrostatic interactions of Na atoms with the adjacent atoms. The yellow and blue regions correspond to the electron density enrichment and electron density depletion, respectively. (V: purple, O: red, H: pink: Na: green)

3.4 ELECTROCHEMICAL PERFORMANCES

Figure *3.5a* shows the initial three CV profiles of Zn//NaVOH cells tested within the voltage range of 0.2–1.6 V (vs. Zn^{2+}/Zn) at a scan rate of 0.1 mV s^{-1}. Two pairs of well-defined redox peaks are observed at around ~1.0 and 0.5 V, which are ascribed to the redox reactions between V^{5+}/V^{4+} and V^{4+}/V^{3+} pairs, respectively.[104] The well overlapped CV profiles for the first three cycles suggest a highly reversible electrochemical Zn^{2+} insertion/extraction process in NaVOH. For comparison, the 3rd cycle of CV curves for NaVOH and VOH are shown in Figure *3.5b*. They exhibit similar shapes and have peaks at the similar positions, indicating that the redox reactions during the electrochemical Zn^{2+} ion intercalation/de-intercalation are the same for both materials. The difference between two samples is that NaVOH possess a larger current response and a larger integrated area of CV curves in comparison to that of VOH (as summarized in Table 3.3), indicating a larger capacity of NaVOH. Also, the smaller voltage gaps between each pair of redox peaks of NaVOH than those of VOH reflect the lower polarization, a better reversibility, thus the better electrochemical kinetics of NaVOH electrodes.

Table 3.3. A comparison of peak positions and voltage gaps between redox pairs of NaVOH and VOH.

Sample	Redox Pairs (V)	Peak Voltages (V)	Peak Separation (V)	Central Position (V)
VOH	V^{5+}/V^{4+}	0.96/1.12	0.16	1.04
	V^{4+}/V^{3+}	0.46/0.70	0.24	0.58
NaVOH	V^{5+}/V^{4+}	0.98/1.05	0.07	1.02
	V^{4+}/V^{3+}	0.48/0.57	0.09	0.52

Figure *3.5*c compares the GCD curves of NaVOH and VOH at 0.05 A g^{-1}. Both NaVOH and VOH display two pairs of charge/discharge plateaus (1.1–0.9 and 0.7–0.4 V), which agree well with the two pairs of redox peaks shown in CV curves (Figure *3.5*b). For NaVOH, the potential gap between the charge/discharge plateaus is smaller than that of VOH, also in good agreement with the narrower peak separation from the CV curves. In the 1st cycle, NaVOH delivers an initial discharge capacity of 420 mA h g^{-1}, much higher than that of VOH (324 mA h g^{-1}). After 50 cycles, the GCD curve of NaVOH remains almost unchanged, while VOH shows an obviously enlarged overpotential and a significant capacity decay, indicating a more reversible Zn^{2+} intercalation/de-intercalation and better cycling stability of NaVOH.

Rate responses of NaVOH and VOH are compared in Figure *3.5*d. The discharge capacities of Na-preinserted V_2O_5 at 0.5, 1.0, 2.0, 4.0 and 8.0 A g^{-1} are 395, 375, 348, 310, and 262 mA h g^{-1}, respectively. Even when the current density increases to 8.0 A g^{-1}, it still delivers a high reversible capacity of 262 mA h g^{-1}, achieving a capacity retention of 66% (with respect to the capacity at 0.5 A g^{-1}). When the rate returns to 0.5 A g^{-1}, a reversible capacity of 385 mA h g^{-1} can be recovered, indicating a good structure stability and the high electrochemical reversibility of NaVOH. The VOH cathode, in comparison, supplies a smaller capacity than that of NaVOH at all current densities, and it has only 57% capacity retention when the current density increases from 0.5 to 8.0 A g^{-1}.

Besides specific capacity/energy, another critical factor to be considered for the large scale energy storage application is energy efficiency, which is defined as the ratio of the discharged energy density to the charged energy density.[143] As presented in Figure *3.5*e, at a current rate of 0.05 A g^{-1}, the energy efficiency of NaVOH is 88%, much higher than that of VOH (78%), and this value drops slightly for NaVOH (64%) while rapidly for VOH (50%) when the current rate increases to

8.0 A g^{-1}, again revealing the higher reversibility and faster kinetics of Zn^{2+} insertion/extraction in NaVOH. The long-term cycling performance of the Zn//NaVOH and Zn//VOH cells were evaluated at a high current density of 4.0 A g^{-1} (Figure *3*.5f). The discharge capacity of NaVOH gradually increases in the initial 150 cycles and stabilizes at 310 mA h g^{-1}. After 2000 cycles, a high specific capacity of 274 mA h g^{-1} can still be maintained for NaVOH (with a capacity retention of 88%). This is much higher than that of VOH, whose specific capacity decreases sharply from 186 mA h g^{-1} to 79 mA h g^{-1} with a capacity retention of only 43%.

NaVOH samples show good performance in both rate capability and cycling stability compared with that of VOH, which can be attributed to the substitution of partial interlayer water by Na^+ ions and the introduction of more tetravalent vanadium in NaVOH. Interlayer Na^+ ions can form stronger chemical bonds with the V–O framework than interlayer water molecules, which helps to better maintain the layered structure during cycling. The presence of more V^{4+} can facilitate the electronic hopping between V^{4+} and V^{5+} and weaken the electrostatic interactions between carrier ions and the host lattice. Both factors are beneficial to the ionic and electronic diffusion and contribute to a suppressed structural distortion during the repeated Zn^{2+} intercalation and deintercalation.

In addition to the improved rate and cycling performance, the aqueous Zn//NaVOH cell also realizes an energy density of 295 Wh kg^{-1} (at a power density of 372 W kg^{-1}) and a power density of 5477 W kg^{-1} (at the energy density of 178 Wh kg^{-1}), which is not only superior than VOH, but also outperform many cathode materials for the aqueous ZIB systems (as illustrated in the Ragone plots in Figure *3*.5g).[144–148] NaVOH with a narrower interlayer spacing achieves a larger specific capacity, higher energy efficiency, longer cycling stability and better rate capability compared to

the pristine VOH, which arise from the low amount of interlayer water, high content of V^{4+} ions and the strong bonding between the interlayer Na^{+} ions and the vanadium oxide network.

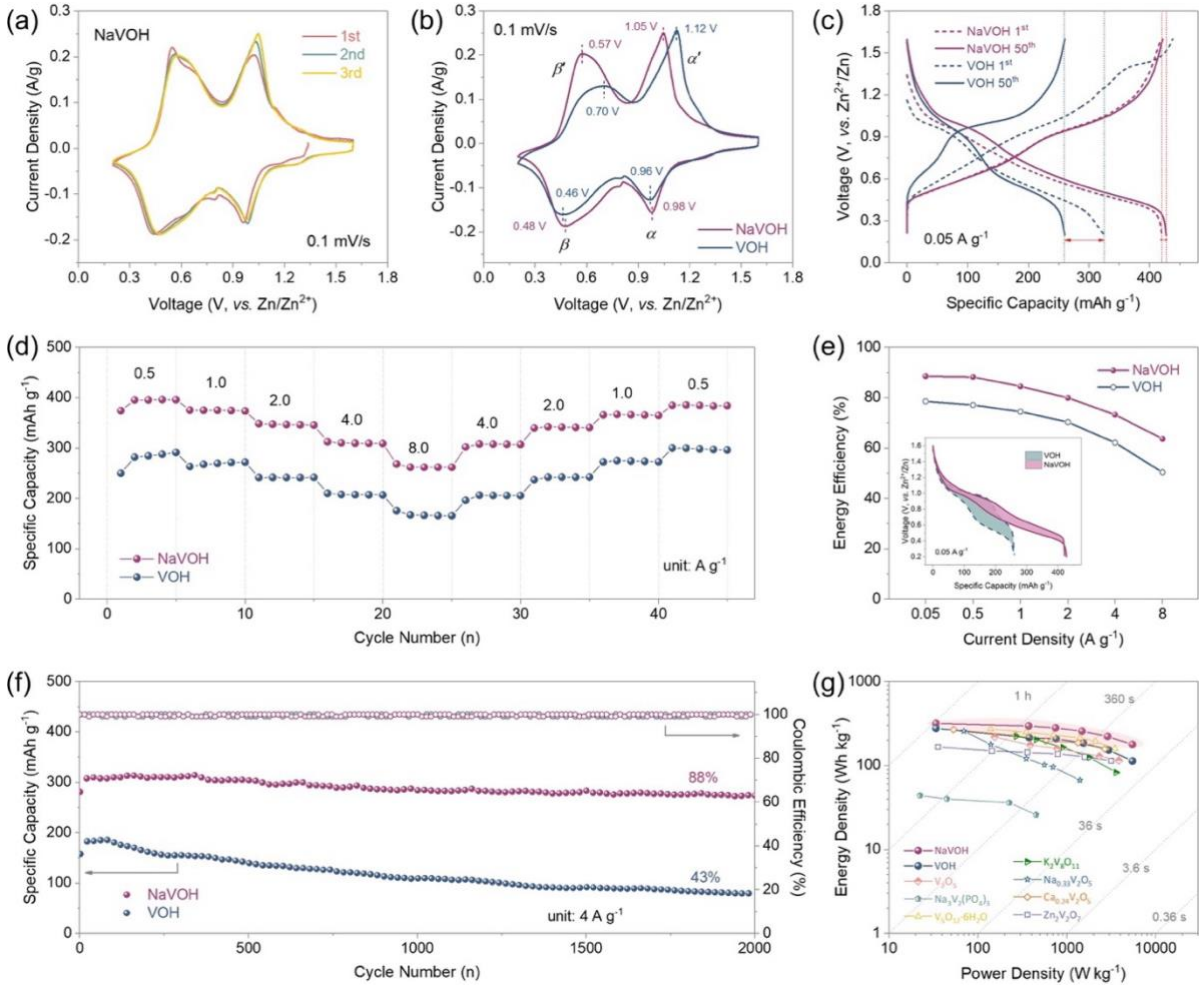

Figure 3.5. Electrochemical characterizations of aqueous Zn//3 M $Zn(CF_3SO_3)_2$//NaVOH and Zn//3 M $Zn(CF_3SO_3)_2$//VOH cells. (a) The initial three cycles of CV curves for NaVOH at a scan rate of 0.1 mV s^{-1}. (b) CV curves of NaVOH and VOH at 0.1 mV s^{-1} (c) The 1st and 50th galvanostatic charge/discharge curves at a current density of 0.05 A g^{-1}. (d) Rate capability. (e) Rate capability evaluated in terms of energy efficiency, insert figure: a comparison of the voltage hysteresis of two samples at 0.05 A g^{-1}, the area enclosed by the charge/discharge profile represents the energy loss. (f) Long-term cycling stability at 4.0 A g^{-1}. (g) Ragone plots of the aqueous Zn//NaVOH and Zn//VOH cells and the aqueous ZIBs with other reported vanadium-based cathode materials. Noted that the energy density values are based on the mass of the active materials in cathode.

3.5 Zn^{2+} Ion Storage Mechanism

The *ex-situ* XRD, XPS, TEM and SEM were carried out to study the structure variation of NaVOH during the Zn^{2+} ion intercalation/deintercalation processes. Figure 3.6a shows the *ex-situ* XRD patterns of NaVOH after the initial discharging and charging. After being discharged to 0.2 V, the (001) peak shifts from the pristine state (8.14°) to a lower degree (6.5°), corresponding to an interlayer expansion from 11.0 Å to 13.7 Å with Zn^{2+} ion insertion. After the subsequent charging to 1.6 V, the (001) peak shifts back to the original position associated with Zn^{2+} extraction. In addition, the (003), (004) and (005) peaks all present the similar shifting process upon cycling, indicating a highly reversible Zn^{2+} intercalation/de-intercalation in NaVOH. Also, it can be observed that the original layered structure of NaVOH is well preserved during cycling, suggesting its good structure stability.

Figure 3.6b is the high resolution XPS spectra of Zn 2p at the discharged/charged states. At the pristine state, there is no Zn^{2+} signal detected. When discharged to 0.2 V, two strong peaks appear at 1022 and 1045 eV, arising from the intercalation of Zn^{2+}. At the fully charged state, though becoming much weaker in intensity, these two Zn peaks can still be detected. This might originate from the surface-adsorbed Zn^{2+} salts on the electrode or the trapped Zn^{2+} ions in the lattice.[115] Figure 3.6c and d present the TEM image with the corresponding elemental mapping of NaVOH at the fully discharged and charged states. The homogeneous distribution of Zn, Na, V and O in the discharged NaVOH confirms the uniform insertion of Zn in the structure. The detection of weaker Zn signal in the charged electrode is consistent with the XPS results (Figure 3.6b). The detection of strong Na signal in both fully discharged and charged state, revealing that the pre-intercalated Na^{+} ions remain stable and inert in the structure upon cycling. The Na:V ratio in the

charged NaVOH is estimated to be 14% from the TEM-EDS results and 13% from SEM-EDS, which does not change much with the pristine state (Na:V ~13.4%). This suggests that the preintercalated Na^+ would not be, or at least not severely, replaced by the cycled Zn^{2+}, which means no deterioration of the vanadium oxide network upon cycling. Though EDS is a surface analytical tool, not very precise tool to quantify the accurate element content, the comparison is still reliable. The Zn:V ratio in the discharged NaVOH is estimated to be 1.2 from SEM-EDS, much higher than that in VOH (Zn:V~0.46). This demonstrates a two times larger amount of Zn^{2+} ions intercalating into NaVOH than VOH, supporting the higher specific capacity of NaVOH (420 mA h g^{-1} at 50 mA g^{-1}) than VOH (324 mA h g^{-1}).

The above results confirm the highly stable and reversible structure of NaVOH upon Zn^{2+} intercalation/deintercalation. During discharging/charging, the original structure of NaVOH is well maintained without obvious Na^+ ion stripping. Compared with VOH, NaVOH has the ability to uptake more Zn^{2+} ions upon discharging; the possible explanations for this are discussed in the GITT results.

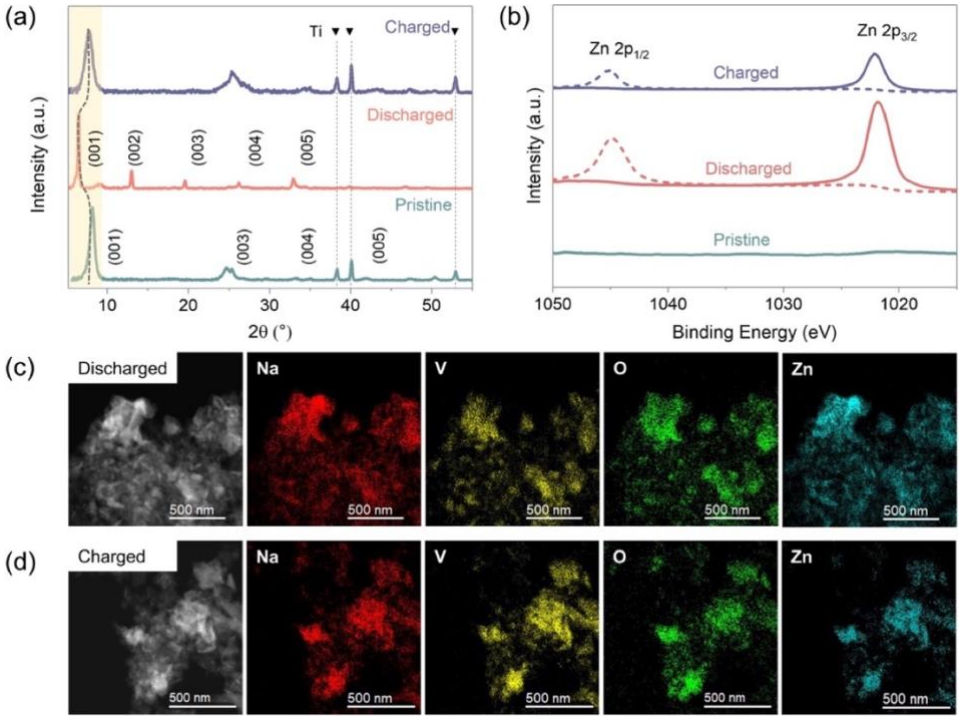

Figure 3.6. (a) *Ex situ* XRD patterns of NaVOH electrodes at the pristine, fully discharged, and charged states (The peaks at 38, 40 and 53° comes from the titanium current collector). (b) The high resolution XPS spectra of Zn 2*p* of NaVOH electrodes at different states. TEM image and the corresponding EDS mappings of NaVOH at (c) the fully discharged state and (d) the fully charged state.

3.6 Electrochemical Kinetics

CV analysis at various scan rates is carried out to explore the electrochemical reaction kinetics. As the scan rate increases from 0.1 to 1.2 mV s^{-1} (Figure *3.7*a and b), the reduction and oxidation peaks shift to a lower and higher voltage, respectively, due to the enlarged polarization. The well-maintained shapes of CV curves with increased scan rates, however, indicate the facile and reversible Zn intercalation/de-intercalation in NaVOH without crystallographic phase change. For both NaVOH and VOH, the *b*-values of all four redox peaks lie in the middle range of 0.5-1.0 (Figure *3.7*c and d), which means that the Zn^{2+} ion storage is achieved by a combination of diffusion and pseudo-capacitive controlled process.

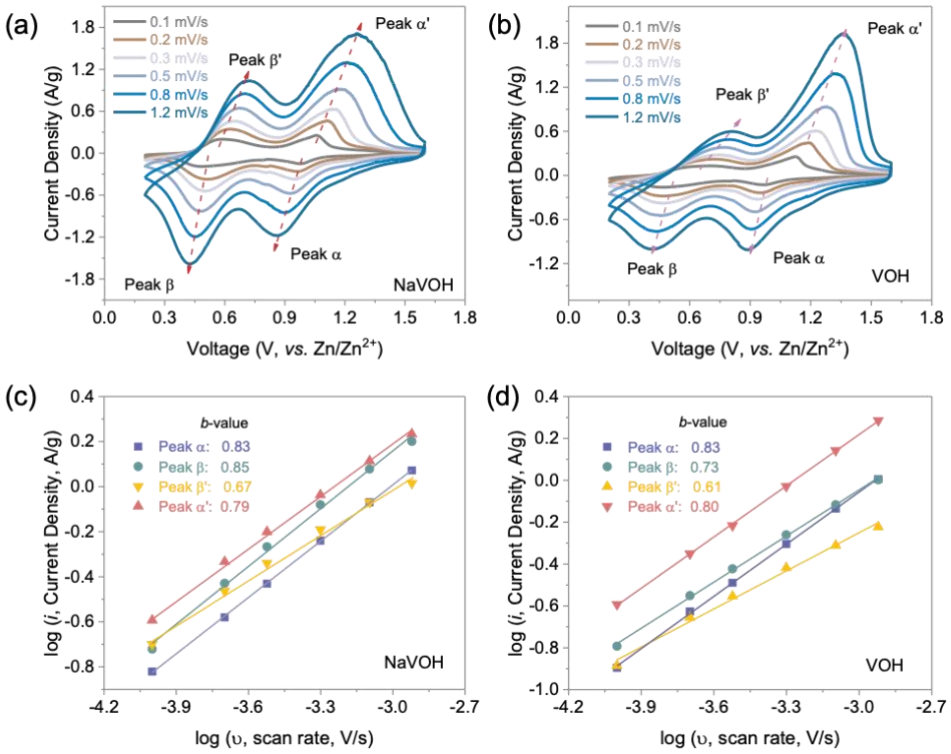

Figure 3.7. (a) and (b) are CV curves at various scan rates for Zn//NaVOH and Zn//VOH, respectively. (c) and (d) are the *b*-values of each redox peak in CV curves of NaVOH and VOH, respectively.

As presented in Figure *3.8*a and b, the charge storage in NaVOH is largely diffusion-controlled; even at high scan rates, diffusion process still accounts for more than 40%. But for VOH, the capacitive contribution occupies the dominant ratio at all scan rates. Another thing to note is, as the scan rate increasing from 0.1 to 1.2 mV s^{-1} (Figure *3.8*b), the calculated diffusion contribution of NaVOH decreases slightly from 58% to 42%. The diffusion contribution of VOH, however, drops significantly from 36% to 14%. The less drop in diffusion contribution of NaVOH explains its better rate performance and suggests its enhanced ion diffusion kinetics.

It needs to be noted that, for electrode materials, the percentage of capacitive contribution makes little sense without revealing the exact capacity. To have a thorough comparison of the reaction

kinetics of NaVOH and VOH, the total capacity, as well as the two types of capacity, is quantified at each scan rate. As shown in Figure *3.8*c, the total stored charge (per unit weight) in NaVOH is much larger than that in VOH (more than 250 C g^{-1} at 0.1 mV s^{-1}), in accordance with the higher specific capacity of NaVOH measured from GCD tests (more than 90 mA h g^{-1} at 0.05 A g^{-1}). Specifically, the capacitive-contributed capacity in NaVOH (494 C g^{-1}) is slightly lower to that in VOH (587 C g^{-1}), while the diffusion-controlled capacity in NaVOH is two times larger than that in VOH at all scan rates. This clearly reveals that the increased capacity of NaVOH is mostly provided by the diffusion-controlled process.

This quantitative analysis demonstrates that NaVOH acquires less charge storage from the capacitive contribution than VOH; but it gets a sharp rise in the diffusion portion, thus enabling the total capacity to actually surpass that of VOH. The highly increased diffusion-contributed capacity of NaVOH suggests its enhanced ionic diffusion kinetics, which will be verified by the GITT results.

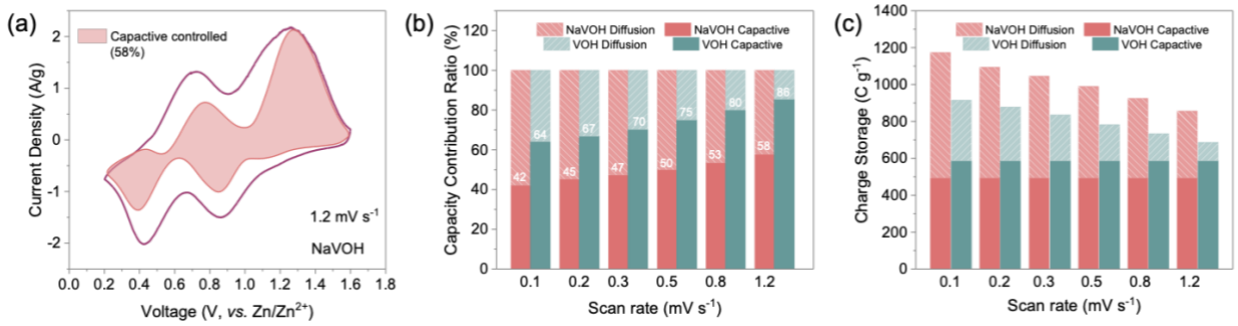

Figure 3.8. (a) Contribution ratio of the capacitive-controlled charge storage in NaVOH at 1.2 mV s^{-1}. (b) The contribution ratios of the capacitive-controlled capacities and diffusion-limited capacities in NaVOH and VOH electrode at different scan rates. (b) The calculated capacitive- and diffusion-contributed capacity in NaVOH and VOH at different scan rates.

The smaller peak separations in CV curves, the better rate performance, a lower polarization and higher energy efficiency of the battery with NaVOH cathode suggest that the Zn^{2+} insertion/extraction in NaVOH is much more kinetically favorable than VOH. Figure *3.9*a shows the Nyquist plots of NaVOH and VOH, both comprising of a depressed semicircle in the high frequency region and a sloped line in the low frequency region (1-0.1 Hz). The diameter of the semicircle corresponds to the charge transfer resistance at the electrode/electrolyte interfaces, while the slope of the straight line is related to the ion diffusion rate in the bulk electrodes.[149] The obtained charge transfer resistance (R_{ct}) and the Zn^{2+} ion diffusion coefficient ($D_{Zn^{2+}}$) of NaVOH and VOH before and after cycling are listed in Table 3.4. Before cycling, the R_{ct} of the ZIB with VOH cathode is calculated to be 91 Ω, much larger than that of NaVOH (35 Ω). This observation agrees with our theoretical calculations that the band gap of VOH is reduced after the pre-intercalation of Na^+ ions. The better electronic conductivity of NaVOH can be ascribed to its higher amount of V^{4+}, which can facilitate the hopping of unpaired electrons between V^{4+}/V^{5+}. After cycling, the R_{ct} values of both samples decrease significantly, due to the gradual penetration of aqueous electrolytes. This is consistent with the capacity raising observed in the initial cycles.

Table 3.4. The charge transfer resistance and Zn^{2+} diffusion coefficient of NaVOH and VOH obtained from EIS.

		Charge Transfer Resistance, R_{ct} (Ω)	Zn^{2+} Diffusion Coefficient, D_{Zn2+} (cm^2/s)
VOH	Pristine	91	1.0×10^{-11}
	After CV	60	5.8×10^{-12}
NaVOH	Pristine	35	8.1×10^{-12}
	After CV	26	2.0×10^{-10}

From the slope of the straight line (in the low frequency region in Figure *3.9*a), we can tell, before cycling, the Zn^{2+} diffusion coefficient of NaVOH is slightly smaller than that of VOH. After cycling, however, D_{Zn}^{2+} of NaVOH becomes much larger than that of VOH. The possible explanations could be, initially, the larger interlayer spacing of pristine VOH contributes to its faster ion diffusion than that of the pristine NaVOH. After cycling, however, some of the intercalated Zn^{2+} ions were trapped in the VOH structure by replacing the interlayer water. As previously stated, partial the interlayer water exist as the acid protons state (H_3O^+) in VOH, those H_3O^+ can be easily replaced by other cations or molecules.[92,95] Upon the first discharging, those H_3O^+ in VOH will be randomly substituted by the intercalated Zn^{2+} ions, hindering the subsequent Zn^{2+} migration.[95] This detrimental phenomenal can be largely avoided in NaVOH because of the stronger chemical bonds between Na^+ and the oxide network.

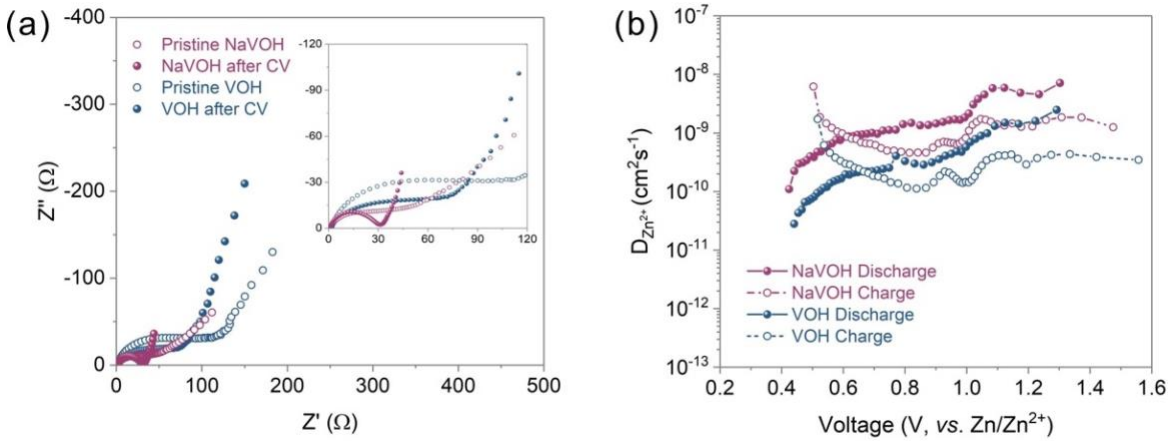

Figure 3.9 (a) Nyquist plots of NaVOH and VOH electrodes collected before and after CV tests. (b) The diffusion coefficient of Zn^{2+} ions upon discharging/charging in the 3rd GITT cycle.

The change of Zn^{2+} diffusion rates upon charging/discharging were analyzed using GITT. As shown in Figure *3.9*b, the calculated D_{Zn}^{2+} for VOH is in the range of 2.8×10^{-11}~2.5×10^{-9} cm^2 s^{-1} upon discharging and 1.1×10^{-10}~1.7×10^{-9} cm^2 s^{-1} upon charging. Even though has a narrower

interlayer distance, NaVOH displays a pretty-competitive diffusion coefficient value (1.1×10^{-10} to 7.1×10^{-9} cm^2 s^{-1} during discharging and 4.6×10^{-10} to 6.2×10^{-9} cm^2 s^{-1} during charging), superior to VOH. This is quite different from the previous consensus that a larger interlayer spacing always leads to a faster ion diffusion, the possible explanations will be discussed later.

Another observation is that D_{Zn}^{2+} during charging (deintercalation) is lower than that during discharging (intercalation), for both NaVOH and VOH. This is because the extraction of Zn^{2+} ions is more difficult than insertion due to the electrostatic interactions between the cycled ions and the host, responsible for the voltage polarization. If we compare this D_{Zn}^{2+} difference between discharge and charge processes for the two materials (Table 3.5), it is obvious that this difference is smaller for NaVOH than VOH, explaining the smaller voltage polarization of NaVOH observed in the CV and GCD curves.

When comparing the diffusion rate change upon cycling, we can see the average D_{Zn}^{2+} of NaVOH remains highly stable; for the discharging process, there is even a 13% increase from the 1st to the 3rd cycle. The average D_{Zn}^{2+} of VOH, however, decreases 39% for the discharge process and 15% for the charge process during the first three cycles, indicating a rapid decay of ion diffusion kinetics in VOH upon cycling. Based on the above description, clearly, NaVOH displays a faster Zn^{2+} ion transportation, a smaller diffusion rate difference between charging and discharging, as well as a lower diffusion rate fluctuation upon cycling. This explains the better rate performance, smaller polarization, and slower capacity fading of NaVOH.

Table 3.5. The average Zn^{2+} diffusion coefficient for NaVOH and VOH in the first three GITT cycles.

		Zn^{2+} Diffusion Coefficient (D_{Zn2+}, $cm^2\ s^{-1}$)		
		1st	2nd	3rd
VOH	Discharge	7.2×10^{-10}	5.0×10^{-10}	4.4×10^{-10}
	Charge	3.4×10^{-10}	3.2×10^{-10}	2.9×10^{-10}
NaVOH	Discharge	1.5×10^{-9}	1.8×10^{-9}	1.7×10^{-9}
	Charge	1.4×10^{-9}	1.3×10^{-9}	1.2×10^{-9}

In summary, the intercalation of Na^+ ions and its replacement of some interlayer water in VOH generate very intricate influences on the electrochemical reaction kinetics. On one hand, due to the removal of partial structural water, the interlayer space of NaVOH shrunk, which seems to be a hindrance factor for the charge carrier diffusion. Actually, although there is a ~1 Å decrease (NaVOH: 11.0 Å, VOH: 12.0 Å), the interplanar distance of NaVOH is still more than two times larger than the radius of hydrated Zn^{2+} ions (4.3 Å),[150] wide enough for its quick transportation. In this case, when comparing the reaction kinetics of NaVOH and VOH, the role of interlayer distance is not as significant as the other limiting factors, like the structural variation during ion insertion/extraction or the electrostatic interactions between charge carriers and the host. For NaVOH, as discussed before, the pre-intercalated Na^+ ions form strong ionic bonds with the V-O network and remain stable in the structure upon cycling, which could help preventing the kinetics decline caused by the structure distortion. As a result, NaVOH provides the unimpeded ion diffusion channels and enables a larger amount of Zn^{2+} to diffuse deep into the inner structure without being blocked, thus exhibiting not only the promoted reaction kinetics but also a higher capacity than VOH. As for VOH, on the contrary, some of its interlayer water (H_3O^+) can be easily replaced by the inserted Zn^{2+} upon the initial discharging. The exchange of coordinated water with Zn^{2+} can occur randomly along the diffusion pathways, which not only deteriorates the V-O

skeleton but also limits the migration depth of Zn^{2+} ions. So, both the cycling performance and reaction kinetics of VOH decay severely, while those of NaVOH remain highly stable.

3.7 CONCLUSIONS

By pre-intercalating Na^+ ions into the oxide structure, about 0.3 interlayer water per V_2O_5 will be favorably replaced, leading to a decreased interlayer spacing from 12.0 Å (VOH) to 11.0 Å (NaVOH). Though has a narrower interlayer spacing, NaVOH demonstrates a faster Zn^{2+} diffusion rate, a larger specific capacity (420 mA h g^{-1} at 0.05 A g^{-1}), an improved energy efficiency (88% at 0.05 A g^{-1}) with a higher Zn^{2+} intercalation/de-intercalation reversibility, and a significantly improved electrochemical stability (88% capacity retention after 2000 cycles). These observations contradict many previous works that pre-intercalation foreign species will always expand the lattice spacing, and the bigger interlayer distance accounts for the improved electrochemical reversibility and stability.

The understandings about how Na^+ pre-intercalation affect the crystal structure and the electrochemical performance are: First, Na^+ ions can be pre-intercalated into VOH via replacing partial interlayer water, resulting in a decreased basal distance, a reduced structural water content, and an increased V^{4+} amount. Second, the introduction of more V^{4+} can facilitate the hopping of electrons between V^{4+} and V^{5+}, hence enhancing the electronic conductivity. Third, the replacement of partial interlayer water by Na^+ ions could alleviate the interactions between cycled Zn^{2+} ions and the host, which ensures a faster and more reversible Zn^{2+} ion insertion/extraction without server structural distortion. As for VOH, its structural water (those exist in the form of H_3O^+) can be readily and randomly replaced by Zn^{2+} ions upon discharging, blocking the pathways for the subsequent Zn^{2+} migration. So, both the cycling performance and kinetics properties of VOH decay severely upon cycling.

Chapter 4. Effects of Different Pre-intercalated Metal Cations

4.1 Background and Approach

In Chapter 3, we have explored the pre-intercalation of Na^+ ions into the $V_2O_5{\cdot}nH_2O$ phase, highlighting their role in boosting structural stabilities and energy storage capabilities. However, there is still a gap in our understanding regarding the intricate relationships between these pre-introduced species and their ion stabilization effects.

In this study, a series of metal cations, including singly charged (Na^+, K^+, and Rb^+), doubly charged (Mg^{2+}), and triply charged cations (Al^{3+}), were pre-intercalated into the $V_2O_5{\cdot}nH_2O$ phase using the same hydrothermal approach. We then investigated how these diverse cations influence the morphology and structure of δ-$M_xV_2O_5{\cdot}nH_2O$ (M = Na, K, Rb, Mg, Al). By evaluating the performance of these δ-$M_xV_2O_5{\cdot}nH_2O$ materials in aqueous ZIBs, we aim to understand the impacts of cation size and electronegativity on electrochemical performance metrics, such as specific capacity, electronic conductivity, and ion diffusion rate. Through this exploration, we hope to establish a comprehensive understanding of how the properties of pre-intercalated metal cations interact with the crystal structure of $V_2O_5{\cdot}nH_2O$, focusing particularly on aspects like interlayer spacing, structural water content, and the presence of V^{4+}, and ultimately elucidate the correlations between these factors and their collective impacts on the electrochemical performance of the material.

4.2 Materials Characterization

Figure 4.1 shows SEM images of the synthesized δ-$M_xV_2O_5{\cdot}nH_2O$ (M = Na, K, Rb, Mg, Al) materials. Morphologies of the five δ-$M_xV_2O_5{\cdot}nH_2O$ materials vary with the pre-intercalated cations. NaVOH exhibits a compact, platelets-like structure, with a diameter of approximately 6μm, constructed from thick V–O sheets. KVOH displays a porous, 3-D flower-like structure, comprising thin nanosheets and nanofibers. RbVOH, in comparison with KVOH, exhibits a more compact, spherical clusters, composed

of smaller nanofibers. AlVOH features a more spherical and symmetric urchin morphology with a diameter of ~10 μm. The structure consists of uniform sized, thin, nanobelts. Similarly, MgVOH shows a spherical structure built from nanobelts, although its diameter is larger than that of AlVOH, and its nanobelts are wider. Among all the five samples, AlVOH exhibits the most uniform and symmetric structure. Compared with the singly charged alkali cations (Na^+, K^+, and Rb^+), the doubly charged Mg^{2+} and triply charged Al^{3+} form bigger structures.

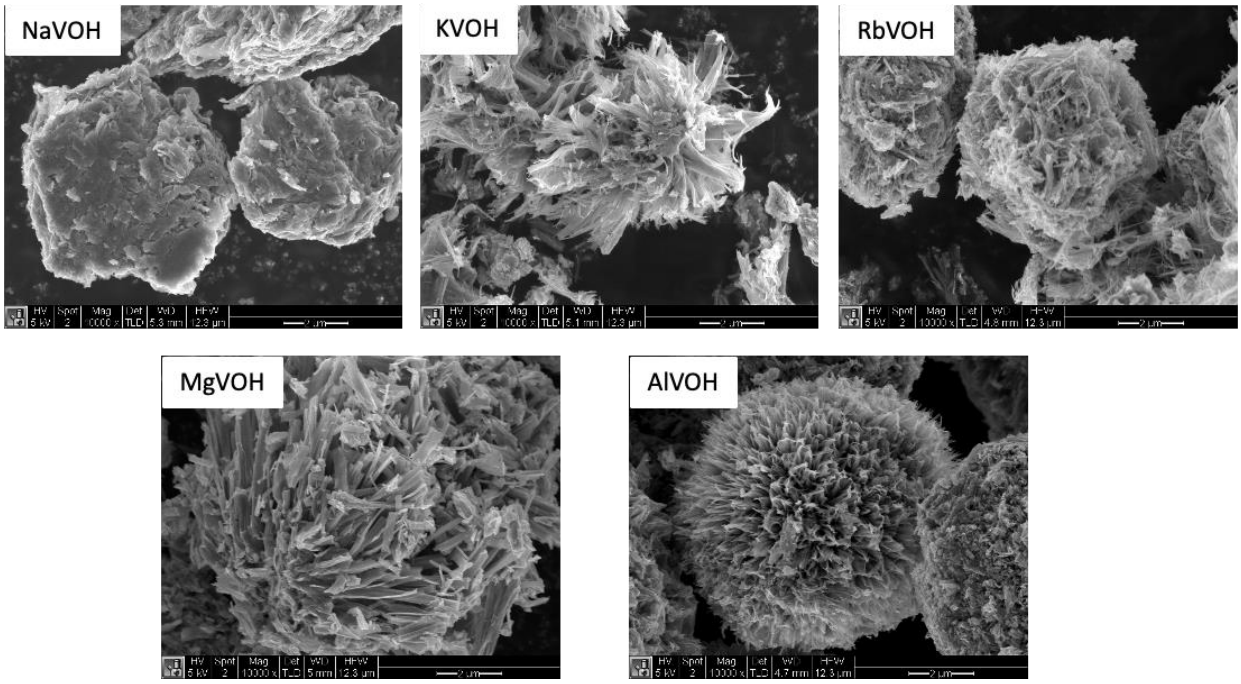

Figure 4.1. SEM images of the five δ-$M_xV_2O_5{\cdot}nH_2O$ (M = Na, K, Rb, Mg, Al) powders.

The EDS elemental mapping of the five samples (Figure 4.2) reveal the uniform distribution of Na, K, Rb, Mg, and Al in their respective samples, confirming the successful pre-intercalation of the five metal ions. The absence of the S peak in all spectra (Figure 4.2) confirms that only metal cations are intercalated into the δ-$V_2O_5{\cdot}nH_2O$ structure, with the sulfate anions completely removed upon washing. The M:V ratios in δ-$M_xV_2O_5{\cdot}nH_2O$ (M = Na, K, Rb, Mg, Al) materials, determined via SEM-EDS, are 18%, 16%, 19%, 10%, and 8%, respectively. This corresponds to a composition of δ-$Na_{0.36}V_2O_5{\cdot}nH_2O$, δ-$K_{0.32}V_2O_5{\cdot}nH_2O$, δ-$Rb_{0.38}V_2O_5{\cdot}nH_2O$, δ-$Mg_{0.21}V_2O_5{\cdot}nH_2O$, and δ-$Al_{0.16}V_2O_5{\cdot}nH_2O$, respectively. The contents of pre-inserted metal cations are roughly in line with literature data indicating that there is

approximately 0.3 H_3O^+ per V_2O_5 that can be exchanged with foreign ions, and the exchange capacity of $V_2O_5 \cdot nH_2O$ with respect to the monovalent, divalent, and trivalent metal cations is about 0.3, 0.16, and 0.11, respectively.[92,95]

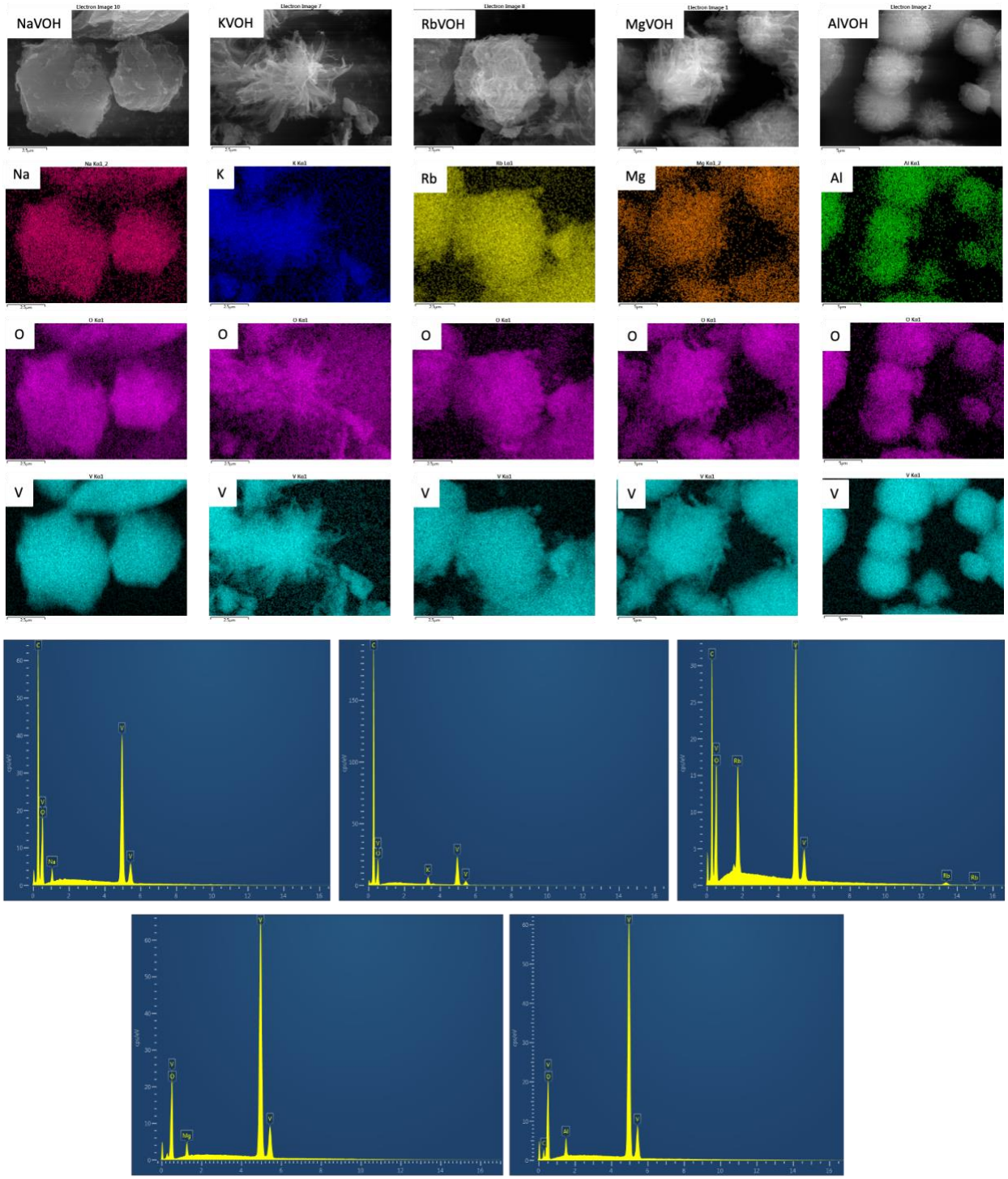

Figure 4.2. EDS elemental mappings and spectra of δ-$M_xV_2O_5 \cdot nH_2O$ (M = Na, K, Rb, Mg, Al).

Figure 4.3a presents the XRD patterns of the five samples. It is evident that all δ-$M_xV_2O_5{\cdot}nH_2O$ (M = Na, K, Rb, Mg, Al) exhibit characteristic (00*l*) diffraction peaks, consistent with the bilayered δ-$V_2O_5{\cdot}nH_2O$ structure. The interlayer distance, calculated from the position of the (001) peak, is found to be influenced by both the charge and the radius of pre-intercalated metal cations. Specifically, RbVOH displays the smallest interlayer distance of 10.5 Å, whereas AlVOH exhibits the largest interlayer distance of 13.5 Å.

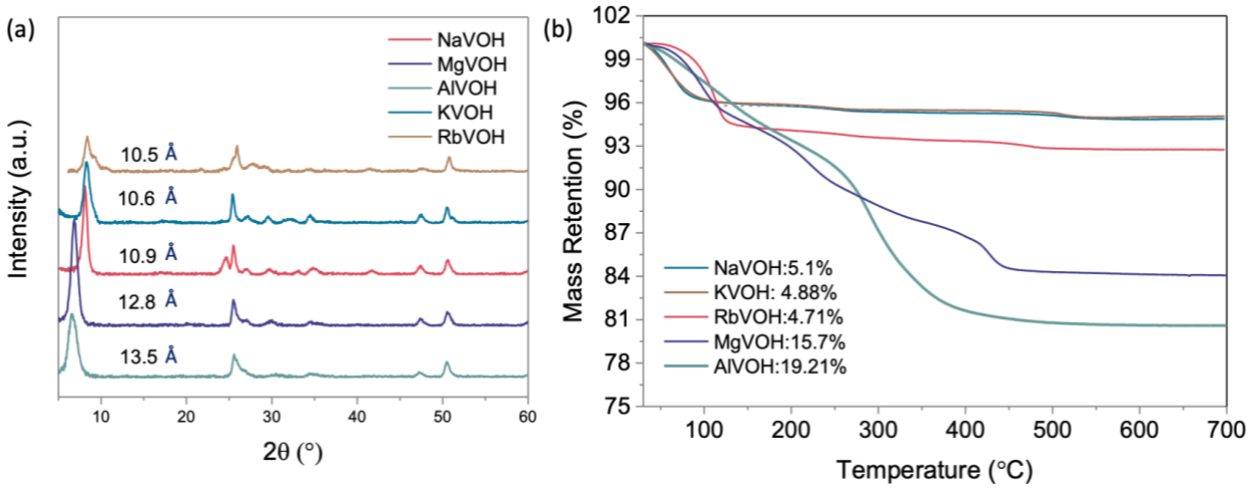

Figure 4.3. (a) XRD patterns, and (b) TGA results of δ-$M_xV_2O_5{\cdot}nH_2O$ samples.

Table *4.1* compares the structural and composition data of δ-$M_xV_2O_5{\cdot}nH_2O$ (M = Na, K, Rb, Mg, Al). It is evident that the interlayer spacing of $M_xV_2O_5{\cdot}nH_2O$ can be directly correlated with both the hydrated radius (not the ionic radii) and the electronegativity of pre-inserted metal cations. A larger hydrated ion radius leads to a bigger interlayer spacing of δ-$M_xV_2O_5{\cdot}nH_2O$, suggesting that all the preintercalated metal ions are coordinated by water molecules within the interlayer of $V_2O_5{\cdot}nH_2O$. Additionally, a smaller electronegativity of M cation leads to a smaller interlayer spacing due to a stronger electrostatic attraction between M cations and O anions, pulling adjacent V–O layers closer.

Interlayer water content in the five samples was evaluated from TGA results (Figure 4.3b). By calculating the weight loss in the temperature range of 100-500 °C, the hydration number in each sample is determined to be

δ-$Na_{0.36}V_2O_5{\cdot}0.54H_2O$, δ-$K_{0.32}V_2O_5{\cdot}0.52H_2O$, δ-$Rb_{0.38}V_2O_5{\cdot}0.50H_2O$, δ-$Mg_{0.21}V_2O_5{\cdot}1.87H_2O$, and δ-$Al_{0.16}V_2O_5{\cdot}2.39H_2O$, respectively (listed in Table *4.1*).

Table 4.1. Correlations between properties of pre-intercalated metal cations (size, hydrated ion radius, electronegativity) and the structure and composition of δ-$M_xV_2O_5{\cdot}nH_2O$ materials.

Preintercalated M cation	Al	Mg	Na	K	Rb
Charge number	3+	2+	1+	1+	1+
Ionic Radius (Å) [150–152]	0.53	0.65	0.95	1.33	1.47
Hydrated ion Radius (Å) [150–152]	4.80	4.40	3.58	3.31	3.05
Interplanar Spacing (Å)	13.5	12.8	10.9	10.6	10.5
Electronegativity of Element (Pauling scale)	1.61	1.31	0.93	0.82	0.82
Electronegativity Difference (with O: 3.44)	1.83	2.13	2.51	2.62	2.62
x in $M_xV_2O_5{\cdot}nH_2O$	0.16	0.21	0.36	0.32	0.38
Amount of water (*n*)	2.39	1.87	0.54	0.52	0.50
$V^{4+}/(V^{4+}+V^{5+})$	6.0%	7.2%	11.6%	9.6%	9.1%

Figure 4.4a shows the XPS survey spectra of the five δ-$M_xV_2O_5{\cdot}nH_2O$ (M = Na, K, Rb, Mg, Al) samples. The high-resolution XPS spectra were collected for the Mg 1*s* region of MgVOH (Figure 4.4b), Al 2*s* region of AlVOH (Figure 4.4c), Na 1*s* region of NaVOH (Figure 4.4d), K 2*p* region of KVOH (Figure 4.4e), and Rb 3*d* region of RbVOH (Figure 4.4f). The single peak observed at 1304.8 eV in Figure 4.4b, 120 eV in Figure 4.4c, and 1071.8 eV in Figure 4.4d corresponds to the 1*s* of Mg^{2+}, 2*s* of Al^{3+}, and 1*s* of Na^+, respectively. In Figure 4.4e, the two peaks located at 292.9 and 295.7 eV are attributed to the clearly spaced spin-orbit K $2p_{3/2}$ and K $2p_{1/2}$ components (Δ chloride = 2.8 eV). The two peaks at 111.2 and 109.7 eV in Figure 4.4f are identified as the $3d_{3/2}$ and $3d_{5/2}$ of Rb elements in RbVOH. These XPS results strongly confirm

the successfully pre-intercalation of metal cations (Na^+, K^+, Rb^+, Mg^{2+}, and Al^{3+}) into the corresponding δ-$M_xV_2O_5{\cdot}nH_2O$ (M = Na, K, Rb, Mg, Al) materials.

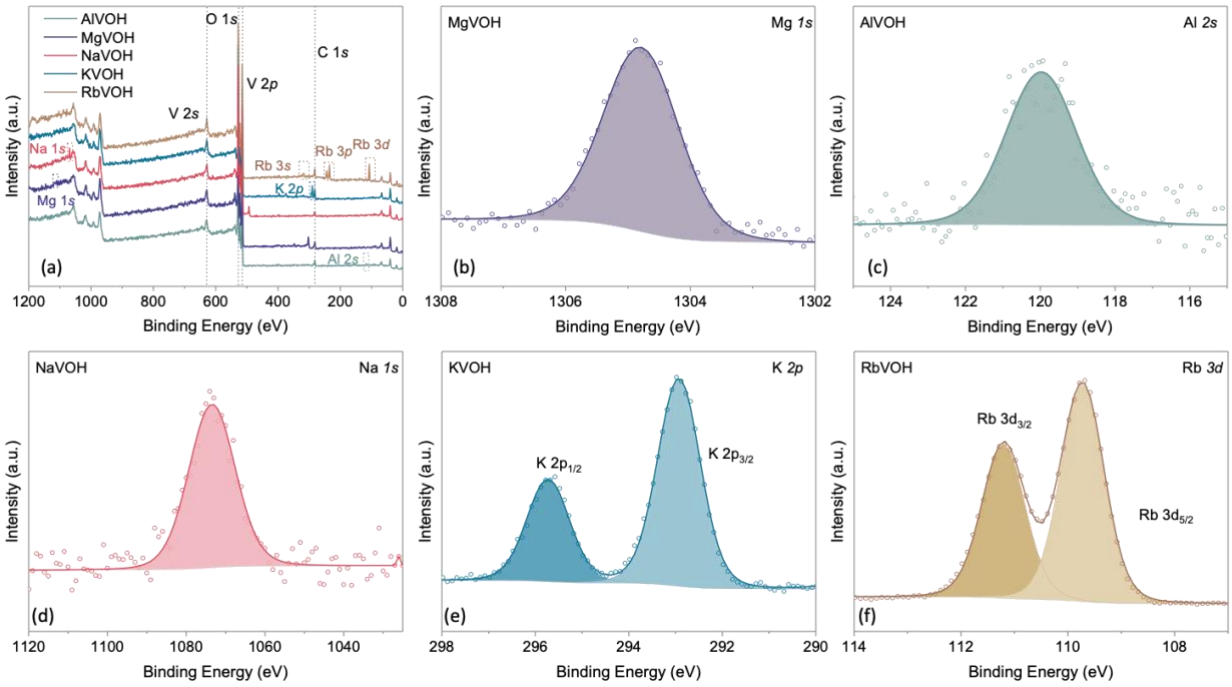

Figure 4.4. (a) XPS survey spectra of δ-$M_xV_2O_5{\cdot}nH_2O$ materials. High-resolution XPS spectra of (b) Mg 1*s* region of MgVOH, (c) Al 2*s* region of AlVOH, (d) Na 1*s* region of NaVOH, (e) K 2*p* region of KVOH, and (f) Rb 3*d* region of RbVOH.

Figure 4.5 displays the high-resolution V 2*p* and O 1*s* spectrum of five metal ion pre-intercalated vanadium oxides. The V 2*p* spectra indicate that all five samples exhibit mixed valence states of V^{5+} and V^{4+}. The corresponding binding energy and ratio of V^{5+} and V^{4+} components in each sample are listed in Table 4.2 and Table *4.1*, respectively. The ratio of $V^{4+}/(V^{4+}+V^{5+})$ is calculated to be 6.0% (AlVOH), 7.2% (MgVOH), 11.6% (NaVOH), 9.6% (KVOH), and 9.1% (RbVOH), respectively. From Table *4.1*, if we only compare the monovalent cations (Na^+, K^+, and Rb^+), the V^{4+} ratio follows the sequence of Rb < K < Na, consistent with the sequence of hydrated ion radius (Rb < K < Na). However, when comparing cations with different charges (Na^+, Mg^{2+}, and Al^{3+}), the V^{4+} ratio follows the sequence of Al < Mg < Na, contrary to the sequence of hydrated ion radius (Al > Mg > Na).

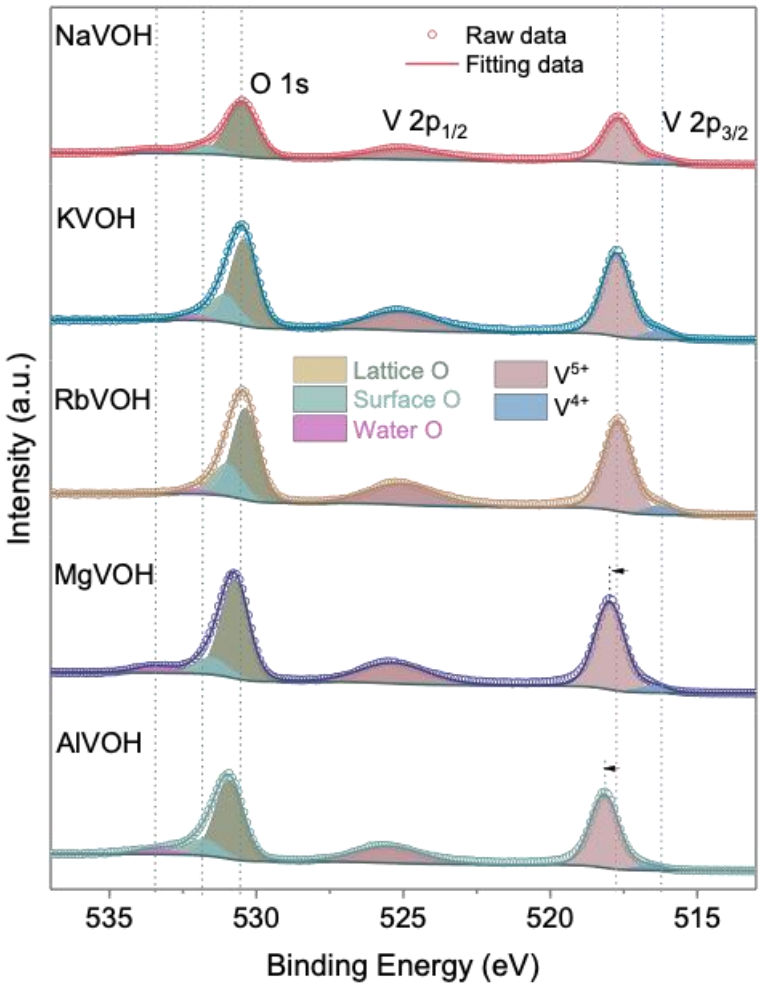

Figure 4.5. High-resolution XPS spectra of V 2*p* and O 1*s* region for δ-$M_xV_2O_5{\cdot}nH_2O$.

Another observation from the V 2*p* spectra is that, for the monovalent cations (NaVOH, KVOH, and RbVOH), the binding energy of their V $2p_{3/2}$ peaks show neglectable differences (Table 4.2). However, for cations with different charges (NaVOH, MgVOH, and AlVOH), both V^{4+} and V^{5+} peaks shift noticeably. For example, the binding energy of V^{5+} changes from 517.7 eV (NaVOH) to 518.0 eV (MgVOH), and to 518.2 eV (AlVOH). This shift of V 2*p* peaks may stem from the formation of M–O bonds in δ-$M_xV_2O_5{\cdot}nH_2O$. A stronger Al–O bond and Mg–O bond (than Na–O bond) induce a larger shift of V peaks in AlVOH and MgVOH.

Regarding the O 1s region (Figure 4.5), the spectrum of NaVOH shows three well-defined peaks at 530.5, 531.7, and 533.5 eV, corresponding to distinct oxygen-containing species: lattice oxygen coordinated

with vanadium atoms (O–V), surface oxygen (e.g., V-bonded hydroxyl groups, V–O–H), and the structural water, respectivly.[153] Similar phenomena are also observed for the other four δ-$M_xV_2O_5{\cdot}nH_2O$ materials. From the XPS spectral area, the percentage area of structural water in the five samples follows the order: AlVOH (5.5%) > MgVOH (5.2%) > NaVOH (4.9%) > KVOH (3.3%) > RbVOH (3.0%). This agrees with the sequence of water content measured from TGA results (Table *4.1*).

Table 4.2. Binding energy of V 2$p_{3/2}$ and O 1*s* peaks of δ-$M_xV_2O_5{\cdot}nH_2O$ samples.

	Binding Energy (eV)				
	V^{4+}	V^{5+}	Lattice O	Surface O	Water O
NaVOH	516.3	517.7	530.5	531.7	533.5
KVOH	516.3	517.8	530.4	531.1	532.2
RbVOH	516.3	517.7	530.4	531.0	532.0
MgVOH	516.5	518.0	530.7	531.5	533.4
AlVOH	516.7	518.2	530.9	531.8	533.4

Figure 4.6 shows the FTIR spectra of δ-$M_xV_2O_5{\cdot}nH_2O$ (M = Na, K, Rb, Mg, Al) phases, with the corresponding frequencies and assignments of FTIR bands listed in Table *4.3*. The broad peak at 745 cm^{-1} in NaVOH is relate to the asymmetric V–O–V stretching vibrations. This band shifts to a higher wavenumber in KVOH and RbVOH, suggesting a shorter V–O–V bond length for the KVOH and RbVOH phases. Bands between 972 cm^{-1} to 1009 cm^{-1} arise from the stretching vibration of the terminal oxygen (V=O bond). The bands at ~1600 cm^{-1} and at ~3600 cm^{-1} corresponds to the H–O–H bending and the O–H stretching of the interlayer water molecules, which are clearly present in all five samples.

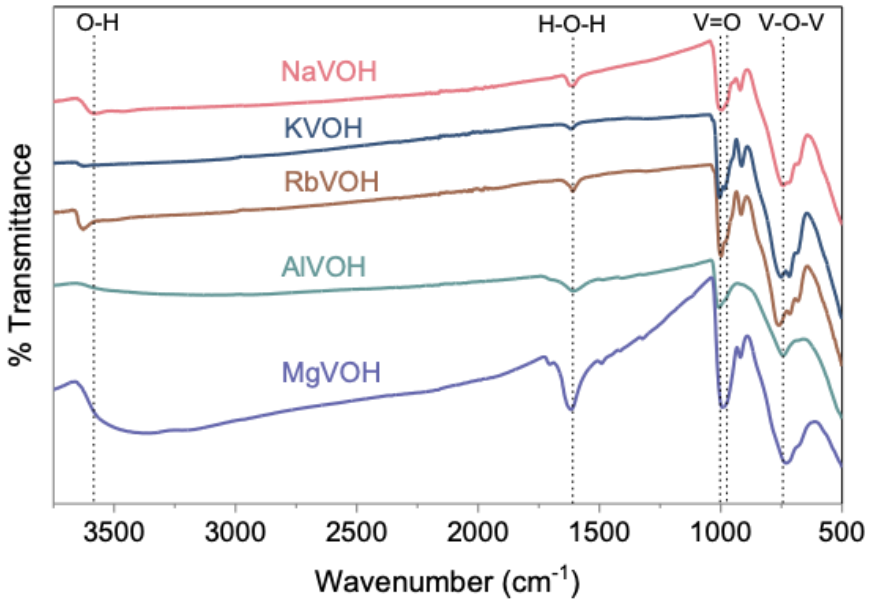

Figure 4.6. FTIR spectra of the δ-$M_xV_2O_5{\cdot}nH_2O$ phases (M = Na, K, Rb, Mg, Al).

Table 4.3. FTIR peak positions and their assignments in δ-$M_xV_2O_5{\cdot}nH_2O$ samples.

Wavenumber /cm^{-1}					Assignments
NaVOH	KVOH	RbVOH	MgVOH	AlVOH	
745	751	761	732	743	Asymmetric stretching of V–O–V
972	984	979	996	1009	Stretching of V=O
997	1005	999			
1607	1610	1609	1617	1604	H–O–H bending of water molecules
3593	3627	3631	3562	3593	O–H stretching of water molecules

4.3 Electrochemical Performances

The electrochemical performances of δ-$M_xV_2O_5{\cdot}nH_2O$ materials were evaluated in ZIBs. From the GCD curves at a current density of 4 A g^{-1} (Figure 4.7), all samples exhibit a similar shape to that of δ-$V_2O_5{\cdot}nH_2O$. The two plateaus at ~1.0 V and 0.5 V can be attributed to the redox reactions between V^{5+}/V^{4+} and V^{4+}/V^{3+} pairs, indicating a two-step Zn^{2+} intercalation/de-intercalation process. Their initial

discharge capacities follow the order: KVOH (333 mA h g^{-1}) > NaVOH (281 mA h g^{-1}) > RbVOH (253 mA h g^{-1}) ≈ MgVOH (251 mA h g^{-1}) > AlVOH (214 mA h g^{-1}). Interestingly, KVOH, with the second smallest interlayer distance (10.6 Å), delivers the highest capacity (333 mA h g^{-1}). While AlVOH, with the biggest interlayer distance (13.5 Å), delivers the lowest capacity (214 mA h g^{-1}). These results suggest that interlayer spacing is not a determining factor for charge storage capabilities of δ-$M_xV_2O_5{\cdot}nH_2O$ phases. This contradicts the previous consensus that pre-intercalated foreign ions expand the interlayer distance, enabling more open diffusion pathways and sites for the cycled ions, thereby contributing to a higher capacity. All five samples show a gradual increase in capacity in the initial cycles. After the initial activation, the capacity of the five samples reaches to a maximum in the same order: KVOH (351 mA h g^{-1}) > NaVOH (315 mA h g^{-1}) > RbVOH (280 mA h g^{-1}) > MgVOH (272 mA h g^{-1}) > AlVOH (248 mA h g^{-1}).

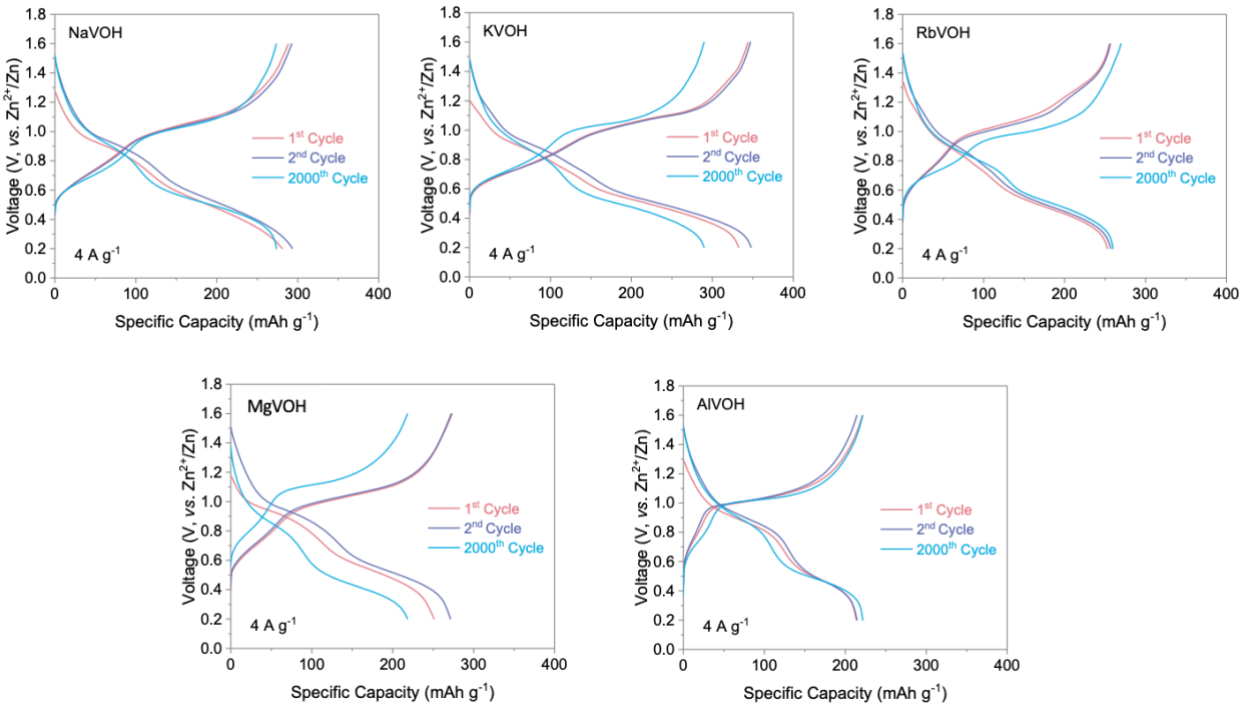

Figure 4.7. The 1st, 2nd, and 2000th cycle of GCD curves for the ZIBs with the δ-$M_xV_2O_5{\cdot}nH_2O$ cathodes (M = Na, K, Rb, Mg, Al) at 4A g^{-1}.

Cycling stability of the five samples is shown in Figure 4.8a and summarized in Table 4.4. After 2000 cycles, it is still the KVOH that maintains the highest capacity of 290 mA h g^{-1}. The capacity retention rates for the five samples follows the trend: RbVOH (93%) > AlVOH (90%) > NaVOH (87%) > KVOH (83%) > MgVOH (80%). Notably, RbVOH, with the smallest interlayer distance, exhibits the highest capacity retention of 93% (to the highest capacity). Surprisingly, there are no clear correlations between the cycling stability of $M_xV_2O_5{\cdot}nH_2O$ and factors such as ionic radius, electronegativity, or the interlayer distance of the materials.

Table 4.4. Comparison of specific capacity and cycling stability of δ-$M_xV_2O_5{\cdot}nH_2O$ at 4 A g^{-1}.

Sample	Initial capacity	Highest capacity	Capacity at 2000th cycle	Capacity retention of the 2000th cycle
NaVOH	281 mA h g^{-1}	315 mA h g^{-1}	274 mA h g^{-1}	87%
KVOH	333 mA h g^{-1}	351 mA h g^{-1}	290 mA h g^{-1}	83%
RbVOH	253 mA h g^{-1}	280 mA h g^{-1}	260 mA h g^{-1}	93%
MgVOH	251 mA h g^{-1}	272 mA h g^{-1}	218 mA h g^{-1}	80%
AlVOH	214 mA h g^{-1}	248 mA h g^{-1}	222 mA h g^{-1}	90%

Upon increasing the current density from 0.5 to 8 A g^{-1}, KVOH continues to demonstrate the highest capacity of 304 mA h g^{-1}, corresponding to a retention of 73% compared to that at 0.5 A g^{-1}, outperforming the other samples (Figure 4.8b). The capacity retention rates for the five samples are (summarized in Table 4.5): KVOH (73%) > RbVOH (61%) ≥ NaVOH (61%) > AlVOH (59%) > MgVOH (58%). Interestingly to note, while the singly charged Na-, K-, Rb-VOH samples have smaller interlayer distances than the doubly-and triply-charged species, their rate capabilities are slightly better. This suggests that the interlayer distance might not be a key factor determining ion diffusion kinetics, as all δ-$M_xV_2O_5{\cdot}nH_2O$ materials possess sufficiently large interlayer spacing (> 9 Å), more than twice the radius of hydrated Zn^{2+} ions (4.3 Å).[150] The doubly and triply charged ions in δ-$M_xV_2O_5{\cdot}nH_2O$ likely exert higher electrostatic interactions with the cycled Zn^{2+} ions, leading to a poorer rate performance.

Table 4.5. Comparison of the specific capacity and rate performance of δ-$M_xV_2O_5{\cdot}nH_2O$ at 0.5, 1.0, 2.0, 4.0, and 8.0 A g^{-1}.

Sample	Discharge capacity					Capacity retention at 8 A g^{-1}
	0.5 A g^{-1}	1 A g^{-1}	2 A g^{-1}	4 A g^{-1}	8 A g^{-1}	
NaVOH	391 mA h g^{-1}	368 mA h g^{-1}	338 mA h g^{-1}	298 mA h g^{-1}	240 mA h g^{-1}	61%
KVOH	417 mA h g^{-1}	401 mA h g^{-1}	379 mA h g^{-1}	349 mA h g^{-1}	304 mA h g^{-1}	73%
RbVOH	354 mA h g^{-1}	339 mA h g^{-1}	310 mA h g^{-1}	263 mA h g^{-1}	216 mA h g^{-1}	61%
MgVOH	348 mA h g^{-1}	312 mA h g^{-1}	285 mA h g^{-1}	245 mA h g^{-1}	201 mA h g^{-1}	58%
AlVOH	301 mA h g^{-1}	279 mA h g^{-1}	252 mA h g^{-1}	216 mA h g^{-1}	177 mA h g^{-1}	59%

Overall, the specific capacity, cyclability, and rate capability of δ-$M_xV_2O_5{\cdot}nH_2O$ samples (M = Na, K, Rb, Mg, Al) are not solely determined by a single factor, such as interlayer spacing or the size and charge of the pre-intercalated ions.

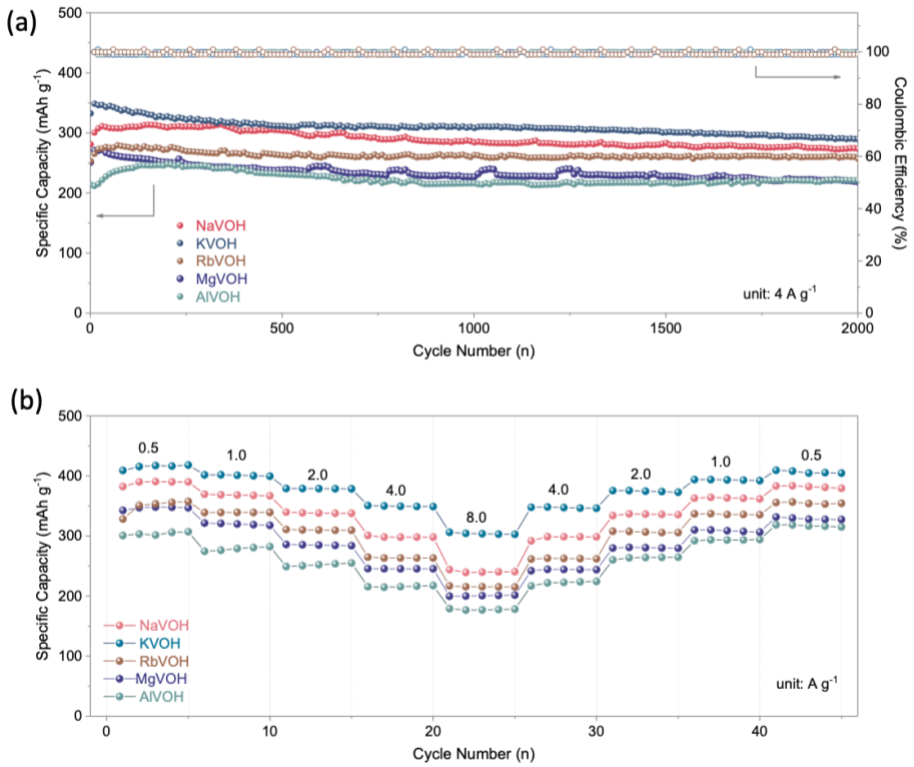

Figure 4.8. (a) Cycling stability at 4A g^{-1}, and (b) Rate capability of ZIBs with the δ-$M_xV_2O_5{\cdot}nH_2O$ cathode.

The CV curves of the five samples at a scan rate of 0.1 mV s^{-1} are depicted in Figure 4.9, and their corresponding redox peaks are listed in Table 4.6. Notably, CV curves of all five samples exhibit similar redox peaks, suggesting a comparable zinc ion storage mechanism. Two pairs of well-defined redox peaks are observed, corresponding to the redox reactions between V^{5+}/V^{4+} pairs (at around 1 V) and V^{4+}/V^{3+} pairs (at around 0.5 V), indicating a two-stage Zn^{2+} intercalation/deintercalation process in the δ-$M_xV_2O_5{\cdot}nH_2O$ materials. The enclosed area in the CV curves represents the charge storage. In comparison, KVOH demonstrates the largest CV area, while AlVOH exhibits the smallest, consistent with their specific capacities obtained from the GCD tests (Table 4.5).

For all five samples, their initial three CV curves are well overlapped, implying highly reversible Zn^{2+} ion intercalation/deintercalation processes. The redox peaks in the CV curves align well with the voltage plateaus in the GCD curves in Figure 4.7. The peak separation between each redox pairs indicates the voltage polarization. From Table 4.6, KVOH exhibits the narrowest peak separation, while MgVOH shows the largest. Interestingly, the peak separation of the five samples follows the same tread as their rate performance, suggesting that their Zn^{2+} ion storage kinetics adhere to the order: KVOH > RbVOH ≥ NaVOH > AlVOH > MgVOH.

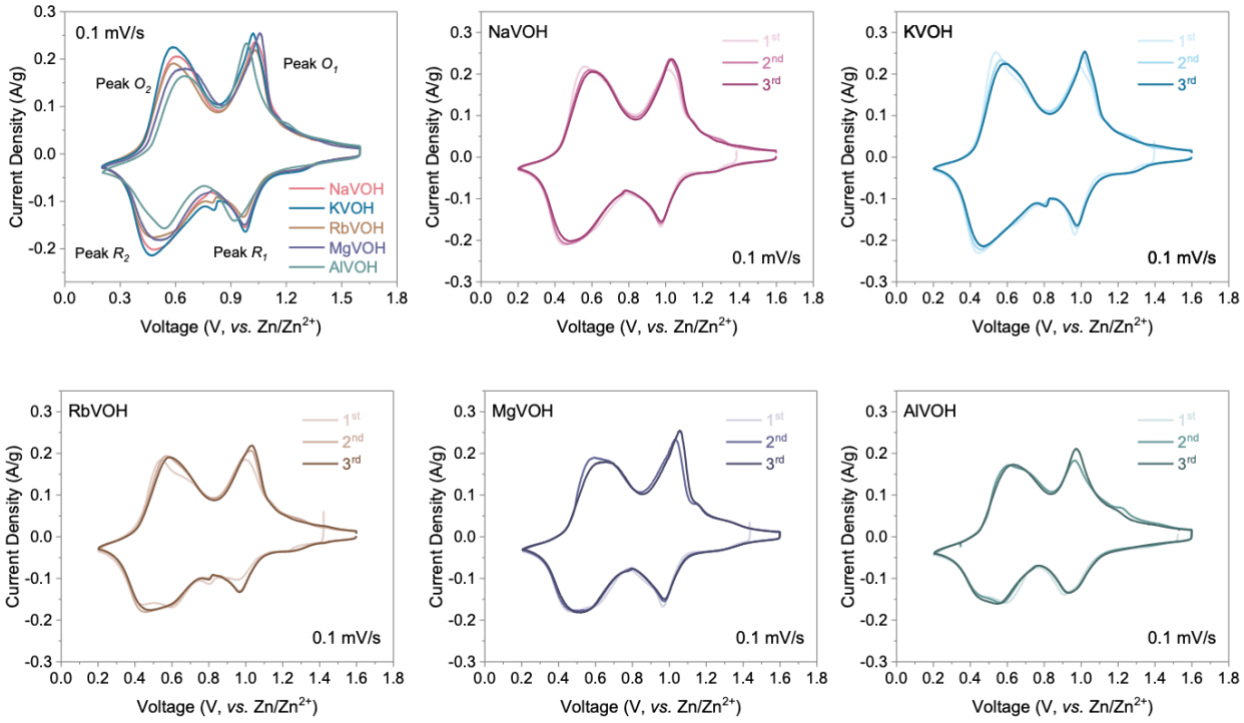

Figure 4.9. CV curves of ZIBs with the δ-$M_xV_2O_5{\cdot}nH_2O$ cathode at 0.1 mV s^{-1}.

Table 4.6. A comparison of peak positions and voltage gaps between redox pairs of δ-$M_xV_2O_5{\cdot}nH_2O$.

Sample	Peak Voltages (V)	Redox Pairs	Peak Separation
NaVOH	0.97/1.03	V^{5+}/V^{4+}	0.06 V
	0.48/0.59	V^{4+}/V^{3+}	0.11 V
KVOH	0.98/1.02	V^{5+}/V^{4+}	0.04 V
	0.47/0.59	V^{4+}/V^{3+}	0.10 V
RbOH	0.97/1.03	V^{5+}/V^{4+}	0.06 V
	0.48/0.59	V^{4+}/V^{3+}	0.11 V
MgVOH	0.97/1.06	V^{5+}/V^{4+}	0.09 V
	0.52/0.65	V^{4+}/V^{3+}	0.13 V
AlVOH	0.92/0.99	V^{5+}/V^{4+}	0.07 V
	0.54/0.65	V^{4+}/V^{3+}	0.11 V

4.4 ELECTROCHEMICAL KINETICS

To gain a deeper insight into the electrochemical kinetics of the δ-$M_xV_2O_5{\cdot}nH_2O$ material (M = Na, K, Rb, Mg, Al), CV curves were measured at various sweep rates, and a detailed kinetic analysis was conducted. With the scan rate increasing from 0.1 to 1.2 mV s^{-1} (Figure 4.10), all five samples exhibit a notable shift of reduction peaks to lower voltages and the oxidation peaks to higher voltages, owing to the amplified polarization at higher scan rates.

Initially, at low scan rates, the CV curves of five samples appear to be quite similar (Figure 4.9). However, as the scan rate increases, significant changes emerge in the current response of different peaks. Particularly noteworthy is the behavior of AlVOH, where the V^{4+}/V^{3+} pairs (~ 0.5 V) dominant the charge storage at 0.1 mV s^{-1}. Yet, at higher scan rates, the V^{5+}/V^{4+} pairs (~ 1 V) become predominant, exhibiting a higher current response.

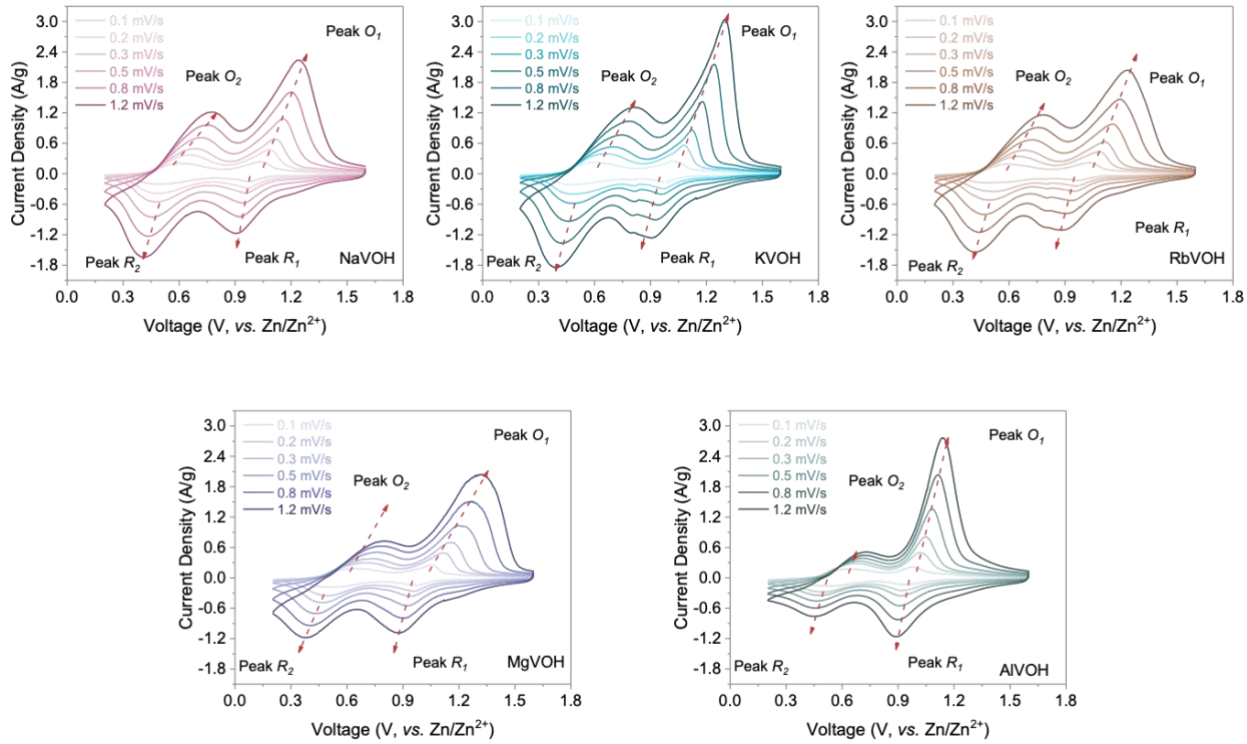

Figure 4.10. CV curves at various scan rates for δ-$M_xV_2O_5{\cdot}nH_2O$.

The *b*-value analysis of each redox peak is presented in Figure *4.11*. Notably, all four peaks in the δ-$M_xV_2O_5{\cdot}nH_2O$ material (M = Na, K, Rb, Mg, Al) exhibit *b* values in the range of 0.5 to 1.0, indicative of a combination of diffusion-controlled behaviors and surface-controlled capacitive behaviors for all samples.

Upon closer examination, it is observed that the O_2 peak possesses a smaller *b*-value compared to O_1, implying that the oxidation from V^{3+} to V^{4+} serves as the rate-limiting step during charging. This trend holds true for all five samples. Conversely, during the discharging process, the rate-liming step is the reduction between V^{5+}/V^{4+} for monovalent cation-stabilized VOH. However, for MgVOH and AlVOH, the rate limiting step becomes the reduction between V^{4+}/V^{3+}. This difference suggests that singly charged ion stabilized VOH allows for easier insertion of more Zn^{2+}, facilitating further reduction of vanadium. Conversely, for MgVOH and AlVOH, once all V^{5+} is reduced to V^{4+}, the insertion of additional Zn^{2+} becomes challenging, explaining their lower specific capacity. This phenomenon may be attributed to the stronger electrostatic interactions between the intercalated Zn^{2+} ions and the doubly charged Mg^{2+} and triply charged Al^{3+}.

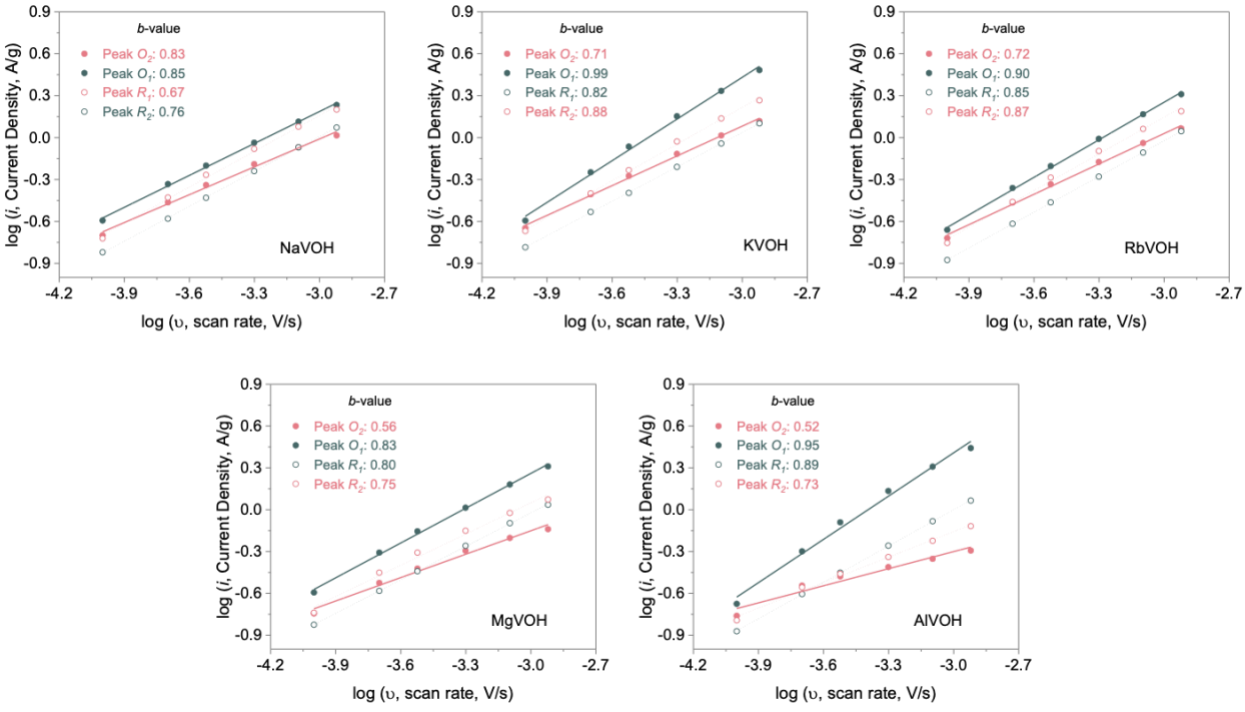

Figure 4.11. The *b*-values of each redox peak in CV curves for δ-$M_xV_2O_5{\cdot}nH_2O$.

4.5 CONCLUSIONS

This chapter investigated the effects of pre-intercalating various metal cations in the $V_2O_5{\cdot}nH_2O$ system, including Na^+, K^+, Rb^+, Mg^{2+}, and Al^{3+}. Firstly, the interlayer spacing of the resulting δ-$M_xV_2O_5{\cdot}nH_2O$ materials (M = Na, K, Rb, Mg, Al) was successfully tuned between 10.5 Å and 13.5 Å by introducing different metal cations. This variation in interlayer distance was found to be influenced by the interlayer water content, or hydration number, which increases with the hydrated ion radius but decreases with the electronegatively of the pre-intercalated metal cations.

Ion stabilization effects of these phases were evaluated in aqueous ZIBs. Notably, $K_{0.32}V_2O_5{\cdot}0.52H_2O$, with the second smallest interlayer distance (10.6 Å), exhibits the highest specific capacity (351 mA h g^{-1} at 4 A g^{-1}) and the best rate performance (73% capacity retention when current density increasing from 0.5 to 8 A g^{-1}). On the other hand, $Rb_{0.38}V_2O_5{\cdot}0.50H_2O$, with the smallest interlayer spacing (10.5 Å), demonstrates the highest cycling stability, with a capacity retention of 93% after 2000 cycles at 4 A g^{-1}.

Electrochemical performance analysis revealed no direct correlations between the interlayer spacing of δ-$M_xV_2O_5{\cdot}nH_2O$ and their cyclic stability or rate capability. This suggests that, since all δ-$M_xV_2O_5{\cdot}nH_2O$ possess a sufficiently large interlayer spacing for charge carriers, the interlayer distance will not be a key determinant of ion diffusion kinetics and host structure stability upon cycling.

Furthermore, monovalent cation-stabilized VOH exhibits better electrochemical kinetics, allowing for easier insertion of more Zn^{2+}. This phenomenon may be attributed to the weaker electrostatic interactions between cycled Zn^{2+} ions and the monovalent cations compared to Mg^{2+} and Al^{3+}.

Overall, this study provides valuable insights into the role of metal cation pre-intercalation in stabilizing the $V_2O_5{\cdot}nH_2O$ structure and its effects for enhancing the electrochemical properties. Further research may be warranted to explore additional factors influencing ion diffusion kinetics and cyclic stability in these δ-$M_xV_2O_5{\cdot}nH_2O$ systems.

Chapter 5. Chemical Pre-intercalation of Organic Cations

Adapted with permission from Xiaoxiao Jia, Chaofeng Liu, Zhi Wang, Di Huang, and Guozhong Cao. "Weakly Polarized Organic Cation-Modified Hydrated Vanadium Oxides for High-Energy Efficiency Aqueous Zinc-Ion Batteries." *Nano-Micro Letters* 16, 129 (2024). https://doi.org/10.1007/s40820-024-01339-y.

5.1 Background and Approach

An important consideration for the metal cation-preintercalated δ-$M_xV_2O_5{\cdot}nH_2O$ (M: metal ions) materials is the potential issue of strong interactions between the charge carrying cations and interlayer water molecules with the cycled ions. These interactions could potentially degrade both the structural stability and the ion transfer kinetics of the material. It was observed from the last chapter that the doubly charged Mg^{2+} stabilized $V_2O_5{\cdot}nH_2O$ and triply charged Al^{3+} stabilized $V_2O_5{\cdot}nH_2O$, despite having a more expanded interlayer distance, exhibit smaller specific capacity and worse cycling stability and rate capability compared to the singly charged ion stabilized $V_2O_5{\cdot}nH_2O$ phase (Na^+, K^+, and Rb^+).

In this perspective, an intriguing avenue of exploration involves the use of low polarized organic cations for chemical pre-insertion within the $V_2O_5{\cdot}nH_2O$ structure. The larger molecular size of organic species has the potential to further expand the interlayer distance beyond what is achievable with inorganic species. Additionally, the ionic nature of organic cations allows for stronger bonding with the host structure compared to neutral molecules. The low polarity of organic cations is expected to mitigate their electrostatic interactions with cycled ions during charging/discharging. This could potentially enhance the cycling stability and reversibility of the system. Exploring this approach may open up new possibilities for optimizing the performance of $V_2O_5{\cdot}nH_2O$-based materials in electrochemical applications.

In this chapter, we will use the organic salt, trimethylphenylammonium chloride ($C_6H_5N(CH_3)_3Cl$, TMPAC), as a precursor for synthesizing the organic cation-stabilized VOH ($[C_6H_5N(CH_3)_3]_{1.08}V_8O_{20}{\cdot}0.06H_2O$, TMPA-

VOH). Through this study, we aim to gain insights into how the presence of pre-intercalated organic cations influences the properties and performance of VOH-based materials, in the context of ZIBs applications.

5.2 Materials Characterization

TMPA-VOH is synthesized using the same hydrothermal conditions as VOH, with the addition of trimethylphenylammonium chloride (TMPACl) salts at a V_2O_5/TMPACl ratio of 2. The formation of dark green precipitates implies a significant reduction of V^{5+} to V^{4+}.[154] Figure 5.1a illustrates the XRD patterns of TMPA-VOH and VOH. VOH exhibits a typical layered structure with characteristic peaks (001), (003), (004), (005), well-matched to the $V_2O_5 \cdot 1.6H_2O$ pattern (JCPDS No.40-1296). [115] The main (001) peak at 2θ of 7.54° corresponds to an interlayer distance of approximately 11.7 Å in VOH. However, upon introduction of $TMPA^+$ cations, the diffraction peaks of TMPA-VOH align with those of the monoclinic (Na, Ca)(V, Fe)$_8O_{20} \cdot nH_2O$ phase (Space group: C2/m, JCPDS No. 45-1363).[155] As clearly depicted in Figure 5.1a, all the (00*l*) peaks of TMPA-VOH shift to a lower degree compared to the standard (Na, Ca)(V, Fe)$_8O_{20} \cdot nH_2O$ phase. Meanwhile, all the other peaks such as (201), (110), $(40\bar{1})$, $(11\bar{3})$, $(60\bar{1})$, (020), (021), and $(71\bar{1})$ remain at the same positions, strongly indicating that $TMPA^+$ has entered the interplanar space of the V-O structure. Compared to the standard (Na, Ca)(V, Fe)$_8O_{20} \cdot nH_2O$ pattern, the (00l) peak of TMPA-VOH shifts from 8.18° to 6.36°, corresponding to an expansion of lattice spacing from 10.8 Å to 13.9 Å. A schematic illustration of the TMPA-VOH structure is provided in Figure 5.1b. The [V_8O_{20}] layer is composed of four-fold [V_4O_{10}] chains, formed by (opposite) corner sharing [VO_6] octahedra (parallel to *b*). Those chains densely packed by sharing edges to form layers, with sufficient interlayer sites partially occupied by cations or water molecules.[155]

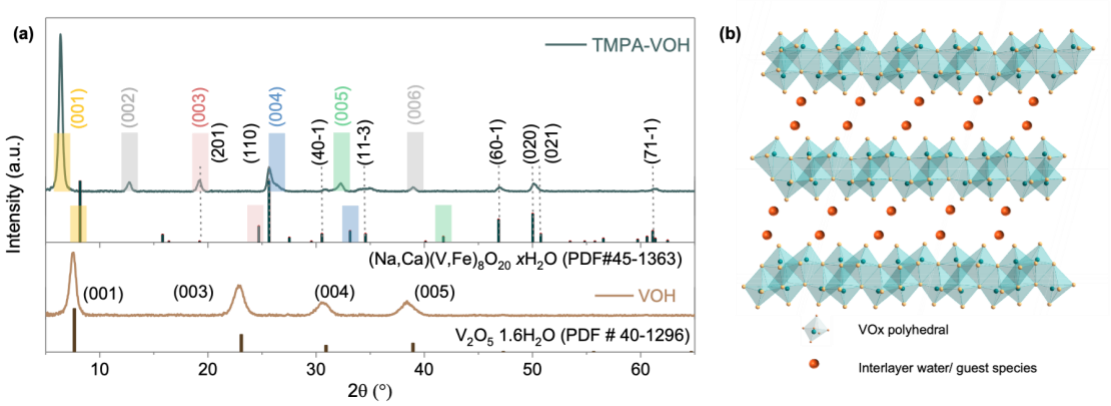

Figure 5.1. (a) XRD patterns of TMPA-VOH and VOH. (b) A schematic illustration of the $M_xV_8O_{20}{\cdot}nH_2O$ phase.

SEM images (Figure 5.2a) reveal that TMPA-VOH exhibits a three-dimensional flower-like/urchin-like morphology, comprising numerous long and ultrathin VO_x nanobelts. These nanobelts nucleate from the core and grow radially outward in all directions, typically reaching several micrometers in length and less than 100 nm in width (Figure 5.2c). This suggests a rapid diffusion-controlled crystal growth without secondary nucleation. The HRTEM image of TMPA-VOH (Figure 5.2d) displays lattice fringes with an interlayer spacing of 1.42 nm, corresponding to the *d*-spacing of (001) planes from the XRD pattern (Figure 5.1a), implying a preferential growth direction for the nanobelts. In contrast, VOH exhibits a more agglomerated and irregular morphology (Figure 5.2b), consisting of randomly stacked faceted flakes. This difference implies that the incorporation of $TMPA^+$ cation or the presence of TMPACl induces a significant morphology change.

Possible explanations for this morphological change might be: the uniformly distributed $TMPA^+$ cations in the V_2O_5 sol could (1) provide more initial nucleation sites, (2) alter the surface energy of nuclei and crystals by adsorbing $TMPA^+$ cations onto the surface, (3) lower the critical energy barrier of initial nucleation and/or subsequent crystal growth, and (4) slow the supply or diffusion of vanadium oxide growing species to the growth front. These factors lead to the formation of a morphology far from the thermodynamic equilibrium shape. The 3D micro flower-like morphology with ultrathin nanobelts of TMPA-VOH provides a larger accessible surface area for ion diffusion and more open space for electrolyte penetration, reducing the diffusion

pathways for guest ions. TEM-EDS element mapping (Figure 5.2e) confirm the uniform distribution of C, N, V and O throughout the entire TMPA-VOH architecture, validating the successful introduction of $TMPA^+$ into the V-O lattice. The molar ratio of N:V, calculated to be ~13.6% based on the SEM-EDS and TEM-EDS, gives an average stoichiometric formula of $(TMPA)_{1.08}V_8O_{20}\cdot nH_2O$ for TMPA-VOH.

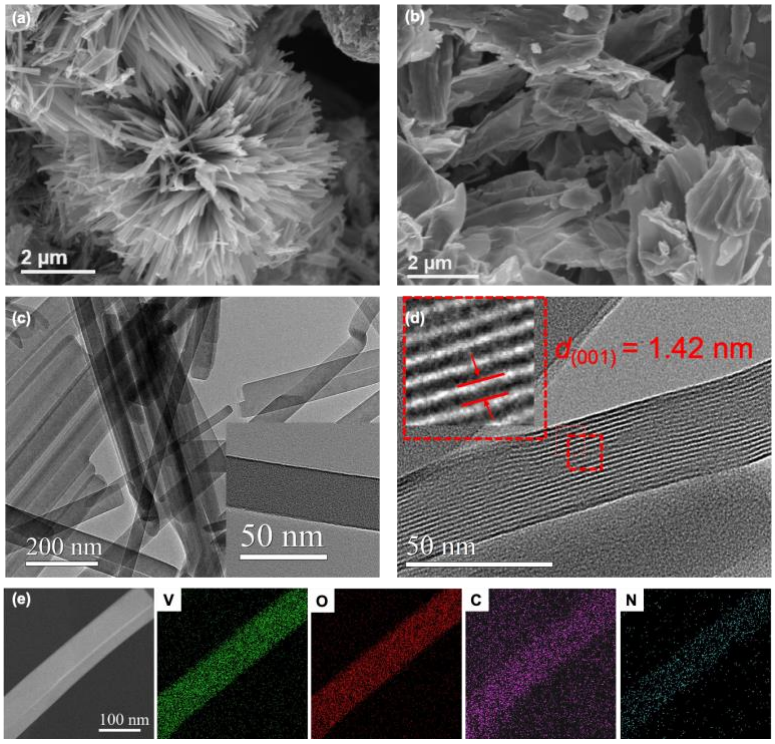

Figure 5.2. Morphological characterization of TMPA-VOH and VOH. SEM images of (a) TMPA-VOH and (b) VOH. (c, d) TEM images and (e) the corresponding EDS elemental mappings of TMPA-VOH.

In Figure 5.3, the water loss in VOH is divided into: (1) a first stage (< 150 °C) corresponding to the loss of weakly bonded water molecules (reversibly adsorbed between the V-O layers), and (2) subsequent stages (150 – 450 °C) corresponding to the removal of more tightly bonded water within the layers.[156] The stoichiometric formula of the prepared VOH was determined to be $V_2O_5\cdot 1.21H_2O$, with a total mass loss of 10.4% between 100 °C to 450 °C. Notably, in TMPA-VOH, there is a negligible mass loss in the first stage (below 150 °C), indicating the absence of reversibly adsorbed water molecules between layers. It can be inferred that intercalating $TMPA^+$ cations into the V-O ribbons is accompanied by the expulsion of interlayer water

molecules. The primary weight loss of TMPA-VOH (~17%) occurs between 150 °C – 450 °C, attributed to the removal of strongly bonded crystal water and the combustion of organic components in air. Based on the N content from EDS data (N: V~13.6%), the amount of $TMPA^+$ cation and crystal water can be estimated, determining the formula of TMPA-VOH roughly to be $(TMPA)_{1.08}V_8O_{20}\cdot 0.06H_2O$.

The combined results of XRD, SEM/TEM and TG affirm that the intercalation of large, weakly polarized organic $TMPA^+$ cations induces a phase change from $V_2O_5\cdot nH_2O$ to $(TMPA)_{1.08}V_8O_{20}\cdot nH_2O$. This transformation is characterized by an interlayer spacing expansion from 11.7 to 13.9 Å, a morphology change from randomly stacked faceted flakes to 3D spherical micro-urchins, and the extrusion of weakly bonded water molecules between interlayers.

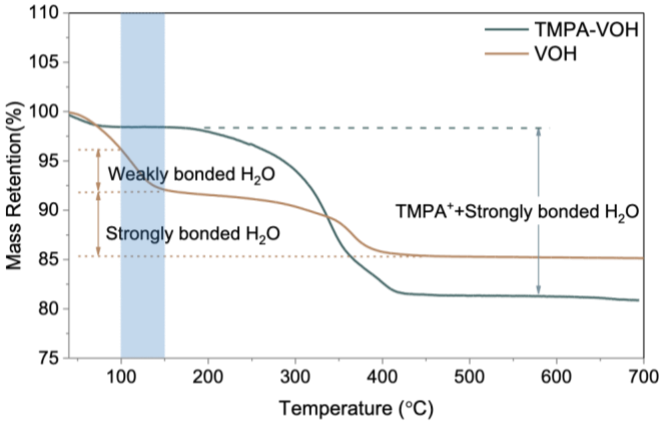

Figure 5.3. TG curves of TMPA-VOH and VOH.

The XPS survey spectra of TMPA-VOH (Figure 5.4a) reveal signals from V, O, N and C, confirming the presence of $TMPA^+$ cations in the material. Notably, no trace of Cl signal is detected in the survey spectra (Figure 5.4a) or the high-resolution Cl 1*s* spectra (Figure 5.4b), indicting the exclusive insertion of organic $TMPA^+$ cations without Cl^- anions. In the high resolution C 1*s* spectra of VOH (Figure 5.4c), in addition to the main line at the binding energy of 285.0 eV (C–C/C–H bonding), two other weak but recognized peaks at 286.7 eV and 288.5 eV are observed, assigned to the C–O, and O–C=O components.[157] These detectable carbon components in VOH originate from surface contamination, commonly observed in samples exposed

to the atmosphere.[158,159] In comparison to the C 1*s* of carbon contamination in VOH, the C 1*s* spectra of TMPA-VOH (Figure 5.4c) reveal a strong resolved peak at 286.5 eV, corresponding to the C–N bonds from the amino group in $TMPA^+$. The presence of C–N bonds or the amino group is also evident at 400.6 eV in the N 1*s* spectra (Figure 5.4d), where the other peak at 402.9 eV could be attributed to N–O bonds formed between $TMPA^+$ cations and oxygen in the vanadium oxide layer.[160,161] This further verifies the successful pre-intercalation of $TMPA^+$ cations into the VOH lattice and the formation of chemical bonds between nitrogen atoms (from $TMPA^+$) and oxygen atoms (on the interlayer surface of vanadium oxide).

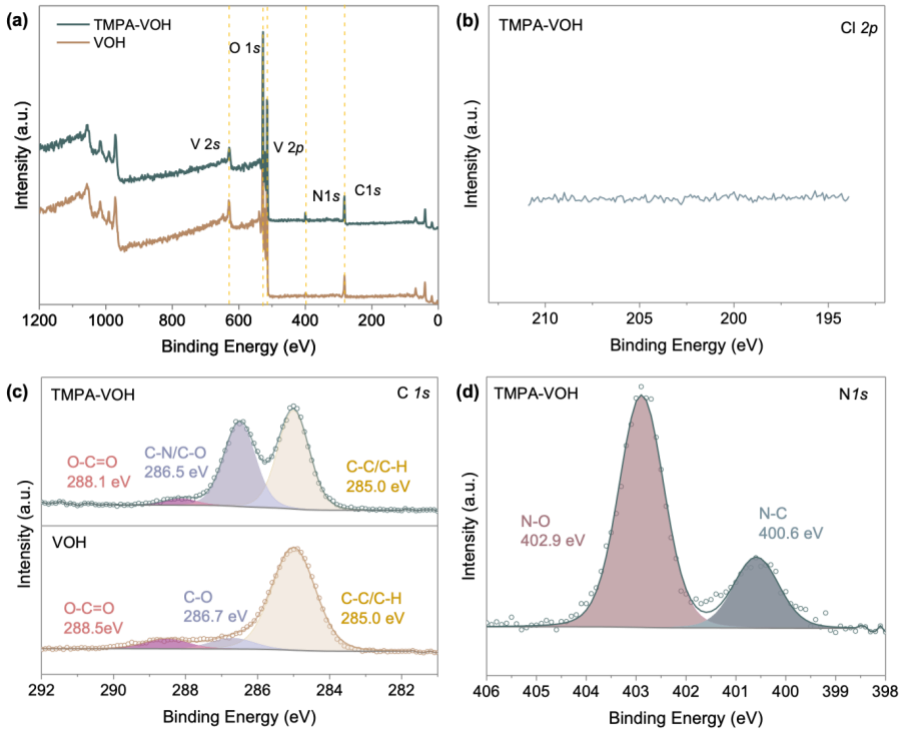

Figure 5.4. XPS analysis. (a) XPS survey spectra, showing a clear N signal in TMPA-VOH. High resolution of (b) Cl *2p* spectra of TMPA-VOH, showing no Cl signal. (c) C 1*s* spectra, a strong C–N peak in TMPA-VOH confirm the insertion of $TMPA^+$ cations. (d) N 1*s* spectra, indicating the presence of C–N bonds and the formation of N–O bonds in TMPA-VOH.

The high-resolution V $2p_{3/2}$ spectrum of TMPA-VOH (Figure 5.5a) reveals a prominent peak at 517.9 eV and a shoulder at 516.2 eV, corresponding to V^{5+} and V^{4+} ions, respectively.[157,162,163] From the fitted peak area, the ratio of V^{4+}/V^{5+} in TMPA-VOH is calculated to be 21.1%, resulting in an average vanadium valence state of +4.83 (in agreement with the literature data of 4.8).[155] In contrast, VOH has a V^{4+}/V^{5+} ratio of 6.8%, estimating

a vanadium valence state of +4.94. The substantial increase in the proportion of V^{4+} ions after $TMPA^+$ introduction promotes the hopping of unpaired electrons between V^{4+} and V^{5+}, enhancing the electronic conductivity and electrochemical kinetics of TMPA-VOH. An intriguing feature from Figure 5.5a is the full width at half maximum (FWHM) of the V 2$p_{3/2}$ peak in TMPA-VOH (1.23 eV), which is broader than that of VOH (1.14 eV). The V 2*p* width of vanadium oxides depends on the population of the *d* band; VO_x with more unpaired electrons exhibits a broader line.[162,164,165] The broadening of the V 2*p* line for TMPA-VOH suggests a higher concentration of electrons in the *d*-band, further illustrating the significant increase in V^{4+} ions after the introduction of $TMPA^+$.

The O 1*s* spectra of TMPA-VOH were deconvolved into three components at 530.5, 531.4, and 532.5 eV (Figure 5.5a). The dominant peak at 530.5 eV arises from the V-O lattice.[162,163] The latter two components can be assigned to C–O and H–O groups, coming from the surface contamination on the sample,[157,162] as also detected in the C 1*s* spectra (Figure 5.4c).[163] In the O 1*s* region of VOH, an additional peak at 533.7 eV is observed, related to the interlayer water molecules.[157,164] Notably, the corresponding peak is absent in TMPA-VOH, suggesting that the introduction of $TMPA^+$ cations not only intercalate into the interlayers but also expels the interlayer water molecules, consistent with the TG results.

The valence band (VB) spectrum of TMPA-VOH and VOH is presented in Figure 5.5b. Both samples exhibit a dominated band at ~ 6 eV (from O 2*p* contribution) and a low intensity band at ~1.5 eV (from V 3*d* contribution).[162] The O 2*p* component is associated with the emission from the vanadyl oxygen (center peak), chain oxygen, and bridge oxygen in the VO_x structure, hybridized with V 3*d*. The appearance of the V 3*d* component, which will not be observed in the orthorhombic V_2O_5, confirms the presence of V^{4+}, attributed to its higher electron density in the conduction band.[162,166] In comparison with VOH, the valance band of TMPA-VOH exhibits a slight shift to lower energy. This indicates increased V–O interactions in TMPA-VOH, possibly arising from the interaction of $TMPA^+$ with the VO_x interlayer surface, resulting in a subtle change in V–O bond length or angle.[167]

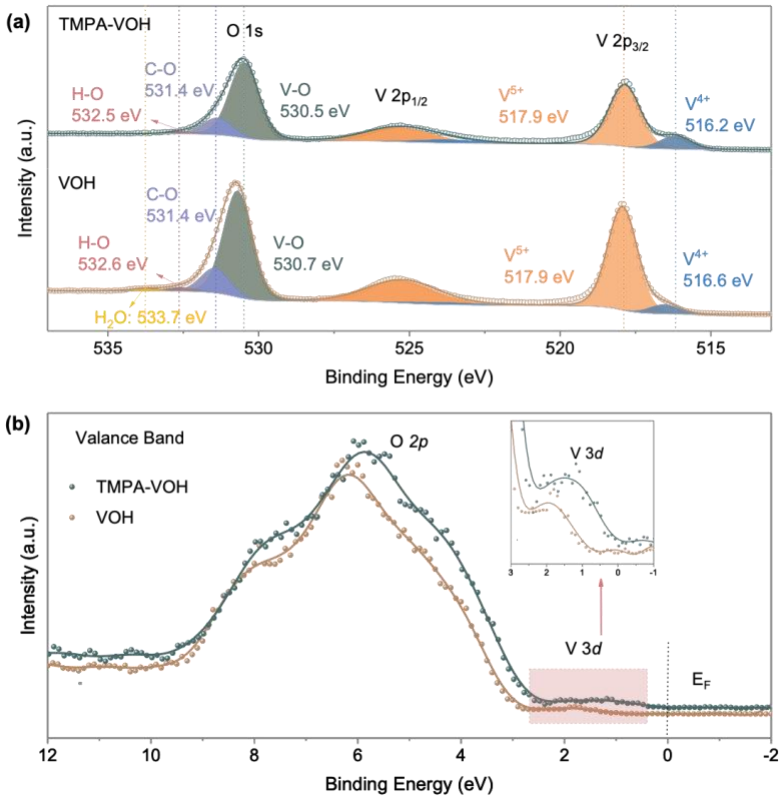

Figure 5.5. XPS analysis. (a) High resolution of V 2*p* and O 1*s* spectra, illustrating the introduction of a large amount of V^{4+} ions and the expulsion of interlayer water by $TMPA^+$ pre-insertion. (b) VB spectra.

Figure 5.6a displays the FTIR spectra of TMPA-VOH and VOH, with corresponding frequencies and assignments listed in Table *5.1*. In the TMPA-VOH spectra, distinctive peaks in the 1550-1200 cm^{-1} region (Region 1 in Figure 5.6a and Figure 5.6b) and 1030-1180 cm^{-1} region (Region 2 in Figure 5.6a and Figure 5.6c) correspond to characteristic vibration modes of $–N–CH_3$, $–CH_3$, and the C–H ring in the $TMPA^+$ salt,[168] affirming the presence of $TMPA^+$ in the TMPA-VOH lattice. In Figure 5.6a and d, peaks observed at 742 cm^{-1}, 975 cm^{-1}, and 1007 cm^{-1} in TMPA-VOH represent the characteristic bands of the vanadium oxide framework.[169,170] The 738 cm^{-1} peak in VOH is related to the asymmetric stretching of V–O–V bridging bands, with the shift to a higher wavenumber in TMPA-VOH (742 cm^{-1}) indicating a stronger V–O–V bond in TMPA-VOH.[169] The symmetric stretching of V–O–V observed at 586 cm^{-1} in VOH is not detected in TMPA-VOH.[171]

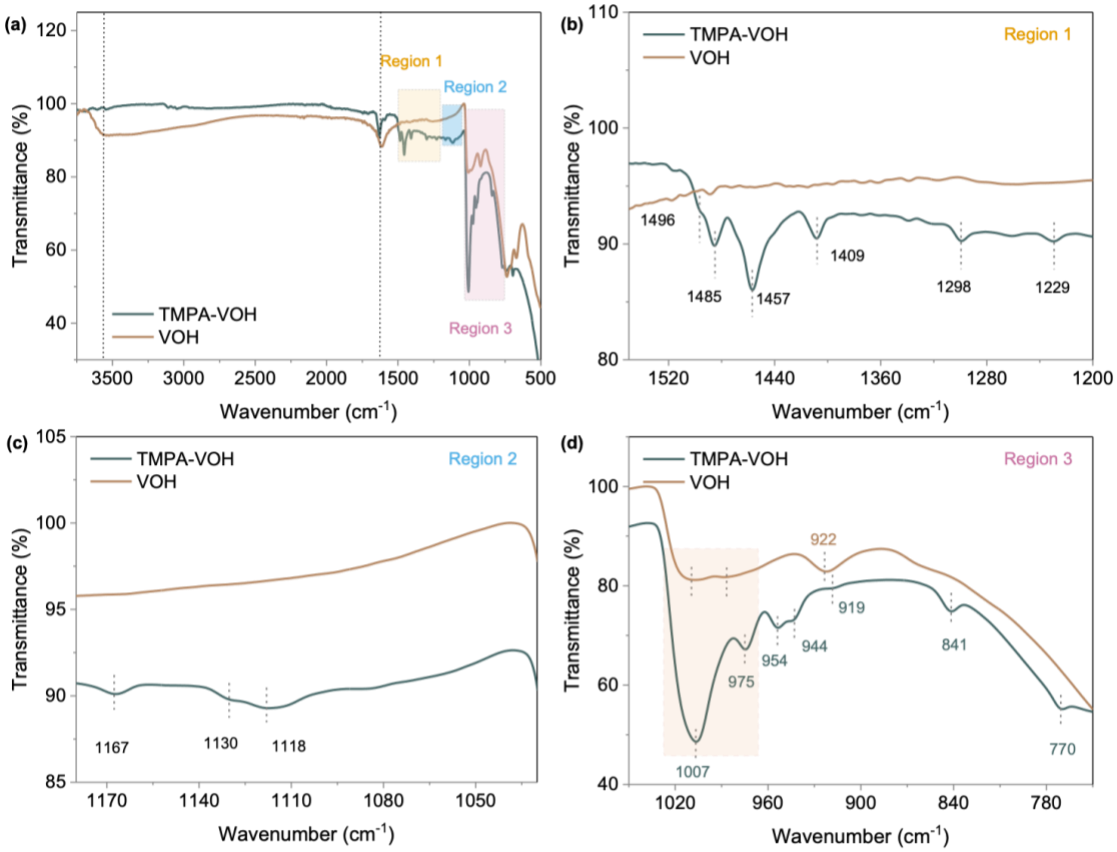

Figure 5.6. Chemical interactions characterization by FTIR. (a) FTIR spectra of TMPA-VOH and VOH. (b) FTIR spectra in the region of 1550-1200 cm^{-1} show the characteristic vibration modes of $TMPA^+$ species in TMPA-VOH. (c) FTIR spectra in the region of 1180-1030 cm^{-1}. (d) FTIR spectra in the region of 1050-750 cm^{-1} depict the splitting of the V=O peak and the absence of interlayer water in TMPA-VOH.

In the enlarged spectra (Region 3 in Figure 5.6a and Figure 5.6d), the broad peak near ~1010 cm^{-1} in VOH stems from the symmetric stretching of the terminal oxygen V=O bond. In TMPA-VOH, this V=O bond splits into two peaks at 1007 and 975cm^{-1}, possibly corresponding to the stretching vibrations of V^{5+}=O and V^{4+}=O, respectively.[169,170,172,173] The higher concentration of V^{4+} ions in TMPA-VOH (V^{4+}/V^{5+} ratio of 21.1%) results in a significant difference between the two signals, leading to a pronounced splitting of the V=O peak. In contrast, VOH has a lower proportion of V^{4+} ions (V^{4+}/V^{5+} ratio of 6.8%), making the splitting of the V=O peak less obvious. This phenomenon of separated V=O peaks has been observed in other systems, such as pyridine-$V_2O_5 \cdot nH_2O$ and Nitrogrn-doped V_2O_5, where the authors attributed it to the stronger interactions between PyH^+ and V=O and the V=O---H_4N^+, respectively.[174,175] In the spectrum of VOH, peaks at 3565 cm^{-1}

and 1613 cm^{-1} are related to the stretching of O–H and bending of H–O–H in the structural water molecules, respectively.[169,173] Notably, similar peaks are not well recognized in TMPA-VOH, suggesting the expulsion of most interlayer water upon $TMPA^+$ pre-intercalation, in agreement with the TG results.

Table 5.1. Frequencies and assignment of FTIR bands of TMPA-VOH and VOH.

Wavenumber/cm^{-1}		Assignment (vibration mode)
TMPA-VOH	VOH	
742	738	Asymmetric stretching of V–O–V
770	—	Out-of-plane ring deformation
841	—	$N–CH_3$ symmetric stretching + (N–C) stretching +ring (C–H) stretching
944	—	Out-of-plane ring (C–H) bending+CH_2 twisting
954	—	($N–CH_3$) streching+CH_3 rocking
975	less obvious	Stretching of V^{4+}=O
1007	less obvious	Stretching of V^{5+}=O
spitted	1010 (broad)	Stretching of V=O
1118	—	In-plane ring (C–H) bending+ (N–C) stretching+ CH_3 rocking
1130	—	CH_3 rocking
1167	—	In-plane ring (C–H) bending
1229	—	$N–CH_3$ asymmetric stretching
1298	—	In-plane ring (CCC) asymmetric stretching + CH_2 wagging
1409	—	CH_3 symmetric bending
1457	—	CH_3 asymmetric bending + In-plane ring (C–H) bending
1485	—	In-plane ring (C–H)+ CH_3 asymmetric bending
1496	—	CH_3 scissoring + In-plane ring (C–H) bending
	1613	H–O–H bending of water molecules
1632	—	C–H bending
—	3565	O–H stretching of water molecules

Electron paramagnetic resonance (EPR) spectroscopy was employed to provide direct evidence for the existence of paramagnetic V^{4+} species, whose outer shell electronic structure $3d^1$ has one unpaired electron to interact with the magnetic field. The EPR spectra of TMPA-VOH exhibit a prominent peak centered at a *g*-factor of 1.9728 (with a peak-to-peak line width of ~200 G), confirming the existence of V^{4+} ions (Figure 5.7a).[176] In Figure 5.7b, both TMPA-VOH and VOH display a symmetric signal at a *g* value of 2.003, originating from unpaired electrons captured at the oxygen sites (oxygen free radicals $O_2^{\cdot-}$).[177] The signal intensity of TMPA-VOH is notably stronger than that of VOH, indicating a higher content of unpaired electrons in TMPA-VOH and emphasizing the formation of more low-valance state V^{4+} ions following $TMPA^+$ intercalation.

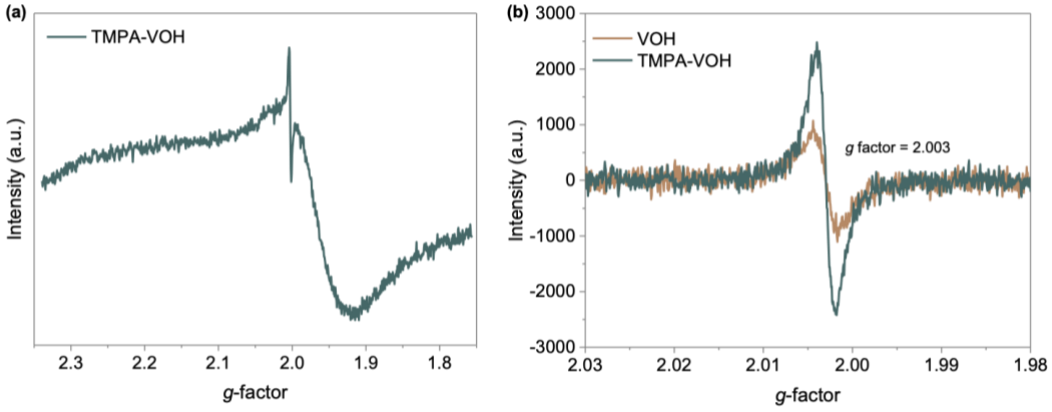

Figure 5.7. Chemical interactions characterization by EPR. (a) EPR spectra of TMPA-VOH show a strong peak at a *g*-factor of 1.9728. (b) EPR spectra of TMPA-VOH and VOH show a stronger signal of unpaired electrons in TMPA-VOH, confirming the presence of more V^{4+} species.

5.3 Electrochemical Performances

Figure 5.8a compares the 1st GCD curves of TMPA-VOH and VOH at 0.1 A g^{-1}. TMPA-VOH demonstrates a high open circuit voltage (OCV) of 1.58 V and an initial specific capacity of 451 mA h g^{-1}, surpassing that of VOH (OCV: 1.31 V, discharge capacity: 399 mA h g^{-1}). Additionally, the mid-point voltage difference of TMPA-VOH is 0.14 V, significantly lower than that of VOH (0.22 V), indicating a reduced discharge/charge overpotential for TMPA-VOH.

The rate performance of two samples is illustrated in Figure 5.8b. TMPA-VOH delivers discharge capacities of 403, 382, 355, 326, and 294 mA h g^{-1} at current densities of 0.5, 1, 2, 4, and 8 A g^{-1}, respectively, demonstrating an outstanding rate performance. In contrast, the discharge capacity of VOH decreases from 354 to 184 mA h g^{-1} with the current density increasing from 0.5 to 8 A g^{-1}, resulting in a capacity retention of 52%, much lower than that of TMPA-VOH (73%). The corresponding GCD curves of TMPA-VOH and VOH are depicted in Figure 5.8c. The narrower capacity gap between each change in current density and the smaller voltage gap between charge/discharge plateaus (e.g. the mid-point voltage difference at 0.5 A g^{-1} is 0.15 V for TMPA-VOH and 0.27 V for VOH) imply better tolerance to high rates and low polarization of TMPA-VOH, possibly arising from its promoted charge transfer and reaction kinetics.

A comparison of the cycling stability between TMPA-VOH and VOH is present in Figure 5.8d. At a current density of 4 A g^{-1}, TMPA-VOH exhibits a superior initial discharge capacity of 329 mA h g^{-1}, outperforming VOH (264 mA h g^{-1}). After 2000 cycles, TMPA-VOH maintains a remarkable capacity of 290 mA h g^{-1}, exhibiting a high retention of 87% (of the highest capacity). In contrast, VOH experiences rapid capacity decay, retaining only 162 mA h g^{-1} (61% retention) after cycling. Figure 5.8e compares the corresponding GCD profiles of the 1^{st} and the 2000^{th} cycle at 4 A g^{-1}. Following cycling, the degradation of VOH is evident not only in the reduced specific capacity but also in a significantly enlarged overpotential.

Another notable observation from Figure 5.8e is that the capacity decay in both samples primarily originates from the lower voltage plateaus (V^{4+}/V^{3+}), suggesting that the insertion of Zn^{2+} into the low-energy redox sites cannot be fully achieved. This difficulty arises from the gradual collapse of the V-O structure, driven by strong electrostatic interactions between divalent Zn^{2+} ions and the lattice. For TMPA-VOH, the introduction of weakly polarized organic cations serves to widen migration channels and weaken electrostatic interactions, promoting Zn^{2+} diffusion kinetics and preventing obvious structural deterioration and ensuring superior cycling stability.

Energy efficiency, a crucial metric calculated as the ratio of discharge specific energy to charge specific energy, provides a quantifiable measure of the energy consumed or released during the extraction or intercalation of working ions.[178] Charging and discharging at different rates not only impact specific capacity but also influence redox overpotential (Figure 5.8c). Therefore, plotting energy efficiency as a function of rates offers a more insightful perspective on the practical rate capability of the electrode. In Figure 5.8f, TMPA-VOH consistently demonstrates higher energy efficiency than VOH across all current densities. Notably, as the current density increases from 0.1 to 8 A g^{-1}, TMPA-VOH only experiences a moderate drop in energy efficiency, from 89% to 66%, corresponding to an impressive retention of 74%. In contrast, VOH shows a more substantial decay from 86% to 48%, with an energy efficiency retention of 56%.

The superior energy efficiency and its slower decline at higher charge/discharge rates in TMPA-VOH indicate lower overpotential and enhanced rate capability with $TMPA^+$ pre-intercalation. This improved reaction kinetics in TMPA-VOH may stem from: (1) its larger diffusion channels, facilitating a lower energy barrier for intercalation ions to reach redox sites; (2) its higher content of low valance state vanadium, providing more unpaired electrons for the conductivity of electroactive materials. Figure 5.8g presents a Ragone plot comparing the specific energy *vs*. specific power of our Zn//TMPA-VOH and Zn//VOH cells with recently reported aqueous ZIBs. Remarkably, the Zn//TMPA-VOH cell achieves the highest specific energy of 316 W h kg^{-1} at a specific power of 71 W kg^{-1} and a specific energy of 197 W h kg^{-1} at a high specific power of 4925 W kg^{-1}. These values not only surpass those of the Zn//VOH cell in our study but also outperform/match many other guest species-intercalated vanadium oxides, including PANI-VOH,[179] $NaCa_{0.6}V_6O_{16}\cdot 3H_2O$,[180] $([N(CH_3)_4]_{0.77},Zn_{0.23})V_8O_{20}\cdot 3.8H_2O$,[181] N-doped V_2O_5,[175] $Na_{0.33}V_2O_5$,[147] and $Ca_{0.24}V_2O_5\cdot 0.83\ H_2O$.[144]

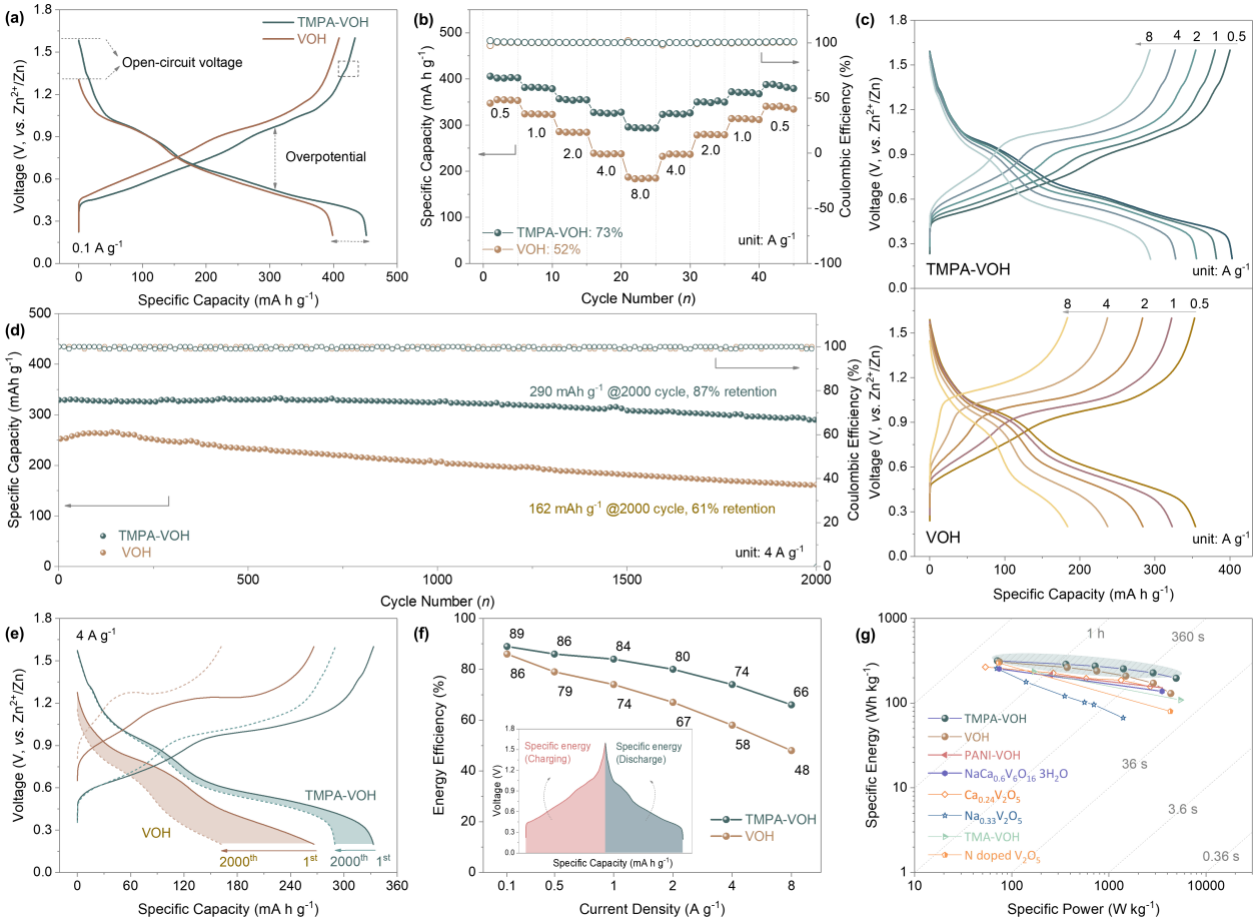

Figure 5.8. The electrochemical performance of Zn//TMPA-VOH and Zn//VOH cells. (a) The 1st GCD curve at 0.1 A g^{-1}. (b) Rate performance and (c) the corresponding GCD profiles at various current densities. (d) Cycling performance at 4 A g^{-1} and (e) GCD profiles of the 1st and 2000th cycle at 4 A g^{-1}. (f) Energy efficiency at various current densities, providing an alternative perspective on rate capability. (g) Ragone plot (specific energy and specific power, based on the weight of the active material in cathode, are derived from the GCD data).

In Figure 5.9a, a comparison of CV curves at a scan rate of 0.1 mV s^{-1} is presented for TMPA-VOH and VOH. VOH exhibits two distinct pairs of well-defined redox peaks at 0.98/1.06 and 0.45/0.65, representing the redox reactions between V^{5+}/V^{4+} and V^{4+}/V^{3+}, respectively.[105,113,115] Surprisingly, TMPA-VOH displays five couples of redox peaks: cathodic peaks centered at 1.33 V, 0.98 V, 0.91 V, 0.61 V, and 0.43 V, along with respective anodic peaks at 1.35 V, 0.99 V, 1.06 V, 0.67 V, and 0.51 V. This observation is further supported by the differential capacity (dQ/dV) *vs.* voltage curves at 0.5 A g^{-1} (Figure 5.9b), revealing five redox couples

in TMPA-VOH and aligning well with the CV results. While multiple redox peaks have been reported in various vanadium oxides,[182–184] the precise assignment of these peaks remains unclear in the literature.

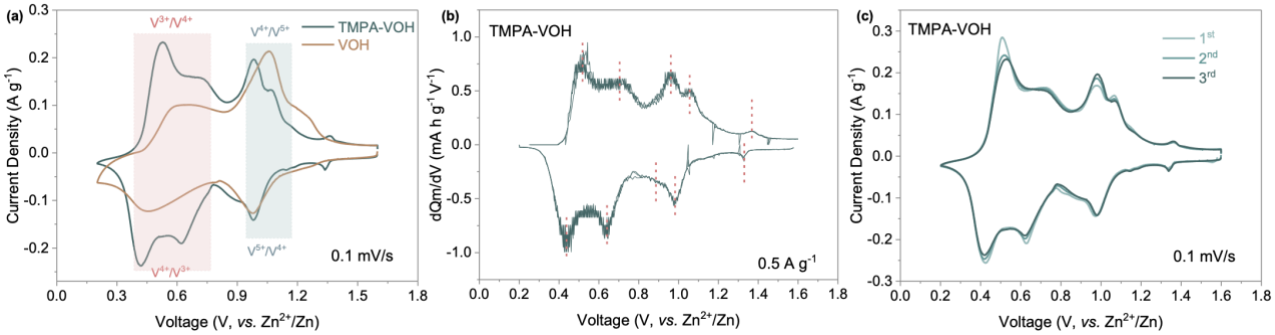

Figure 5.9. (a) The 3rd cycle of CV tests at a scan rate of 0.1 mV s^{-1}. (b) The dQm/dV vs. voltage profiles of TMPA-VOH. (c) The initial three cycles of CV tests at 0.1 mV s^{-1} for TMPA-VOH.

Firstly, from the initial three CV cycles of TMPA-VOH at 0.1 mV s^{-1} (Figure 5.9c), it becomes evident that the five couples of redox peaks in TMPA-VOH remain consistently present and nearly overlapped throughout subsequent cycles. This result strongly suggests the good reversibility of these redox reactions, effectively ruling out the possibility of irreversible phase transitions or structural changes. Secondly, as illustrated in Figure 5.10a, with an increase in the scan rate, two pairs of redox peaks around 0.5 V begin to merge into a single pair, so do the two pairs around 1 V. In other words, while TMPA-VOH exhibits five distinct redox pairs at low scan rates, it manifests only three redox pairs at high scan rate.

Based on these observations, it is likely that at the small scan rate of 0.1 mV s^{-1}, both pairs of redox peaks at 0.98/0.99 V and 0.91/1.06 V can be assigned to the V^{5+}/V^{4+} redox reaction, while both pairs at 0.61/0.67 V and 0.43/0.51 V represent the V^{4+}/V^{3+} redox centers. This split of vanadium redox peaks could be attributed to the existence of two distinct vanadium coordination in TMPA-VOH. During discharging/charging, the oxidation state of vanadium undergoes transitions between 5+, 4+, and 3+, coinciding with the transformation of the corresponding vanadium coordination polyhedra.[182,185] In TMPA-VOH, the existence of two distinct polyhedral coordination of vanadium is evident from the separate V=O peaks (V^{5+}=O and V^{4+}=O) in the FTIR spectra (Figure 5.6d). Consequently, the transformation of these two

types of vanadium coordination occurs at distinct redox voltages, and this becomes more apparent at low scan rates, where the redox reaction is relatively slow. Unlike VOH, where this redox peak split is undistinguishable in CV curves, consistent with the single or nearly merged V=O peaks in FTIR spectra. The additional tiny peak at 1.33/1.35 V suggests the emergence of a new redox site, with some attributing this to the interaction between the empty orbit of Zn^{2+} and the lone pair electrons of N.[175]

Further insights can be derived from the CV curves at 0.1 mV s^{-1} (Figure 5.9a). The voltage gap between each redox pair of TMPA-VOH is smaller than that of VOH, as detailed in Table 5.2). This indicates reduced polarization and accelerated reaction kinetics in TMPA-VOH, aligning with its diminished overpotential as evident from the reduced mid-point voltage difference in the GCD curves. The area enclosed by the CV curves corresponds to the charge storage in the material. Notably, the peak area under the V^{5+}/V^{4+} peaks is nearly the same for both samples. However, the peak area under the V^{4+}/V^{3+} pairs is significantly larger in TMPA-VOH than in VOH. This indicates that TMPA-VOH possesses more accessible redox sites in its structure, facilitating the insertion of more Zn^{2+} ions to reduce vanadium ions to V^{3+}. This finding is consistent with the higher specific capacity of TMPA-VOH obtained from the GCD tests.

Table 5.2. Peak positions and potential gaps between each redox pair of TMPA-VOH and VOH.

Sample	Peak Voltages (V)	Redox Pairs	Peak Separation (V)
TMPA-VOH	0.98/0.99	V^{5+}/V^{4+}	0.01
	0.91/1.06		0.15
	0.61/0.67	V^{4+}/V^{3+}	0.06
	0.43/0.51		0.08
	1.33/1.35		0.02
VOH	0.98/1.06	V^{5+}/V^{4+}	0.08
	0.45/0.65	V^{4+}/V^{3+}	0.20

5.4 Electrochemical Kinetics

CV tests were conducted at various scan rates (ranging from 0.1 to 1.2 mV s^{-1}) to reveal the Zn^{2+} ion storage kinetics in TMPA-VOH (Figure 5.10a). With increasing scan rates, the voltage difference between each redox pair expands, causing reduction peaks to shift to lower voltage and oxidation peaks to shift to higher voltage. In comparison to VOH (Figure 5.10c), TMPA-VOH exhibits a less significant enlargement in peak separation, indicating its reduced electrochemical polarization. *b* values, reflective of the dominant charge storage process, were derived from the *log* (peak current) *vs*. *log* (scan rate) plot (Figure 5.10b and d). For TMPA-VOH, the *b* values of peak O_1, R_1, O_2, R_2, O_3, and R_3 are 0.77, 0.96, 1.0, 0.84, 0.97, 0.96, respectively. These values suggest that the Zn^{2+} storage in TMPA-VOH involves a combination of diffusion-controlled behaviors and surface-controlled capacitive behaviors.[121]

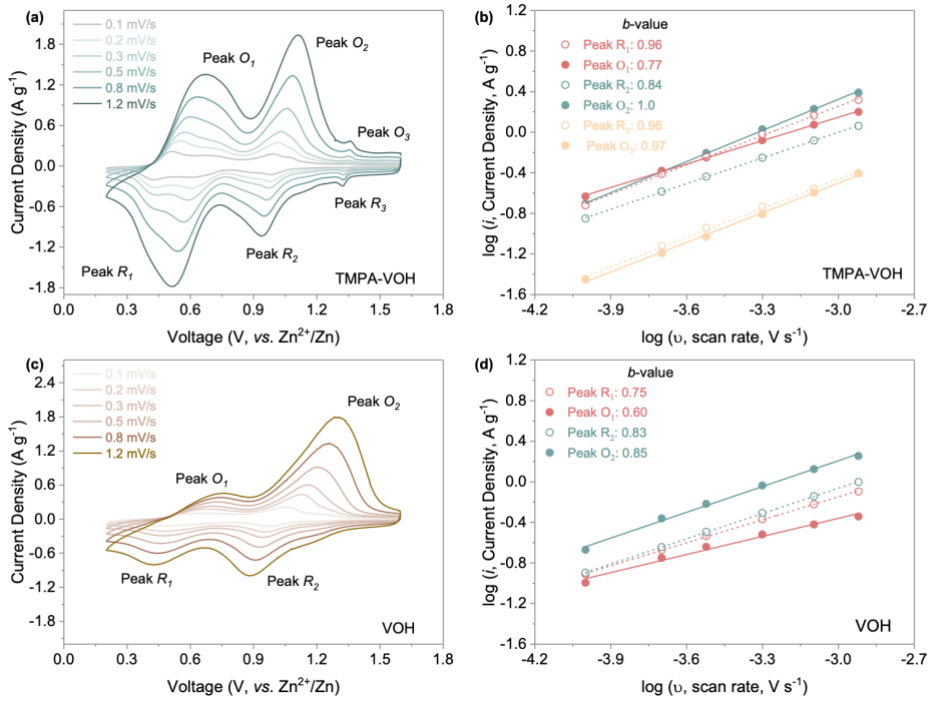

Figure 5.10. CV curves at various scan rates for (a) TMPA-VOH and (c) VOH. The *log* (peak current) *vs. log* (scan rate) plot for each redox peak and their *b* values for (b) TMPA-VOH and (d) VOH.

As summarized in Figure 5.11a and b, the contribution from each process can be quantitatively distinguished. Firstly, the capacitive contribution in TMPA-VOH at all sweep rates surpasses that in VOH, indicating an

overall faster reaction kinetics of TMPA-VOH. This enhanced pseudocapacitive behavior may be attributed to the large surface area and the wide interlayer spacing of TMPA-VOH. Secondly, since capacitive charge storage is sweep rate independent (Figure 5.11b), decreases in diffusion-controlled charge storage can serve as an effective indicator for evaluating the rate resistance of electrodes. As shown in Figure 5.11a, the contribution ratio of the diffusion-controlled process in TMPA-VOH declines less (from 30% to 11% with scan rate increasing from 0.1 to 1.2 mV s^{-1}) than that of VOH (from 46% to 20%), indicating a superior rate capability of TMPA-VOH. Thirdly, from Figure 5.11b, the specific capacitance/stored charge in TMPA-VOH (e.g. 1180 C g^{-1} at 0.1 mV s^{-1}) surpasses that of VOH (925 C g^{-1} at 0.1 mV s^{-1}), consistent with their specific capacify values from GCD tests. Additionally, as scan rates increase, the slower decay of specific capacitance in TMPA-VOH aligns with its improved rate performance (Figure 5.8b).

In summary, the kinetics analysis from CV data reveals that the charge storage in TMPA-VOH primarily results from the surface-controlled capacitive processes. The pre-intercalation of $TMPA^+$ cations enhances pseudocapacitive behavior and results in a slower decay in diffusion-controlled charge storage with increasing scan rate.

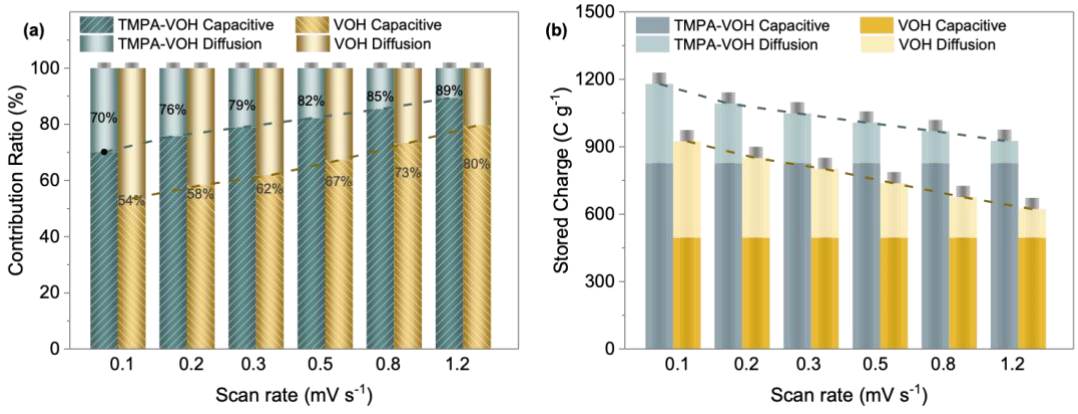

Figure 5.11. (a) Contribution ratio and (b) specific capacitance of the diffusion-controlled process and capacitive process for TMPA-VOH and VOH at different scan rates.

Figure 5.12a compares the Nyquist plots of TMPA-VOH and VOH before and after CV tests. Both spectra consist of a semicircle in the high frequency region, associated with the charge transfer resistance (R_{ct}) in electrodes, and a sloped line at low frequency, related to the ion diffusion process. Before cycling, the R_{ct} of TMPA-VOH (28 Ω) is notably half that of the pristine VOH electrode (57 Ω), highlighting improved electronic conductivity resulting from organic cation pre-intercalation. This enhancement is likely attributed to the increased density of unpaired electrons in TMPA-VOH, supported by the significantly higher amount of V^{4+} in TMPA-VOH (21.1%) compared to VOH (6.8%). After cycling, R_{ct} decreases for both TMPA-VOH and VOH, reaching 13 Ω and 26 Ω, respectively. The substantial reduction in R_{ct} after cycling may be ascribed to the small amount of residual Zn^{2+} in the structure, boosting the electrical conductivity of the cathode. Figure 5.12b illustrates the real part of impedance (Z') as a function of frequency ($\omega^{-1/2}$) in the low-frequency region. The line for the TMPA-VOH before cycling exhibits a smaller slope than VOH, indicating faster Zn^{2+} ion transport within TMPA-VOH. These EIS results underscore the active role of $TMPA^+$ introduction in enhancing the electrochemical reaction kinetics, particularly by boosting charge transfer conductivity.

The GITT was employed to compare the ion diffusion kinetics of TMPA-VOH and VOH at various charging/discharging stages. The calculated Zn^{2+} ion diffusion coefficients ($D_{Zn^{2+}}$) during the 3rd GITT cycle at 50 mA g^{-1} are presented in Figure 5.12c. TMPA-VOH exhibits $D_{Zn^{2+}}$ values ranging from 9.1×10^{-11} to 2.4×10^{-9} cm^2 s^{-1} during discharging and 1.9×10^{-10} to 2.0×10^{-9} cm^2 s^{-1} during charging. In contrast, VOH displays smaller $D_{Zn^{2+}}$ values, approximately 8.6×10^{-12}~1.5×10^{-9} cm^2 s^{-1} during discharging and 8.1×10^{-11}~1.0×10^{-9} cm^2 s^{-1} during charging. Compared with VOH, the faster Zn^{2+} ion diffusion rate of TMPA-VOH throughout the entire intercalation/de-intercalation process indicates that the pre-insertion of $TMPA^+$ into V-O layers effectively benefits the transport of charge carriers.

As demonstrated in Figure 5.12c, both systems exhibit relatively stable diffusivity at the beginning of the discharge process, followed by a rapid decrease after 1.0 V. Initially, the layered structure with large

channels allows the "free" insertion of Zn^{2+} ions; afterwards, deep intercalation is hindered due to the increasing electrostatic interactions between the inserted Zn^{2+}. However, this diffusivity decay is more significant in VOH than in TMPA-VOH, especially at lower voltage. This supports the previous statement derived from the CV curves that TMPA-VOH can accommodate more Zn^{2+} ions, inserting into the deeper lattice to reduce more V^{5+}/V^{4+} to V^{3+}.

Another important factor, internal resistance, can be estimated from the IR-drop in the GITT results (Figure 5.12d). Internal resistance represents the overall resistance in electrochemical reactions, originating from active materials, current collectors, conductive additives, contact between each element, and electrolyte conductivity. Throughout the charge/discharge process, the internal resistance values for TMPA-VOH are consistently lower than those of VOH (Figure 5.12d), contributing to a reduced overpotential and higher energy efficiency for TMPA-VOH, as confirmed by previous GCD and CV results. During discharging (Figure 5.12d), the internal resistance of VOH displays two steps of increase at ~ 1.2 and 0.6 V, coinciding with the two-step redox reactions upon the Zn^{2+} intercalation. The dramatic increase in resistance towards the end of discharge in VOH is a consequence of kinetic limitations, attributed to increased concentration polarization and electrochemical polarization. In contrast, the internal resistance of TMPA-VOH remains relatively stable throughout the entire discharge process, further indicating the reduced electrostatic interactions between the inserted Zn^{2+} and the lattice, facilitating the insertion of more Zn^{2+} ions into the TMPA-VOH lattice.

Benefiting from the 3D flower-like morphology, a wide interlayer spacing, and a large amount of V^{4+} with more unoccupied electrons, TMPA-VOH exhibits an accelerated ion diffusion rate and improved charge transfer kinetics. The low polarity of the pre-inserted organic ions minimizes interactions with the cycled Zn^{2+} ions, resulting in reduced polarization. Moreover, the pre-intercalation of organic cations has a significant impact on preventing the decay in diffusion rate and the increase in internal resistance upon deep discharging, enabling relatively stable kinetics throughout the entire discharging/charging process.

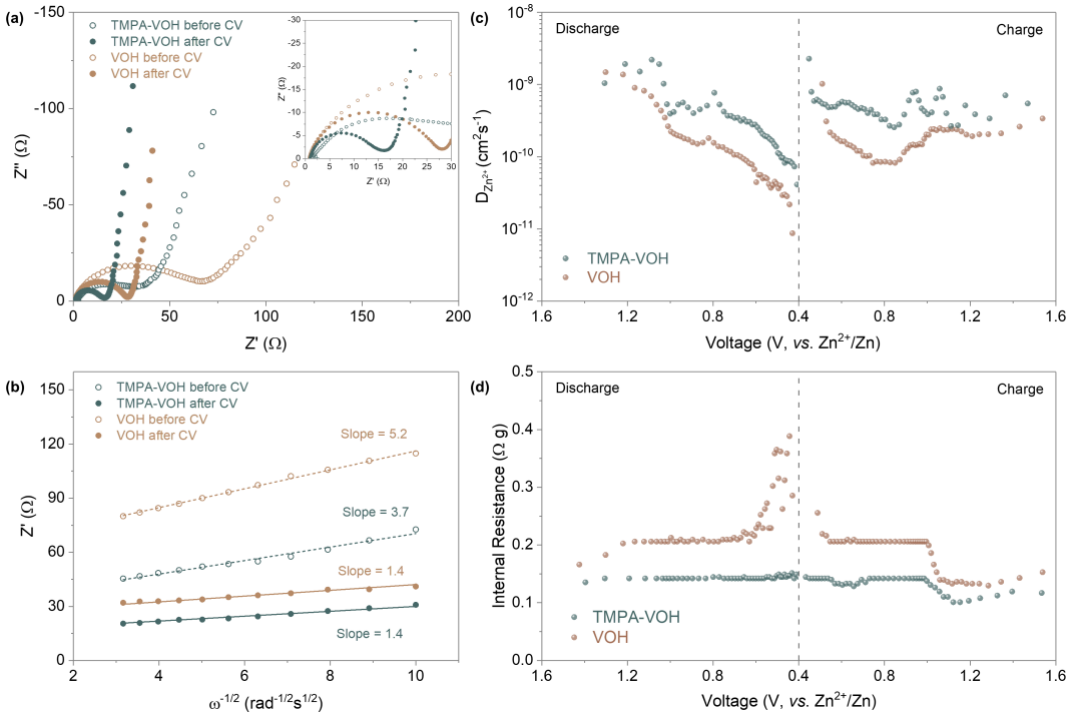

Figure 5.12. Electrochemical reaction kinetics analysis. (a)Nyquist plots of TMPA-VOH and VOH electrodes before and after CV tests. (b) Plot of the real part of impedance *vs.* $\omega^{-1/2}$ in the low-frequency region. (c) Zn ion diffusion coefficients and (d) internal resistance calculated from the 3rd cycle of GITT tests.

5.5 Zn^{2+} Ion Storage Mechanism

Figure 5.13a displays the XRD pattern of TMPA-VOH electrodes in the pristine state, fully discharged state (0.2 V) and fully charged state (1.6 V) during the first cycle. The XRD pattern of the pristine electrode closely matches the as synthesized TMPA-VOH powder and the Ti current collector. Upon complete discharge to 0.2 V, there is no significant shift in the position of the (00*l*) peak, indicating minimal expansion or contraction of the interlayer distance during Zn^{2+} intercalation into the structure. This contrasts with some reported vanadium oxides that exhibit noticeable interlayer expansion, which was attributed to screened electrotactic repulsions between V–O layers caused by inserted Zn^{2+}.[113] Conversely, certain vanadium oxides demonstrate an obvious interlayer contraction explained by the electrostatic attractions between Zn^{2+} and the host structure, pulling the layers closer.[160,181,186] The negligible interlayer spacing variation in TMPA-VOH suggests alleviated electrostatic interactions

between intercalated Zn^{2+} ions and the V-O lattice due to $TMPA^{+}$ pre-insertion.[120] This reduction in electrostatic interactions is beneficial for Zn^{2+}diffusion and structural stability during cycling.

It is noteworthy that no discernible new peaks are identified in the discharged electrode, which is different from observations in some studies where the generation of byproducts or secondary phases, such as $Zn_x(CF_3SO_3)_y(OH)_{2x-y}\cdot nH_2O$ or $Zn_3(OH)_2V_2O_7\cdot 2H_2O$, is commonly observed during the discharging process.[179] In the case of TMPA-VOH, characteristic peaks of $Zn_x(CF_3SO_3)_y(OH)_{2x-y}\cdot nH_2O$ or $Zn_3(OH)_2V_2O_7\cdot 2H_2O$ phases cannot be clearly detected, possibly due to the low abundance of new phases generated during discharging, resulting in an XRD signal too weak to be identified.[181] Additionally, the main peaks corresponding to $Zn_3(OH)_2V_2O_7\cdot 2H_2O$ (JCPDS No. 50-0570) appear at 12.3°, 20.9°, 30.1° and 34.2°,[187] closely located to the peaks of (002), (003), $(40\bar{1})$, and $(11\bar{3})$ planes of TMPA-VOH (at 12.6°, 19.2°, 30.8°, and 34.7°, respectively), making it even more challenging to differentiate the new phases from the main peaks. However, based on the XPS results, we speculate the formation or disappearance of these new phases upon discharging or charging (as discussed later). This phenomenon is similar to that observed in $(Na,Mn)V_8O_{20}\cdot nH_2O$ [188] and $[N(CH_3)_4]_{0.77},Zn_{0.23})V_8O_{20}\cdot 3.8H_2O$ [181].

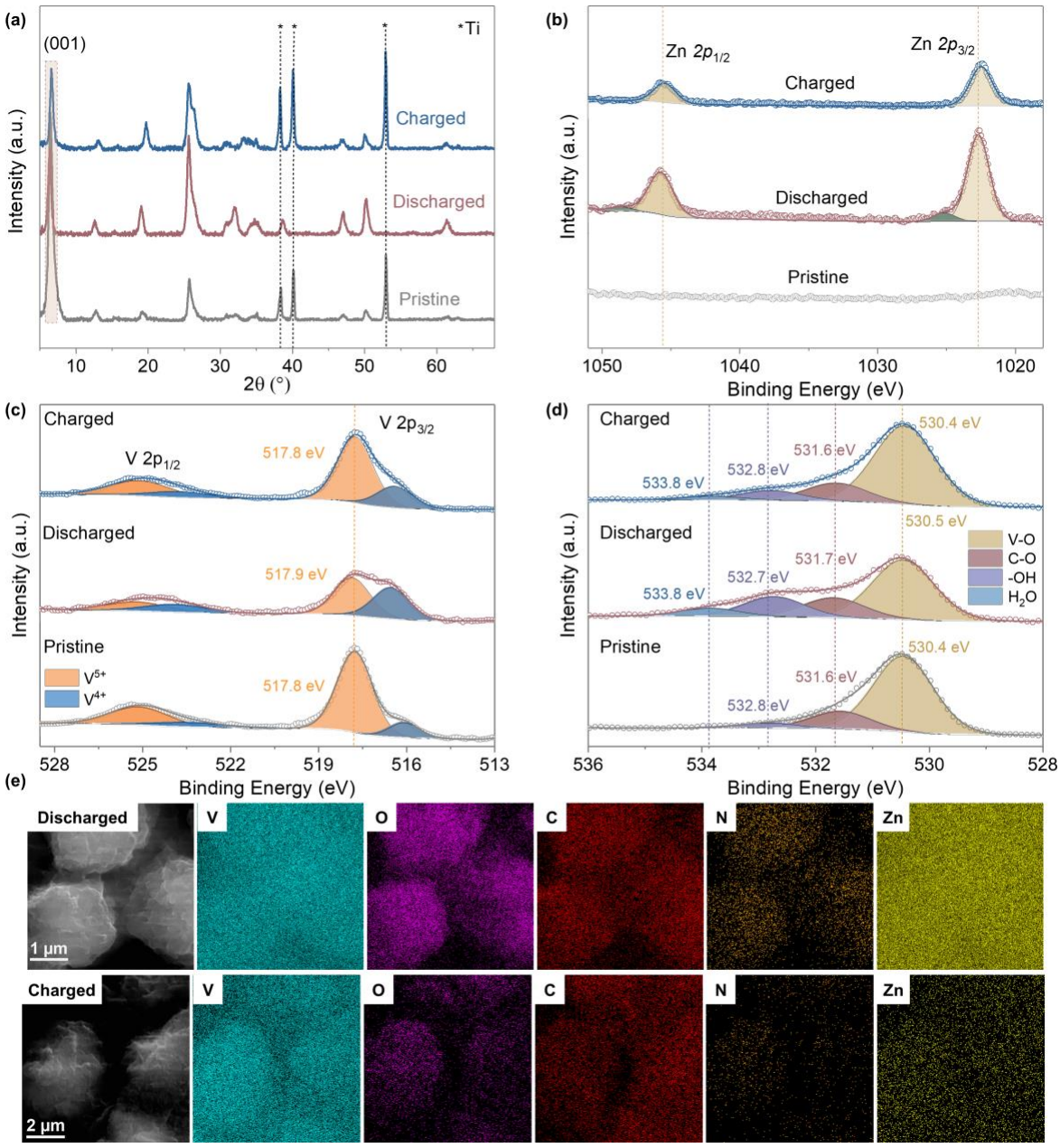

Figure 5.13. Energy storage mechanism of Zn//TMPA-VOH. (a) *Ex situ* XRD patterns. *Ex situ* XPS of (b) Zn 2*p* spectra, (c) V 2*p* spectra, and (d) O 1*s* spectra. (e) SEM elemental mapping images of TMPA-VOH cathode at discharged and charged state.

As shown in the Zn 2*p* XPS spectra (Figure 5.13b), no signal is detected for the pristine electrode. When discharged to 0.2 V, strong Zn peaks clearly appear, confirming the intercalation of Zn^{2+} into TMPA-VOH. Upon charged to 1.6 V, the Zn signal is still present but with reduced intensity, suggesting the incomplete extraction of Zn^{2+} from the TMPA-VOH structure. These residual Zn^{2+} ions are believed to be trapped in the host lattice, contributing to enhanced electronic conductivity, as reflected by the

reduced charge transfer resistance after cycling (as evidenced by EIS data). Notably, the discharged electrode shows two Zn components in the Zn 2$p_{3/2}$ region, a strong one at 1022.7 eV and a small side one at 1025.2 eV, which can be assigned to the intercalated Zn^{2+} in TMPA-VOH and the Zn precipitate (e.g. $Zn_x(CF_3SO_3)_y(OH)_{2x-y}\cdot nH_2O$ or $Zn_3(OH)_2V_2O_7\cdot 2H_2O$) generated on the surface.[189,190] After being fully charged, the latter peak disappears, with only the peak associate with intercalated Zn^{2+} showing at 1022.5 V, suggesting the reversible generation/dissolution of the zinc second phase.

The V 2*p* region is displayed in Figure 5.13c. Consistent with the as-synthesized TMPA-VOH material (Figure 5.5a), two peaks corresponding to V^{5+} (517.8 eV) and V^{4+} (516.1 eV) exist in the pristine electrode, with V^{5+} being the dominant one. After discharge, the signal of V^{4+} intensifies and becomes the major component, while that of V^{5+} decreases, indicating the reduction of vanadium ions accompanied with the intercalation of Zn^{2+}. A shift in the binding energy of V in the discharged state could be attributed to the interactions between intercalated Zn^{2+} and the V–O layers.[191] A smaller shift of the V^{5+} peak in TMPA-VOH (0.1 eV) compared to other guest species pre-intercalated vanadium oxides, like Cr-VOH [192] or Polypyrrole-VOH [193], suggests reduced electrostatic interactions due to $TMPA^+$ pre-intercalation. Interestingly, the V^{3+} signal was not observed in the discharged electrode. Although, based on the CV curves or the specific capacity of TMPA-VOH (451 mA h g^{-1}), there exists a valence conversion from +4 to +3 in vanadium. This phenomenon is widely observed for other vanadium-based cathode,[105,194] as trivalent vanadium cations are very unstable and can be easily oxidized during sample handling (exposed to air) and *ex situ* XPS characterization. After complete charging, both the position and fraction of vanadium spectra return to the initial state, demonstrating the reversible redox reaction. The slightly higher amount of V^{4+} in the charged electrode than in the pristine electrode can be ascribed to the incomplete de-intercalation of Zn^{2+} in the first charging process, in agreement with the Zn 2*p* spectra analysis (Figure 5.13b).

In Figure 5.13d, the O 1*s* spectra of the pristine electrode reveal three distinct components at 530.4 V (attributed to lattice oxygen in the V–O matrix), 531.6 V (indicative of C–O from surface contaminations), and 532.8 eV (corresponding to surface O–H species). Upon complete discharge, an additional peak emerges at 533.8 eV, possibly associated with H_2O molecules. This may be attributed to the insertion of hydrated zinc ions or the formation of $Zn_x(CF_3SO_3)_y(OH)_{2x-y}{\cdot}nH_2O$ or $Zn_3(OH)_2V_2O_7{\cdot}2H_2O$. The appearance of the H_2O peak, along with the strengthening of the –OH peak, indicates the possible formation of $Zn_x(CF_3SO_3)_y(OH)_{2x-y}{\cdot}nH_2O$ or $Zn_3(OH)_2V_2O_7{\cdot}2H_2O$, consistent with the Zn spectra analysis. Upon charging, the diminishing –OH peak and H_2O peak suggest the decomposition of these newly formed phases. The –OH in the zinc complex arises from the dissociation of water molecules in the electrolyte, induced by the intercalation of H^+ into the cathode.[195] Therefore, a Zn^{2+}/H^+ co-intercalation mechanism can be reasonably proposed for TMPA-VOH, aligning with many other vanadium oxide cathodes.[160,181,188]

As demonstrated in the *ex situ* SEM images (Figure 5.13e), there is no significant morphological evolution of TMPA-VOH during charging and discharging. The homogeneous distribution of V, O, N, C, and Zn across the sample further confirms the insertion of Zn^{2+} into TMPA-VOH and the stability of $TMPA^+$ cation during discharging/charging. The weak Zn signal detected at the fully charged state suggests the incomplete extraction of Zn^{2+} ions, which agrees with the XPS data. Based on the XRD, XPS, and SEM analyses, the energy storage mechanism of Zn//TMPA-VOH involves a Zn^{2+}/H^+ co-insertion. The pre-intercalation of $TMPA^+$ cations significantly decrease the electrostatic interactions between inserted Zn^{2+} and the V-O lattice, resulting in negligible interlayer variation and structural evolution during discharging/charging. This phenomenon is responsible for the enhanced kinetics and stability observed during cycling.

5.6 CONCLUSIONS

In this work, weakly polarized organic cations ($TMPA^+$) were employed as a novel pre-intercalated species to regulate the structure of vanadium oxide. The resulting $[C_6H_5N(CH_3)_3]_{1.08}V_8O_{20}\cdot 0.06H_2O$ (TMPA-VOH) exhibits enhanced electronic and ionic transports, along with a strengthened structure, attributed to several key factors: (1) the expanded interlayer spacing accelerates Zn^{2+} diffusion and reduces the migration energy barrier; (2) the expelling of interlayer water by the pre-inserted low polarity organic cations alleviates the electrostatic interactions between cycled Zn^{2+} ions and the lattice, minimizing the degradation in both structural stability and ionic diffusivity during cycling; (3) the increased amount of low valence-state V^{4+} provides more unpaired electrons for electronic conductivity; (4) the porous flower-like morphology, constructed from thin nanobelts, shortens ion diffusion pathways and facilitates fast near-surface activities. Capitalizing on these effects, when employed as cathodes in aqueous ZIBs, TMPA-VOH demonstrates enhanced capacitive behavior, reduced battery polarization, and achieves a high open circuit voltage of 1.58 V, a large specific capacity of 451 mA h g^{-1} (at 0.1 A g^{-1}) with an energy efficiency of 89%, high rate capability (294 mA h g^{-1} at 8 A g^{-1}) and long-term cycling stability with a capacity retention of 87% after 2000 cycles.

Chapter 6. Effects of Different Pre-intercalated Organic Cations

6.1 Background and Approach

The previous work has demonstrated that organic cations can be effectively pre-intercalated into vanadium oxides using the same synthesis methods as those for inorganic cations. This is particularly advantageous due to the lower polarity of organic cations, which helps reduce electrostatic interactions with cycled ions during charge/discharge processes, potentially mitigating capacity fading and enhancing rate capability. Additionally, the larger size of organic cations compared to metal cations can further expand the interlayer distance, facilitating better diffusion of guest ions within the cathode structure.

While interlayer distance plays a significant role, other factors, such as the nature of chemical bonding between pre-intercalated species and the host material, the amount of V^{4+} and water molecules within the interlayer space, and the electrostatic interactions between the pre-intercalated species and cycled ions, are also crucial in determining the electrochemical kinetics and stability of the system. Comparing the effects of various organic cations requires an understanding of how their structure, properties, and electrochemical performance differ. Investigating these aspects will provide valuable insights into the distinct behaviors and potential advantages of organic cation-based intercalation strategies.

This study involves selecting two alkylammonium cations, $CH_3NH_3^+$ and $N(CH_3)_4^+$, to explore how variations in alkyl chain structures, sizes, weights, and polarities affect their pre-intercalation effects on VOH materials. The ammonium cation (NH_4^+) pre-intercalated vanadium oxide will be used as a reference material. The synthesis of these pre-intercalated compounds will follow the established hydrothermal methods used for inorganic ions to ensure consistency. Direct data on the polarity of organic cations is challenging to find in databases. However, we can infer relative polarity by using melting points as an indicator. A higher melting point usually suggests stronger intermolecular interactions. Given that all three pre-intercalated precursors are chlorides, we assume that a higher melting point corresponds to a more ionic

or polar nature. Based on their melting point (as shown in Table 6.1), we predict the sequence of polarity for the three cations to be: methylammonium (MA^+) < ammonium (A^+) < tetramethylammonium (TMA^+).

Table 6.1. Structure, molecular weight, ionic radius, and melting point of pre-intercalated organic precursors selected in this study.

Precursor Salts	Formula	Structure	Mw	Effective ionic radius	Melting point
Ammonium chloride	NH_4Cl	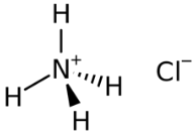	53.49 g mol^{-1}	A^+: 1.4-1.7 Å	338 °C
Methylammonium chloride	CH_3NH_3Cl	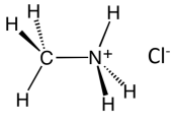	67.52 g mol^{-1}	MA^+: 2.2 Å	225-230 °C
Tetramethylammonium chloride	$N(CH_3)_4Cl$	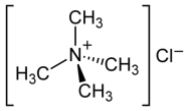	109.60 g mol^{-1}	TMA^+: 3.6 Å	425 °C

6.2 MATERIALS CHARACTERIZATION

Figure 6.1 displays the XRD patterns of $(Org)_xV_8O_{20}{\cdot}nH_2O$ materials (Org = ammonium (A), methylammonium (MA), and tetramethylammonium (TMA)), all identified as the monoclinic (Na, Ca)(V, Fe)$_8O_{20}{\cdot}nH_2O$ phase (Space group: C2/m, JCPDS No. 45-1363), [155] with no detectable impurity peaks. The XRD patterns of all three samples exhibit characteristic (00*l*) diffractions, indicative of the lamellar structure of bilayered vanadium oxides.

The lattice spacing of the primary (001) plane is measured as 10.6 Å (at 8.30°) for A-VOH, 11.2 Å (at 7.92°) for MA-VOH, and 12.6 Å (at 7.02°) for TMA-VOH. The observed interlayer spacing differences among samples (e.g., 1.4 Å difference between TMA-VOH and MA-VOH) correlate well with the variation in ionic radius of the respective organic cations (a 1.4 Å difference between $r(TMA^+)$ and $r(MA^+)$). This observation suggests that the *d*-spacing of $(Org)_xV_8O_{20}{\cdot}nH_2O$ materials (Org = A, MA, and TMA) is directly

determined by the ion radius of the pre-intercalated organic cations. In contrast to $M_xV_2O_5{\cdot}nH_2O$ (M = Na, K, Rb, Mg, Al) materials, their *d*-spacing is predominantly influenced by the hydrated ion radius.

Additionally, XRD patterns of $(Org)_xV_8O_{20}{\cdot}nH_2O$ reveal varying degrees of peak broadening, as indicated by the full width at half-maximum (FWHM) values of (001) peak. As detailed in

Table 6.2, the FWHM values for the three samples follow the trend: A-VOH (0.72°) > MA-VOH (0.51°) > TMA-VOH (0.48°), suggesting that their crystallite sizes exhibit the order: A-VOH < MA-VOH < TMA-VOH.

Table 6.2. Structure and chemical composition characterization of $(Org)_xV_8O_{20}{\cdot}nH_2O$ materials (Org = A, MA, and TMA).

Sample	*d*-spacing (XRD)	FWHM for (001) peak (XRD)	*x* in $(Org)_xV_8O_{20}{\cdot}nH_2O$ (EDS)	V^{4+}/V^{5+} (XPS)	*n* in $(Org)_xV_8O_{20}{\cdot}nH_2O$ (TG)	Chemical formula
A-VOH	10.6 Å	0.72°	0.8	14.5 %	1.7	$(NH_4)_{0.8}V_8O_{20}{\cdot}1.7H_2O$
MA-VOH	11.2 Å	0.51°	0.8	15.7 %	2.0	$(CH_3NH_3)_{0.8}V_8O_{20}{\cdot}2.0H_2O$
TMA-VOH	12.6 Å	0.48°	0.88	12.2 %	1.0	$((CH_3)_4N)_{0.88}V_8O_{20}{\cdot}1.0H_2O$

Figure 6.1b shows the SEM images of $(Org)_xV_8O_{20}{\cdot}nH_2O$ materials. All three samples exhibit uniform-sized spherical clusters with diameters of several micrometers. Compared to the inorganic $M_xV_2O_5{\cdot}nH_2O$ (M = Na, K, Rb, Mg, Al) materials discussed in Chapter 4, the organic cation-modified vanadium oxides exhibit a more uniform and symmetric structure. This morphological difference is possibly attributed to the reduced polarity of organic cations, which may influence the kinetics of nanostructure growth.

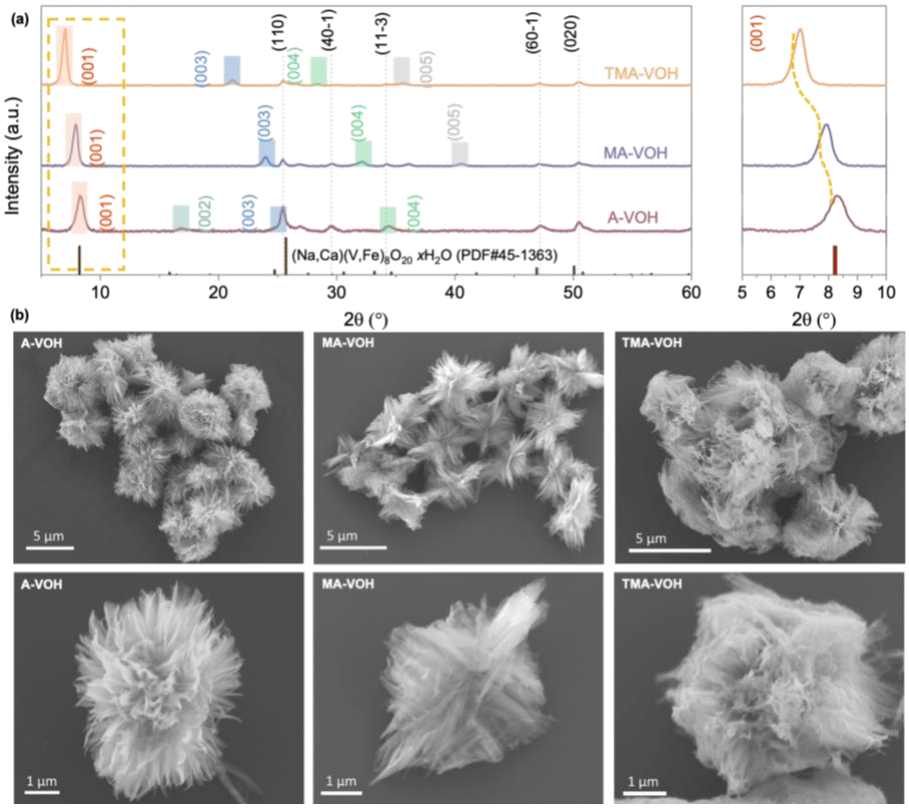

Figure 6.1. (a) XRD patterns and (b) SEM images of the synthesized $(Org)_xV_8O_{20}\cdot nH_2O$ powders (Org = A, MA, and TMA).

Further structural characterization was performed using TEM (Figure 6.2) to investigate the building blocks of spherical clusters in three samples. Notably, all samples reveal that each cluster is composed of ultrathin 2D nanobelts intergrown together, as reveled by the TEM images at higher magnification (Figure 6.2). In the case of A-VOH, numerous ultrathin nanobelts self-assemble into a 3D flower-like microstructure. While MA-VOH contains a relatively lower volume of VO_x nanobelts, which protrude from the central axis and stretch into two vertical directions, rather than forming a perfect spherical arrangement. TMA-VOH features radially oriented nanobelts similar to A-VOH, but with most nanobelt ends folded and covering the surface, creating a more compact, "destroyed" flower-like structure (Figure 6.1b and Figure 6.2). The destruction of nanobelts in TMA-VOH might be attributed to its strong interactions with the surrounding environment or high surface free energy.

During the initial nucleation stage, a layered structure forms with foreign species intercalated between oxide layers. SEM and TEM results demonstrate that all three samples crystallize as 2D ultrathin nanobelts, indicating similar effects of different organic species at this stage. In contrast, inorganic cation modified $M_xV_2O_5{\cdot}nH_2O$ (M = Na, K, Rb, Mg, Al) in Chapter 4 exhibit different building blocks such as nanoplatelets, nanofibers, or thick nanobelts.

After the initial nucleation stage, subsequent kinetic growth governs the final architecture, as the VO_x lamina self-organize into various configurations, forming distinct hierarchical structures. This process is presumed to be controlled by intermolecular forces from the un-intercalated free foreign species.[196] The selective adsorption of organic molecules onto specific crystal facets of growing nanoparticles can result in diverse hierarchical morphology.

In conclusion, compared to TMA-VOH, both A-VOH and MA-VOH exhibit relatively higher surface-to volume ratios and a larger number of absorption sites, which hold promise for enhanced electrolyte penetration into active sites and shorter diffusion pathways for Zn^{2+} ions. TEM-EDS mappings (Figure 6.2) confirm the even distribution of elements across the samples, with clear detection of N content indicating the presence of organic species. The atomic ratio of N:V calculated from TEM mapping is approximately 0.10 for A-VOH, 0.10 for MA-VOH, and 0.11 for TMA-VOH, corresponding to $(A)_{0.8}V_8O_{20}{\cdot}nH_2O$, $(MA)_{0.8}V_8O_{20}{\cdot}nH_2O$, and $(TMA)_{0.88}V_8O_{20}{\cdot}nH_2O$, respectively (

Table 6.2).

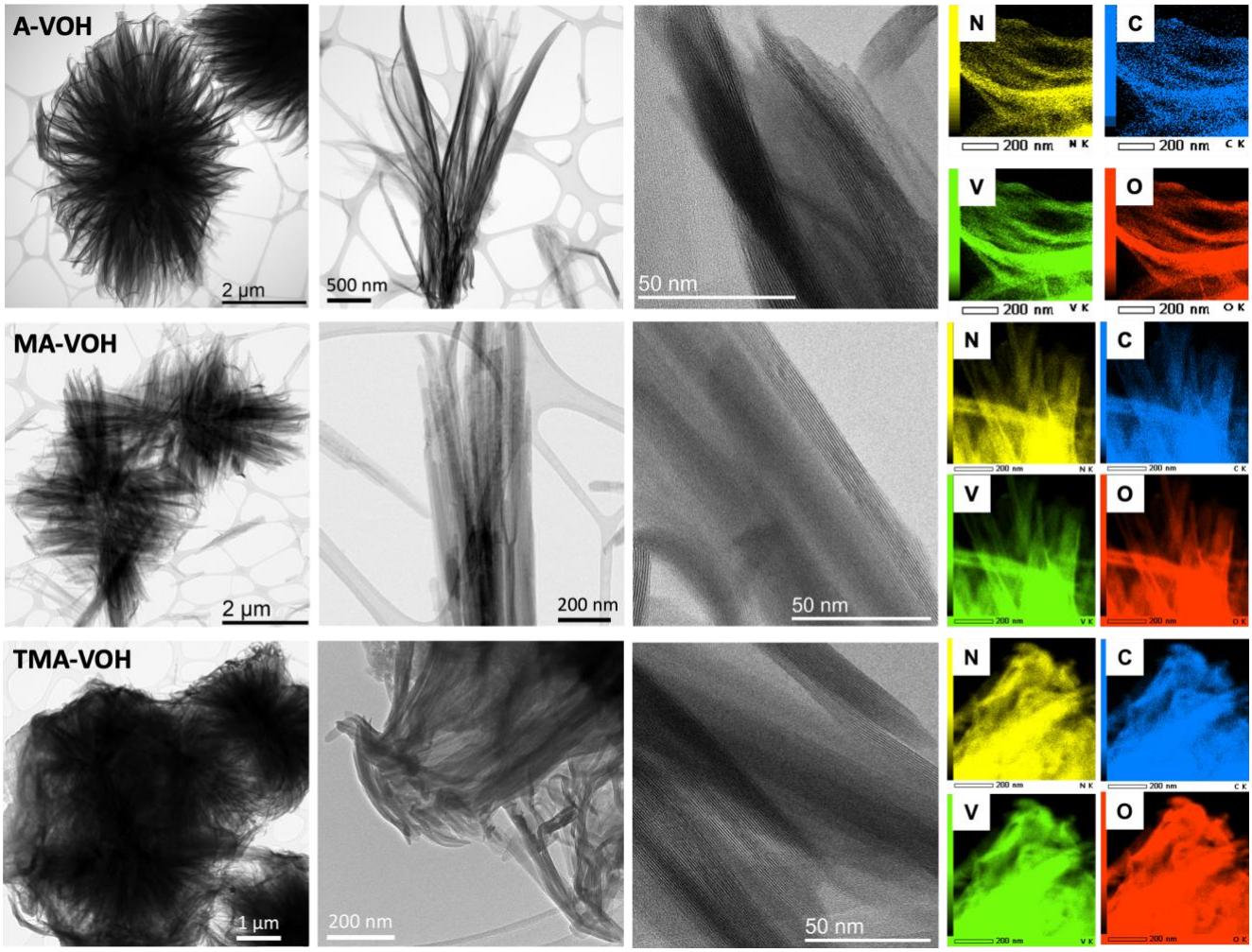

Figure 6.2. TEM images of the synthesized $(Org)_xV_8O_{20}\cdot nH_2O$ powders (Org = A, MA, and TMA).

Figure 6.3 presents the FTIR spectra of three samples, and the observed transmittance bands along with their corresponding assignments are provided in Table *6.3*. The spectra of these organic-inorganic nanocomposites are divided into two parts: spectral contributions from the pre-intercalated organic species and those specific to the vanadium oxides structures. In A-VOH, characteristic bands at 1400 cm^{-1} and 3158 cm^{-1} are attributed to the N−H bending and N−H stretching modes of the NH_4^+ species. For MA-VOH, intense bands arising from $–NH_3^+$ groups (at 3252 cm^{-1} and 1431 cm^{-1}) and $–CH_3$ groups (at 1465 cm^{-1} and 1497 cm^{-1}) are clearly distinguished, confirming the presence of methylammonium species.[197,198] As for TMPA-VOH, the strong peak at 945cm^{-1} corresponds to the C_4-N skeletal asymmetric stretching of the tetramethylammonium ($(CH_3)_4N^+$) cations, and the CH_3 asymmetric bending mode is observed at 1488 cm^{-1}.[199–201]

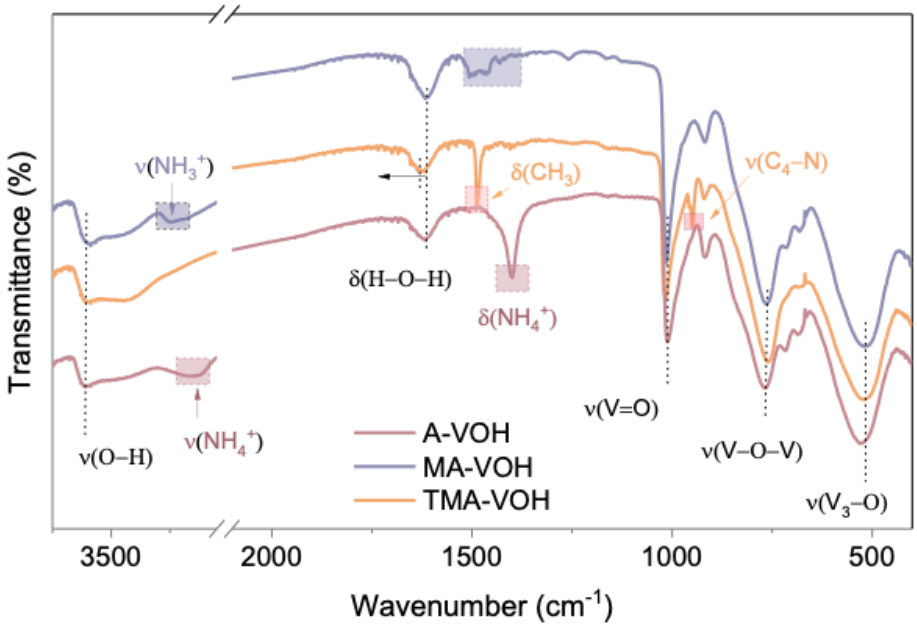

Figure 6.3. FTIR spectra of $(Org)_xV_8O_{20}\cdot nH_2O$ materials (Org = A, MA, and TMA).

In all three samples, the vibrational spectrum shows characteristic features of vanadium pentoxide near 1000 cm^{-1}, 750 cm^{-1}, and 500 cm^{-1}, corresponding to the stretching modes of V=O (vanadyl oxygen), V–O–V (doubly coordinated bridge oxygen), and V_3–O (triply coordinated chain oxygen), respectively.[202–205] The presence of these V_2O_5 characteristic modes indicates that the vanadium coordination is well preserved after the pre-intercalation of organic cations into the structure. The V=O peak exhibits a shoulder near 990 cm^{-1}, suggesting the presence of V^{4+}, a lowering of the V–O crystal symmetry, or the existence of V–O···N^+ interactions.[204]

Additionally, in all three samples, the observation of peaks near 1600 cm^{-1} and in the region of 3400–3600 cm^{-1} indicates a detectable presence of remining water molecules within the structure.[206] Specifically, the component centered at around 3600 cm^{-1} could be attributed to relatively free water molecules, while those near 3400 cm^{-1} are assigned to bound water molecules (likely involved in hydrogen bonding with oxygen atoms of the V−O structure or with other water molecules).[203]

Table 6.3. Assignments of the FTIR bands in A-VOH, MA-VOH, and TMA-VOH.[200,204,207,208]

Wavenumber/cm^{-1}			Assignment (vibration mode)
A-VOH	MA-VOH	TMA-VOH	
531 (s)	517 (s)	519 (s)	Asymmetric stretching of triply coordinated oxygen bonds O–$(V)_3$, $\nu_{as}(V_3O)$
716 (w)	714 (w)	712 (vw)	Hydrogen bonding with oxygen atoms of vanadyl group
768 (s)	764 (s)	760 (s)	Asymmetric stretching of doubly coordinated oxygen bonds V–O–V, ν_{as}(V–O–V)
918 (m)	918 (m)	920 (m)	V–OH_2 stretching
—	—	945 (s)	C_4–N asymmetric stretching, $\nu_{as}(C_4–N)$
989 (sh)	992 (sh)	995 (sh)	V=O stretching
1012 (s)	1014 (s)	1016 (s)	V=O stretching
—	1257 (m)	—	NH_3^+ Rocking, $\rho(NH_3^+)$
1400 (s)	1431 (w)	—	NH_3^+ symmetric bending, $\delta_s(NH_3^+)$
—	1465 (m)	1457 (w)	CH_3 symmetric bending, $\delta_s(CH_3)$
—	1497 (m)	1488 (s)	CH_3 asymmetric bending, $\delta_{as}(CH_3)$
1617 (s)	1617 (s)	1623 (s)	H–O–H bending
3158 (m)	3252 (m)	—	NH_3^+ asymmetric stretching
3609-3422 (s)	3587-3435 (s)	3596-3438 (s)	O–H stretching

Note: s, strong; w, weak; vw, very weak; m, middle; sh, shoulder.

The presence of NH_4^+ ions in A-VOH, $CH_3NH_3^+$ (MA^+) ions in MA-VOH, and $(CH_3)_4N^+$ (TMA^+) ions in TMA-VOH was also indicated by the detectable presence of N 1*s* signal in the XPS survey spectra (Figure 6.4a). Moreover, there is no trace of Cl signal detected in the survey spectra or the high-resolution Cl 1*s* spectra in all samples, indicating that only organic cations were pre-intercalated into the structure.

The high-resolution V $2p_{3/2}$ spectra (Figure 6.4b) reveal that all three samples exhibit a mixed valence state of V^{5+} and V^{4+}. The peak position and percentages of V^{5+} and V^{4+} components are listed in Table 6.4.[157,162,163] The binding energy of V^{5+} and V^{4+} peaks shows neglectable differences among three samples. This observation is consistent with that of alkali metal-modified VOH (NaVOH, KVOH, and RbVOH in Table

4.2). The atomic ratio of V^{4+}/V^{5+} follows the trend: MA-VOH (15.7%) > A-VOH (14.5%) > TMA-VOH (12.2%). Considering the polarity of three organic cations ($MA^+ < A^+ < TMA^+$), it can be reasonably suggested that the smaller polarity of pre-intercalated organic cations results in a higher amount of V^{4+} generated in the modified vanadium oxides. Comparing monovalent metal cations (Na^+, K^+ and Rb^+) in Chapter 4, the V^{4+} ratio follows the sequence: RbVOH (10.0%) < KVOH (10.6%) < NaVOH (13.1%), and the electronegativity difference between metal cations and the oxygen is Na–O (2.51) < K–O (2.62) = Rb–O (2.62). It can be inferred that the metal cation with a smaller M–O electronegativity difference induces a higher amount of V^{4+}, which aligns with the conclusion for organics cations.

The full width at half-maximum (FWHM) of the V $2p_{3/2}$ peak in MA-VOH (1.22 eV) is broader than that of A-VOH (1.21 eV) and TMA-VOH (1.18 eV), indicating that MA-VOH has a higher concentration of unpaired electrons in the *d*-band, again illustrating more V^{4+} ions upon the introduction of MA^+.[162,164,165] This higher proportion of V^{4+} species in MA-VOH can endow it with higher electronic conductivity and better electrochemical kinetics.

Table 6.4. Peak positions and valence states of vanadium determined from the fitted XPS spectra.

Samples	V^{5+}		V^{4+}		Average oxidation state
	Peak position	Ratio	Peak position	Ratio	
A-VOH	517.9 eV	87.3%	516.5 eV	12.7%	+4.87
MA-VOH	517.9 eV	86.4%	516.4 eV	13.6%	+4.86
TMA-VOH	517.9 eV	89.1%	516.5 eV	10.9%	+4.89

The O 1*s* spectra of A-VOH (Figure 6.4.b) show three peaks at 530.6 , 531.3, and 532.4 eV, which correspond to three oxygen-containing species: lattice oxygen coordinated with vanadium atoms (O–V), surface oxygen (e.g., V-bonded hydroxyl groups V–O–H), and oxygen from interlayer water molecules (H–O–H), respectively.[209,210] Similar phenomena are observed for the other two materials. The binding energy of all three O 1*s* peaks is the same for A-VOH and MA-VOH. However, for TMA-VOH, the peak corresponding

to water species shifts to a lower energy (532.1 eV compared to 532.4 eV), suggesting weaker bonding of interlayer water in TMA-VOH. This agrees with the earlier onset temperature of water loss observed for TMA-VOH in the TG results.

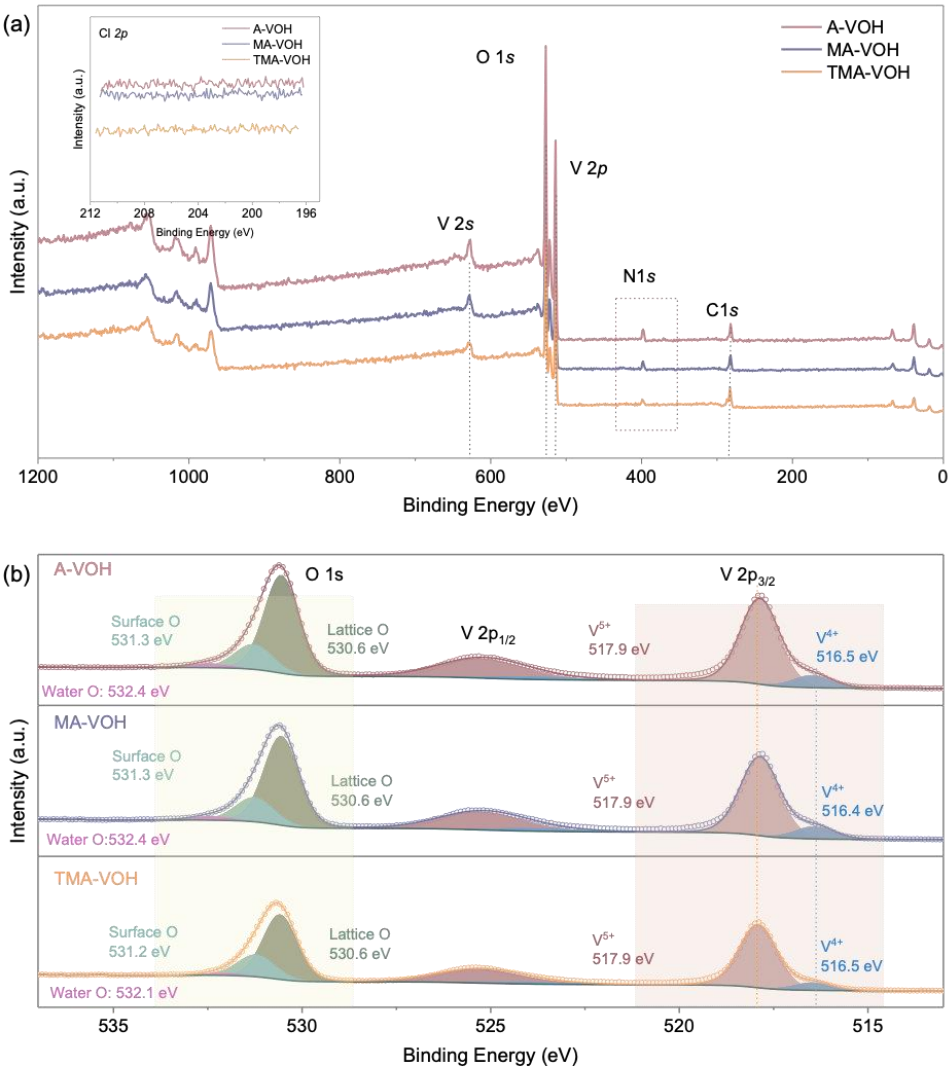

Figure 6.4. (a) XPS survey spectra, and (b) O 1*s* and V 2*p* spectra of $(Org)_xV_8O_{20}\cdot nH_2O$ materials.

In the high resolution N 1*s* spectra of all three samples (Figure 6.5a), in addition to the N–C bonds from the organic cations, another peak corresponding to N–O bonds is also observed, suggesting the formation of chemical bonds between the pre-intercalated organic cations and the VO_x matrix.[160,161] Compared to A-VOH and MA-VOH, the N–O peak in TMA-VOH shifts significantly toward a higher binding energy (0.7 eV),

indicating stronger N–O bonds in TMA-VOH. As shown in the C 1*s* spectra (Figure 6.5b), A-VOH exhibits three carbon components due to surface contamination: C–C/C–H bonding (285.0 eV), C–O bonding (286.4 eV), and O–C=O bonding (288.6 eV).[158,159] Similarly, MA-VOH and TMA-VOH also display three C 1*s* peaks as A-VOH, except the intensity of the peak at ~286 eV being much stronger (stronger than the C–C/C–H peak). This stronger peak can be attributed to the presence of C–N bonding adjacent to C–O.

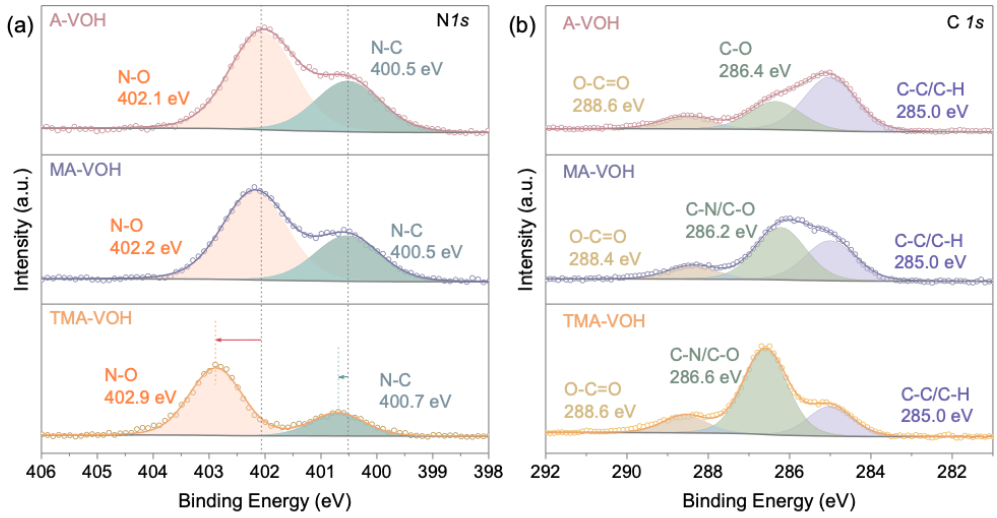

Figure 6.5. XPS spectra of $(Org)_xV_8O_{20}\cdot nH_2O$ materials. (a) N 1*s* spectra. (b) C 1*s* spectra.

Figure 6.6 presents the TG results of $(Org)_xV_8O_{20}\cdot nH_2O$ materials. The initial stage of weight loss up to 150 °C corresponds to the departure of weakly bonded water molecules, which can be recovered by adsorbing humidity from the air. The weight loss observed between 150–450 °C is attributed to the removal of tightly bonded water molecules between the V–O layers, along with the release of CO_2 and NO_2 gases from the combustion of pre-intercalated organic components.[156] The onset temperature for organics combustion varied depending on the intercalated species, with values of 336 °C for A^+, 342 °C for MA^+, and 365 °C for TMA^+. This trend is consistent with the stronger N–O bonds observed in TMA-VOH based on the XPS results. The total weight loss between 100 °C to 450 °C also varied with the intercalate: 5.9 % for A-VOH, 7.9 % for MA-VOH, and 10.2% for TMA-VOH. A summary of the hydration degree of $(Org)_xV_8O_{20}\cdot nH_2O$ materials is presented in Table 6.2. Based on the atomic ratio of N:V obtained from TEM-EDS data (listed in Table

6.2), the amount of interlayer organics and water can be estimated, allowing determination of chemical formula for the three compounds as follows: $(NH_4)_{0.8}V_8O_{20}\cdot 1.7H_2O$ for A-VOH, $(CH_3NH_3)_{0.8}V_8O_{20}\cdot 2.0H_2O$ for MA-VOH, and $((CH_3)_4N)_{0.88}V_8O_{20}\cdot 1.0H_2O$ for TMA-VOH.

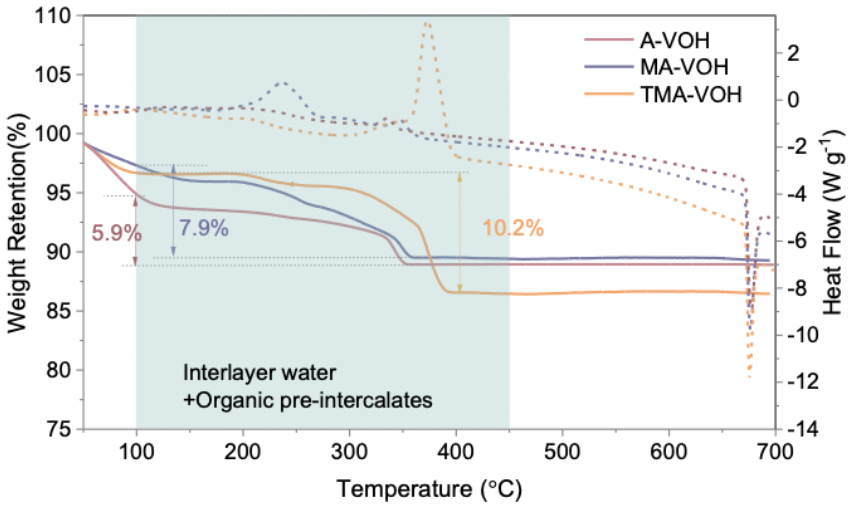

Figure 6.6. TG curves of $(Org)_xV_8O_{20}\cdot nH_2O$ materials (Org = A, MA, and TMA).

6.3 Electrochemical Performances

The 1st cycle GCD profiles of $(Org)_xV_8O_{20}\cdot nH_2O$ electrodes (Org = A, MA, and TMA) in ZIBs at 0.2 A g^{-1} are illustrated in Figure 6.7a. The initial discharge capacity for three samples is detailed in Table 6.5. Although there is a difference of 31 mA h g^{-1} between the lowest and highest initial capacities, the variations between three materials are not substantial. The sequence of initial capacity follows: MA-VOH > A-VOH > TMA-VOH. This observation suggests that the initial discharge capacity does not directly correlate with interlayer spacing, which is A-VOH (10.6 Å) < MA-VOH (11.2 Å) < TMA-VOH (12.6 Å). Rather, complex interplay of factors including ion radii, ion polarity, interlayer water, and V^{4+} content, may collectively influence the achieved capacity. Regarding the open circuit voltages (OCVs), a different sequence is observed: TMA-VOH (1.55 V) > MA-VOH (1.44 V) > A-VOH (1.40 V). The discrepancy in OCVs among samples was not specifically investigated in this study.

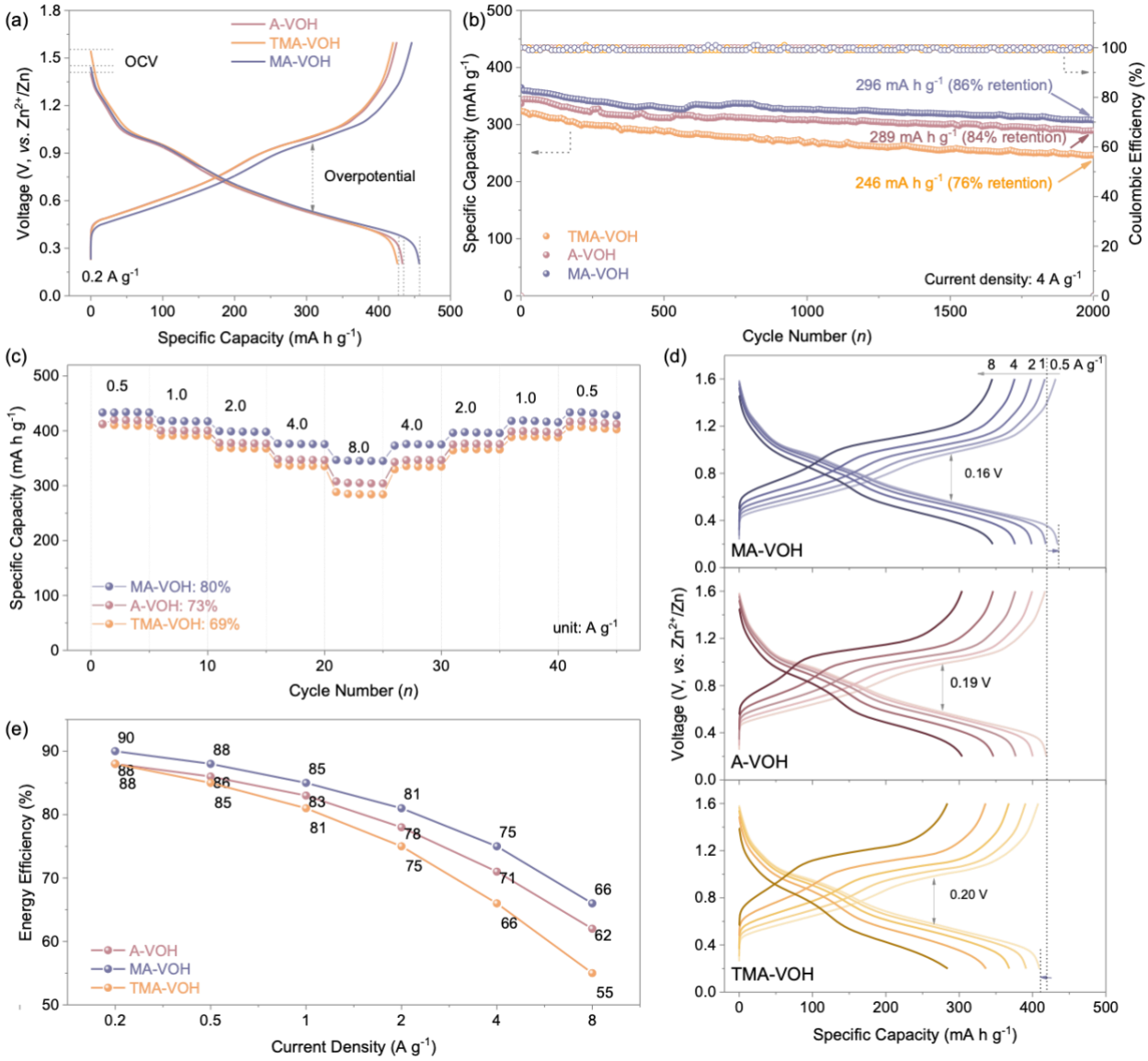

Figure 6.7. Electrochemical performance of Zn//A-VOH, Zn//MA-VOH, and Zn//TMA-VOH cells. (a) The 1st GCD cycle at 0.2 A g^{-1}. (b) Cycling performance at 4 A g^{-1}. (c) Rate performance and (d) the corresponding GCD profiles at various current densities. (e) Energy efficiency at various current densities.

Cycling stabilities are compared in Figure 6.7b. MA-VOH demonstrates the highest discharge capacity (346 mA h g^{-1}) and the highest capacity retention (85% after 2000 cycles), while TMA-VOH shows the lowest discharge capacity (324 mA h g^{-1}) and the lowest capacity retention (76% after 2000 cycles). The rate performance of Zn//$(Org)_xV_8O_{20}\cdot nH_2O$ cells is shown in Figure 6.7c, and the corresponding discharge capacities at different current densities are summarized in Table 6.5. When cycled at high current densities,

MA-VOH consistently demonstrates the largest capacities and the highest capacity retention (80% compared to the capacity at 0.5 A g^{-1}), highlighting its high tolerance to high currents, which is important for fast charging/discharging applications. In contrast, TMA-VOH shows the smallest capacities and the lowest capacity retentions (69 %).

The capacity decay of bilayered vanadium oxides largely stems from the loss of lamellar order due to strong electrostatic interactions between Zn^{2+} with the host lattice or the dissolution of vanadium ions. Both cycling stability and rate capability of $(Org)_xV_8O_{20}\cdot nH_2O$ follow the order of MA-VOH > A-VOH > TMA-VOH, which is contrary to the sequence of polarity for the three organic cations $MA^+ < A^+ < TMA^+$. These results support the hypothesis that the lower polarity of pre-inserted organic cations is expected to reduce electrostatic interactions between cycled ions with the host structure, thereby potentially enhancing the cycling stability and reversibility of the system.

Table 6.5. Discharge capacities of $Zn//(Org)_xV_8O_{20}\cdot nH_2O$ batteries (Org = A, MA, and TMA) at different current densities.

Samples	Specific Capacity (mA h g^{-1})					
	0.2 A g^{-1}	0.5 A g^{-1}	1.0 A g^{-1}	2.0 A g^{-1}	4.0 A g^{-1}	8.0 A g^{-1}
A	433	419	400	378	347	305
MA-VOH	457	434	418	399	376	346
TMA-VOH	426	410	391	368	337	284

The GCD curves at different current densities shown in Figure 6.7d highlight the differences in terms of capacity and overpotential among three samples. As illustrated by the mid-point voltage difference in Table 6.6, MA-VOH exhibits the smallest polarization at a given current density, while TMA-VOH shows the largest. Moreover, as the current rate increases, the advantages of MA-VOH becomes more pronounced, indicating that the intercalation/de-intercalation reversibility of the three samples follow the order: MA-VOH > A-VOH > TMA-VOH. Figure 6.7e presents the energy efficiency of the three samples. MA-VOH

consistently displays the highest energy efficiency across all current densities, while TMA-VOH demonstrates the lowest. Additionally, the energy efficiency of TMA-VOH decays most rapidly as the current density increases.

Table 6.6. Mid-point voltage difference between charging and discharging at different current densities for Zn//$(Org)_xV_8O_{20}\cdot nH_2O$ batteries (Org = A, MA, and TMA).

Samples	Overpotential				
	0.5 A g^{-1}	1.0 A g^{-1}	2.0 A g^{-1}	4.0 A g^{-1}	8.0 A g^{-1}
A	0.19 V	0.24 V	0.32 V	0.38 V	0.50 V
MA-VOH	0.16 V	0.20 V	0.27 V	0.35 V	0.45 V
TMA-VOH	0.20 V	0.27 V	0.35 V	0.46 V	0.61 V

In summary, MA-VOH exhibits the largest capacity, highest cycling stability, best rate capability, highest energy efficiency, and lowest overpotential among the three $(Org)_xV_8O_{20}\cdot nH_2O$ materials (Org = A, MA, and TMA). Conversely, TMA-VOH demonstrates the poorest performance across all these electrochemical metrics. A-VOH shows electrochemical stability similar to MA-VOH but kinetics closer to TMA-VOH. These results suggest that, rather than the radius of pre-intercalated ions or interlayer distance of the modified vanadium oxides, the polarity of the organic ions and amount of V^{4+} ions may be more influential factors determining the electrochemical performance.

6.4 Electrochemical Kinetics

From the CV curves at different scan rates (Figure 6.8a, d, and g), all three samples show a notable shift of reduction peaks to lower voltages and oxidation peaks to higher voltages as the scan rate increases from 0.1 to 1.2 mV s^{-1}, indicating amplified polarization effects.

The *b*-value analysis for the three samples is presented in Figure 6.8.b, e, and h. Notably, the *b* values of all redox peaks are higher than 0.7 for all three sample, indicating that charge storage in $(Org)_xV_8O_{20}\cdot nH_2O$ materials (Org = A, MA, and TMA) is primarily dominated by surface-controlled capacitive processes, rather than diffusion-limited redox processes. The smaller *b*-value of the O_2 peak compared to the O_1 peak suggests that the oxidation from V^{3+} to V^{4+} is the rate-limiting step during charging, consistent across all three samples. Comparing the rate-limiting step during charging (O_2), the *b* values follow the trend: MA-VOH > A-VOH > TMA-VOH, indicating better kinetics for MA-VOH and poorer kinetics for TMA-VOH.

For the discharging process, the rate-liming step differs among samples. For A-VOH and MA-VOH, the rate-liming step is the reduction reaction from V^{5+} to V^{4+} (R_1 peak), similar to the behavior of monovalent ion-stabilized VOH in Chapter 4. However, for TMA-VOH, the rate limiting step is the reduction from V^{4+} to V^{3+} (R_2 peak), resembling the behavior observed with doubly charged and triply charged ion-stabilized VOH. This distinction suggests that the pre-insertion of lower-polarized MA^+ ions has effects similar to pre-inserting singly charged ion-stabilized VOH (NaVOH, KVOH, and RbVOH). Conversely, for TMA-VOH, the effects are more aligned with those of MgVOH and AlVOH, where the insertion of more Zn^{2+} becomes challenging once all V^{5+} is reduced to V^{4+}. This phenomenon could be attributed to stronger electrostatic interactions between the intercalated Zn^{2+} ions and the more polarized TMA^+ ions.

The ratio of capacitive and diffusion-controlled contribution for all three samples is illustrated in Figure 6.8c, f, and i. MA-VOH demonstrates the highest capacitive contribution (e.g., 75 % at 0.1 mV s^{-1}), whereas A-VOH and TMA-VOH show similar capacitive contributions (69 % for A-VOH and 67 % for TMA-VOH), consistent with their similar rate capabilities (73% for A-VOH and 69 % for TMA-VOH). As the sweep rate increases from 0.1 to 1.2 mV s^{-1}, the diffusion contribution of MA-VOH decreases by only 16%, which is lower than the decrease observed for TMA-VOH (21%) and A-VOH (19%), further confirming the superior rate capability of MA-VOH.

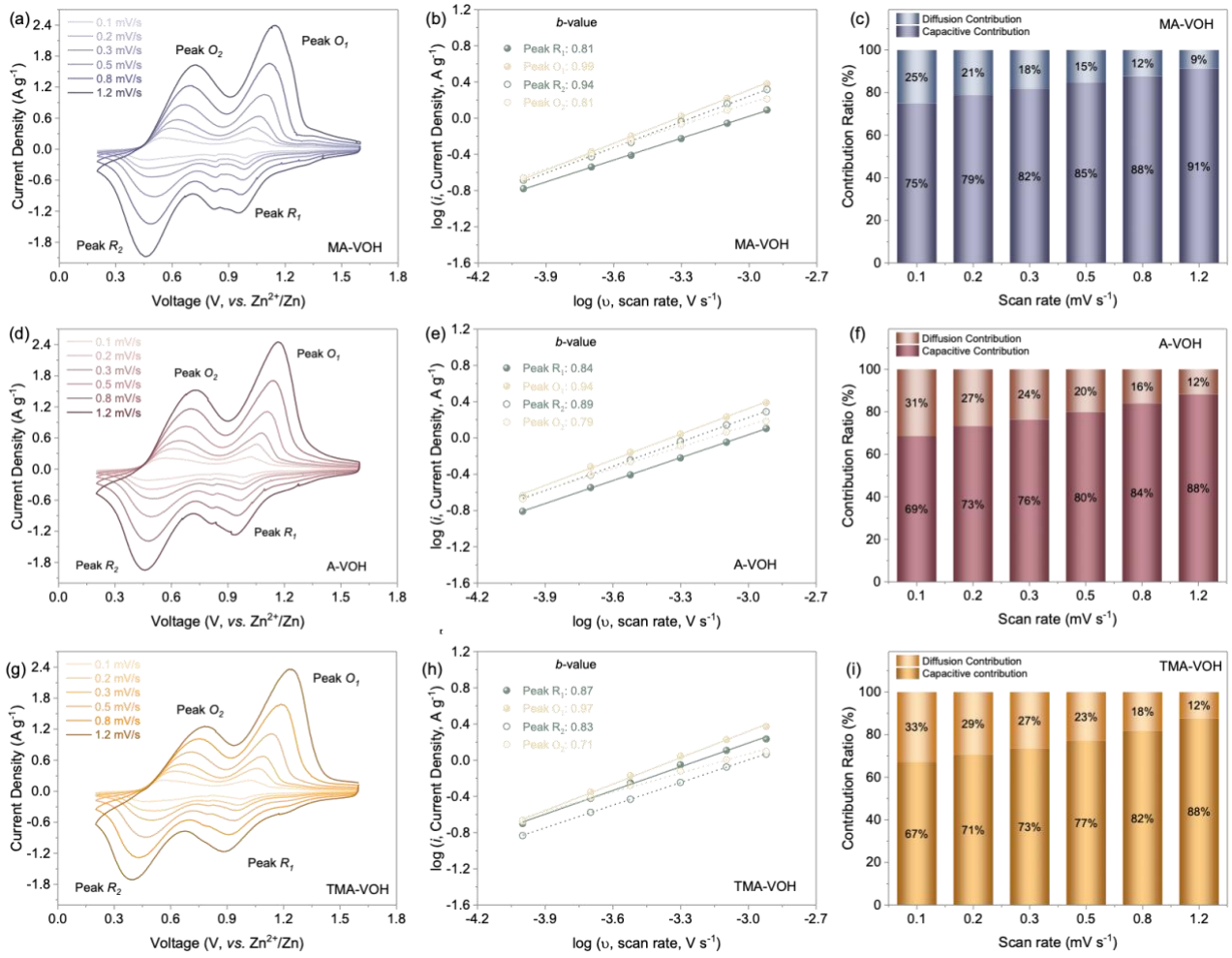

Figure 6.8. Electrochemical reaction kinetics analysis of Zn//(Org)$_x$V$_8$O$_{20}$·nH$_2$O batteries (Org = A, MA, and TMA). (a, d, g) CV curves at various scan rates. (b, e, h) The *log* (peak current) *vs. log* (scan rate) plot for each redox peak and their corresponding *b* values. and (c, f, i) Contribution of the diffusion-limited process and capacitive process.

Figure 6.9a and b show the CV curves at 0.1 mV s^{-1} and 1.2 mV s^{-1}, respectively. When cycled at a low scan rate of 0.1 mV s^{-1}, there is no significant difference in the shape of CV curves, peak positions, or enclosed areas among the three samples. This implies that all three samples demonstrate the same Zn^{2+} storage mechanism and offer similar active sites for Zn^{2+} intercalation. However, as the scan rate increases, the advantages of MA-VOH begin to emerge. At 1.2 mV s^{-1}, the area enclosed by the CV curve of MA-VOH is larger than that of A-VOH and TMA-VOH, and the shift of anodic and cathodic peaks is smaller, suggesting that MA-VOH has better electrochemical kinetics under higher scan rates.

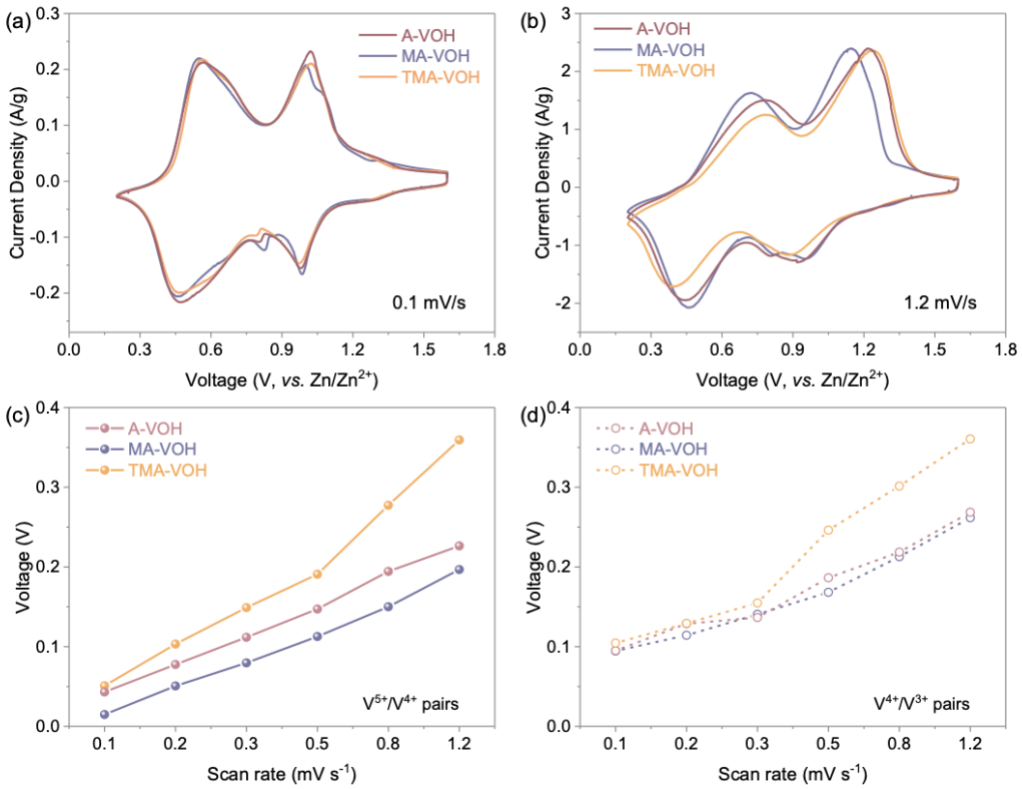

Figure 6.9. The 3rd cycle of CV curves at a scan rate of (a) 0.1 mV s^{-1} and (b) 1.2 mV s^{-1}. The voltage gaps between (a) V^{5+}/V^{4+} redox pairs, and (d) V^{5+}/V^{4+} redox pairs at different scan rates.

Peak separations between each redox pair at different scan rates are listed in Table 6.7 and plotted in Figure 6.9 c and d. At a low scan rate of 0.1 mV s^{-1}, considering V^{5+}/V^{4+} redox pairs (around ~ 1.0 V) as an example, MA-VOH exhibits a smaller difference between the corresponding cathodic and anodic peak voltages (0.01 V) compared to A-VOH (0.04 V) and TMA-VOH (0.05 V). This suggests higher reversibility of Zn^{2+} interaction and de-intercalation for MA-VOH, which aligns with the reduced overpotential observed in Figure 6.7d and supports the highest rate capability of MA-VOH. This advantage of MA-VOH becomes more prominent at higher rates. At 1.2 mV s^{-1}, the voltage gap of MA-VOH is 0.19 V, significantly smaller than that of TMA-VOH (0.36 V). Notably, the polarization of MA-VOH and A-VOH only shows a noticeable difference in the V^{5+}/V^{4+} pairs; the performance of V^{4+}/V^{3+} pairs is almost the same. The underlying reason for this phenomenon is still unclear at this point and requires further investigation.

Table 6.7. A comparison of peak positions and voltage gaps between redox pairs of V^{5+}/V^{4+} and V^{5+}/V^{4+} for three organic cation-pre-intercalated vanadium oxides at 0.1 mV s^{-1} and 1.2 mV s^{-1}.

Redox Pair	Sample	0.1 mV s^{-1}		1.2 mV s^{-1}	
		Peak Voltages	Peak Gap	Peak Voltages	Peak Gap
V^{5+}/V^{4+}	A-VOH	1.02/0.98 V	0.04 V	1.16/0.94 V	0.22 V
	MA-VOH	1.00/0.99 V	0.01 V	1.14/0.95 V	0.19 V
	TMA-VOH	1.02/0.97 V	0.05 V	1.24/0.88 V	0.36 V
V^{4+}/V^{3+}	A-VOH	0.57/0.47 V	0.10 V	0.72/0.45 V	0.27 V
	MA-VOH	0.55/0.46 V	0.09 V	0.72/0.46 V	0.26 V
	TMA-VOH	0.57/0.46 V	0.11 V	0.78/0.42 V	0.36 V

Figure *6.10*a presents the Nyquist plots for both fresh and cycled batteries, with charge transfer resistance (R_{ct}) and Zn^{2+} ion diffusion coefficient (D_{Zn}^{2+}) values listed in Table 6.8. All impedance spectra show a depressed semicircle at the medium-frequency region, indicating charge transfer processes, and a sloped line in the low-frequency region, corresponding to zinc diffusion. Initially, R_{ct} values follow the order: MA-VOH (14 Ω) < A-VOH (17 Ω) < TMA-VOH (32 Ω), indicating that MA-VOH has the highest electronic conductivity, likely attributed to its greatest density of unpaired electrons, as evidenced by the V^{4+}/V^{5+} ratio (MA-VOH 15.7 %, A-VOH 14.5 %, TMA-VOH 12.2 %). Before cycling, D_{Zn}^{2+} values are MA-VOH (1.9×10^{-11} cm^2 s^{-1}) > A-VOH (1.4×10^{-11} cm^2 s^{-1}) > TMA-VOH (1.3×10^{-11} cm^2 s^{-1}), highlighting more favorable ion transfer kinetics for MA-VOH due to the weakly polarized MA^+ ions. After cycling, all three samples show reduced charge transfer resistance and increased ion diffusion coefficient, a typical "activation process" in ZIBs, likely due to additional charge-transferring channels from residual Zn^{2+}. The lower R_{ct} and higher D_{Zn}^{2+} in MA-VOH compared to A-VOH and TMA-VOH indicate its superior electronic conductivity and ion diffusivity, contributing to its better electrochemical kinetics.

Benefiting from a higher proportion of low valance state V^{4+} and minimized interactions between Zn^{2+} ions and weakly polarized MA^+ species, MA-VOH exhibits superior electronic conductivity and ion diffusivity.

Consequently, MA-VOH demonstrates faster electrochemical kinetics, evidenced by its smaller voltage polarization and higher pseudocapacitive behavior. In contrast, TMA-VOH shows poorer performance than the control sample A-VOH, despite having the largest interlayer spacing. This suggests that the polarity of organic cations, rather than their ionic size, plays a critical role in electrochemical kinetics.

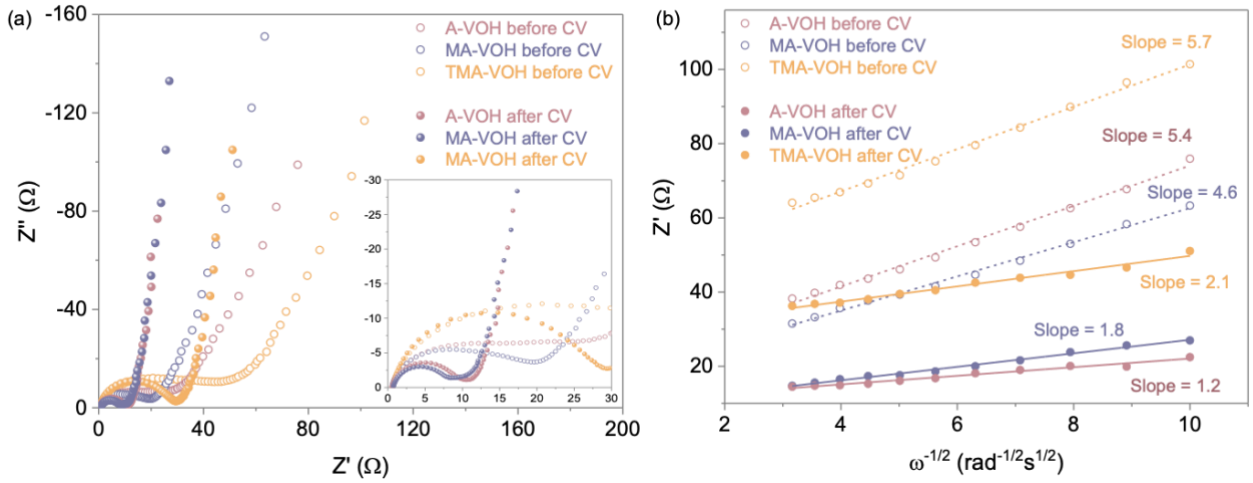

Figure 6.10. (a) Nyquist plots collected before and after CV cycles, and (b) Plot of Z' *vs.* $\omega^{-1/2}$ in the low-frequency region for Zn//(Org)$_x$V$_8$O$_{20}$·*n*H$_2$O batteries.

Table 6.8. Charge transfer resistance and Zn^{2+} diffusion coefficient of Zn//(Org)$_x$V$_8$O$_{20}$·*n*H$_2$O batteries.

		Charge Transfer Resistance, R_{ct}	Zn^{2+} Diffusion Coefficient, $D_{Zn^{2+}}$
A-VOH	Pristine	17 Ω	1.4×10^{-11} cm^2 s^{-1}
	After CV	9 Ω	2.8×10^{-10} cm^2 s^{-1}
MA-VOH	Pristine	14 Ω	1.9×10^{-11} cm^2 s^{-1}
	After CV	7 Ω	1.2×10^{-10} cm^2 s^{-1}
TMA-VOH	Pristine	32 Ω	1.3×10^{-11} cm^2 s^{-1}
	After CV	26 Ω	9.0×10^{-11} cm^2 s^{-1}

6.5 CONCLUSIONS

This chapter has demonstrated the effects of pre-intercalating two organic cations, methylammonium ($CH_3NH_3^+$) and tetramethylammonium ($N(CH_3)_4^+$) into the $V_2O_5 \cdot nH_2O$ system, using ammonium NH_4^+ pre-intercalated vanadium oxide as a reference. The interlayer spacing of $(Org)_xV_8O_{20} \cdot nH_2O$ materials (Org = A, MA, and TMA) is directly influenced by the ionic radius of organic cations, following the trend: A-VOH (10.6 Å) < MA-VOH (11.2 Å) < TMA-VOH (12.6 Å). This contrasts with the metal cation pre-intercalated vanadium oxide, where the interlayer distance is affected by the hydrated ion radius.

Electrochemical performance analysis in aqueous ZIBs reveals that MA-VOH exhibits superior performance in terms of capacity (457 mA h g^{-1} at 0.2 A g^{-1}), cycling stability (85% retention after 2000 cycles at 4 A g^{-1}), rate capability (80% retention at 8 A g^{-1} compared to capacity at 0.5 A g^{-1}), and energy efficiency (90% at 0.2 A g^{-1}), alongside the lowest overpotential (mid-point voltage difference of 0.16 V at 0.5 A g^{-1}). Conversely, TMA-VOH, despite its largest interlayer spacing, shows the poorest performance, likely due to stronger electrostatic interactions between higher polarized organic cations and cycled Zn^{2+} ions, leading to structural collapse and irreversible capacity loss. A-VOH displays electrochemical stability similar to MA-VOH but kinetics closer to TMA-VOH. Electrochemical kinetics analysis indicates that lower-polarized MA^+ ions facilitate easier Zn^{2+} ions insertion, similar to monovalent ion-stabilized VOH (NaVOH, KVOH, and RbVOH). In contrast, TMA-VOH aligns more with MgVOH and AlVOH, where Zn^{2+} insertion becomes more challenging after V^{5+} reduction to V^{4+}.

The trend in electrochemical stability and kinetics, MA-VOH > A-VOH > TMA-VOH, suggests that interlayer distance has minimal impacts on ion diffusion kinetics or host structure stability upon cycling. Interestingly, this trend correlates well with the cation polarity ($MA^+ < A^+ < TMA^+$), underscoring the significance of cation polarity and V^{4+} content over ion radius or interlayer distance in determining electrochemical behavior for $(Org)_xV_8O_{20} \cdot nH_2O$ materials.

Chapter 7. Conclusions and Future Directions

7.1 CONCLUSIONS

Aqueous zinc-ion batteries (ZIBs), with their air-stable zinc metal anodes and nonflammable water-based electrolytes, have emerged as promising candidates for grid-scale stationary energy storage. However, to realize practical application, further optimization of current ZIB systems is still needed, particularly in developing stable cathode materials. This dissertation explored a chemical pre-intercalation approach to enhance the properties of hydrated vanadium oxides ($V_2O_5 \cdot nH_2O$, VOH) for application as cathode materials in aqueous ZIBs. The work was organized around four main aims:

(1) Metal ion pre-intercalation study: using Na^+ as an example, investigated the feasibility of pre-intercalating metal cations into $V_2O_5 \cdot nH_2O$, and its effects on the structural properties and energy storage capabilities of VOH in aqueous ZIBs.

(2) Comparative study of various metal ions: examined a series of δ-$M_xV_2O_5 \cdot nH_2O$ (M = Na, K, Rb, Mg, Al) materials, established correlations between the properties of metal cations (e.g., size, charge, electronegativity), the structure of δ-$M_xV_2O_5 \cdot nH_2O$ (morphology, interlayer spacing, structural water, V^{4+} amount), and their electrochemical performance (capacity, stability, kinetics).

(3) Organic cation pre-intercalation study: explored the pre-intercalation of large and weakly polarized trimethylphenylammonium cations ($TMPA^+$) to harness the benefits of both ionic and molecular pre-intercalation.

(4) Comparative study of different organic cations: compared the pre-intercalation of $CH_3NH_3^+$ and $N(CH_3)_4^+$ cations with NH_4^+ pre-intercalated vanadium oxides, analyzed how properties of organic cations (size or polarity) affect their pre-intercalation effects, correlated the effects of organic cation-pre-intercalation with metal cation-pre-intercalation.

The main conclusions of these studies are summarized below:

(1) Metal cations can be favorably pre-intercalated into the VOH structure, replacing hydrogen bonded water (H_3O^+) between bilayers, modifying interlayer distance, and inducing more V^{4+} formation. Additional bridging bonds formed between pre-intercalated metal ions and the V–O lattice help to stabilize the framework more effectively than weak Van der Walls interactions in VOH. The increased amount of V^{4+} facilitates electron hopping between V^{4+} and V^{5+}, enhancing electronic conductivity. Partial replacement of interlayer water alleviates interactions between cycled Zn^{2+} ions and the host, ensuring faster and deeper Zn^{2+} ion insertion. These factors, together, effectively enhance the stability and kinetics of Zn^{2+} ion storage in the metal-cation modified VOH.

(2) The interlayer spacing of metal cation pre-intercalated δ-$M_xV_2O_5{\cdot}nH_2O$ materials (M = Na, K, Rb, Mg, Al) is determined by interlayer water content/hydration number, which increases with the hydrated ion radius but decreases with the electronegatively of preintercalated metal ions. There is no direct correlation between interlayer spacing of δ-$M_xV_2O_5{\cdot}nH_2O$ and its cyclic stability or rate capability, suggesting that interlayer spacing is not a key determinant of ion diffusion kinetics and host structure stability once it is sufficiently large for Zn ions. Singly charged ion-stabilized VOH (Na^+, K^+, and Rb^+), though has smaller interlayer spacing, exhibits better electrochemical kinetics than doubly charged

Mg^{2+}- and triply charged Al^{3+}-stabilized VOH, allowing for easier and deeper Zn^{2+} insertion due to their weaker electrostatic interactions with Zn^{2+} ions.

(3) Large organic cations can be pre-intercalated into VOH using the same synthesis methods as for inorganic cations. Incorporation of weakly polarized $TMPA^+$ cations induces a significant interlayer distance expansion, the extrusion of interlayer water, and a substantial increase in V^{4+} content. These modifications, synergistically, contribute to a largely reduced electrostatic interactions between Zn^{2+} and the V–O lattice, enhancing structural stability and reaction kinetics during cycling.

(4) Unlike metal cation pre-intercalated vanadium oxides, where interlayer distance is influenced by hydrated ion radius, the interlayer spacing of $(Org)_xV_8O_{20}\cdot nH_2O$ materials (Org = A, MA, and TMA) is directly influenced by the ionic radius of organic cations. The electrochemical stability and reaction kinetics of $(Org)_xV_8O_{20}\cdot nH_2O$ are mainly affected by the polarity of organic cations rather than their radius or interlayer distance. Lower-polarized MA^+ ions facilitate easier Zn^{2+} ion insertion, similar to singly charged ion-stabilized VOH, whereas higher-polarized TMA^+-stabilized VOH aligns more with doubly charged and triply charged ion-stabilized VOH.

7.2 Future Directions

This dissertation provides a solid foundation for further research and optimization of aqueous ZIBs using pre-intercalated vanadium oxides. Future work could focus on several key areas:

(1) In-depth mechanism studies: conduct *in-situ* and *ex-situ* characterization studies to gain deeper insights into the structural changes during cycling; investigate the ion diffusion pathways and the role of interlayer water in facilitating or hindering ion transport; explore the relationship between pre-intercalated species and the open circuit voltage using both experimental analysis and theoretical computations to clarify the observed tuning of open circuit voltage from 1.2-1.6 V with different pre-intercalated species.

(2) Optimization of chemical pre-intercalation methods: explore alternative synthesis routes to optimize the pre-intercalation effects; investigate the effects of varying synthesis parameters (temperature, time, or precursor concentration) on the structure and electrochemical properties of the materials.

(3) Towards practical applications: scale up the synthesis of pre-intercalated vanadium oxides and fabricate larger-scale ZIB prototypes to evaluate their performance under practical conditions; assess the long-term cycling stability of the aqueous ZIBs under various operational conditions.

(4) Expand beyond vanadium oxides and aqueous ZIBs: expand the established pre-intercalation strategy to other materials, such as manganese oxides, dichalcogenides, or MXenes; investigate the compatibility of pre-intercalated vanadium oxides with other battery systems, such as sodium ion batteries or lithium-ion batteries.

BIBLIOGRAPHY

1. Larcher, D., and Tarascon, J. M. Towards greener and more sustainable batteries for electrical energy storage. *Nat. Chem.* **7**, 19-29 (2015).
2. Hosenuzzaman, M., Rahim, N.A., Selvaraj, J., Hasanuzzaman, M., Malek, A.B.M.A., and Nahar, A. Global prospects, progress, policies, and environmental impact of solar photovoltaic power generation. *Renew. Sustain. Energy Rev.* **41**, 284–297 (2015).
3. Tang, W., Zhu, Y., Hou, Y., Liu, L., Wu, Y., Loh, K.P., Zhang, H., and Zhu, K. Aqueous rechargeable lithium batteries as an energy storage system of superfast charging. *Energy Environ. Sci.* **6**, 2093–2104 (2013).
4. Manthiram, A. An Outlook on Lithium Ion Battery Technology. *ACS Cent. Sci.* **3**, 1063–1069 (2017).
5. Di Lecce, D., Verrelli, R., and Hassoun, J. Lithium-ion batteries for sustainable energy storage: recent advances towards new cell configurations. *Green Chem.* **19**, 3442–3467 (2017).
6. Cheng, X., Zhang, R., Zhao, C., and Zhang, Q. Toward Safe Lithium Metal Anode in Rechargeable Batteries: A Review. *Chem. Rev.* **117**, 10403–10473 (2017).
7. Liu, B., Jia, Y., Li, J., Yin, S., Yuan, C., Hu, Z., Wang, L., Li, Y., and Xu, J. Safety issues caused by internal short circuits in lithium-ion batteries. *J. Mater. Chem. A.* **6**, 21475–21484 (2018).
8. Xu, K. Electrolytes and Interphases in Li-Ion Batteries and Beyond. *Chem. Rev.* **114**, 11503–11618 (2014).
9. Liu, C., Yuan, J., Masse, R., Jia, X., Bi, W., Neale, Z., Shen, T., Xu, M., Tian, M., Zheng, J., Tian, J., and Cao, G. Interphases, Interfaces, and Surfaces of Active Materials in Rechargeable Batteries and Perovskite Solar Cells. *Adv. Mater.* **33**, 1905245 (2021).
10. Kim, H., Hong, J., Park, K., Kim, H., Kim, S., and Kang, K. Aqueous Rechargeable Li and Na Ion Batteries. *Chem. Rev.* **114**, 11788–11827 (2014).

11. Wang, Y., Fu, X., Zheng, M., Zhong, W., and Cao, G. Strategies for Building Robust Traffic Networks in Advanced Energy Storage Devices: A Focus on Composite Electrodes. *Adv. Mater.* **31**, 1804204 (2019).
12. Cho, Y.G., Hwang, C., Cheong, D.S., Kim, Y.S., and Song, H.K. Gel/Solid Polymer Electrolytes Characterized by In Situ Gelation or Polymerization for Electrochemical Energy Systems. *Adv. Mater.* **31**, 1804909 (2019).
13. Gao, Z., Sun, H., Fu, L., Ye, F., Zhang, Y., Luo, W., and Huang, Y. Promises, Challenges, and Recent Progress of Inorganic Solid-State Electrolytes for All-Solid-State Lithium Batteries. *Adv. Mater.* **30**, 1705702 (2018).
14. Osada, I., de Vries, H., Scrosati, B., and Passerini, S. Ionic-Liquid-Based Polymer Electrolytes for Battery Applications. *Angew. Chem. Int. Ed.* **55**, 500–513 (2016).
15. Eshetu, G. G., Mecerreyes, D., Forsyth, M., Zhang, H., and Armand, M. Polymeric ionic liquids for lithium-based rechargeable batteries. *Mol. Syst. Des. Eng.* **4**, 294–309 (2019).
16. Gao, Y., Yan, Z., Gray, J.L., He, X., Wang, D., Chen, T., Huang, Q., Li, Y.C., Wang, H., Kim, S.H., Mallouk, T.E., and Wang, D. Polymer–inorganic solid–electrolyte interphase for stable lithium metal batteries under lean electrolyte conditions. *Nat. Mater.* **18**, 384–389 (2019).
17. Jiao, S., Ren, X., Cao, R., Engelhard, M.H., Liu, Y., Hu, D., Mei, D., Zheng, J., Zhao, W. *et al.* Stable cycling of high-voltage lithium metal batteries in ether electrolytes. *Nat. Energy* **3**, 739–746 (2018).
18. Wu, F., Kim, G.T., Kuenzel, M., Zhang, H., Asenbauer, J., Geiger, D., Kaiser, U., and Passerini, S. Elucidating the Effect of Iron Doping on the Electrochemical Performance of Cobalt-Free Lithium-Rich Layered Cathode Materials. *Adv. Energy Mater.* **9**, 1902445 (2019).
19. Kubota, K., and Komaba, S. Review—Practical Issues and Future Perspective for Na-Ion Batteries. *J. Electrochem. Soc.* **162**, A2538–A2550 (2015).
20. Yabuuchi, N., Kubota, K., Dahbi, M., and Komaba, S. Research development on sodium-ion batteries. *Chem. Rev.* **114**, 23, 11636–11682 (2014).
21. Hwang, J. Y., Myung, S. T., and Sun, Y. K. Sodium-ion batteries: Present and future. *Chem. Soc. Rev.* **46**, 3529–3614 (2017).

22. Kim, H., Kim, J. C., Bianchini, M., Seo, D.H., Rodriguez-Garcia, J., and Ceder, G. Recent Progress and Perspective in Electrode Materials for K-Ion Batteries. *Adv. Energy Mater.* **8**, 1702384 (2018).
23. Chong, S., Wu, Y., Guo, S., Liu, Y., and Cao, G. Potassium nickel hexacyanoferrate as cathode for high voltage and ultralong life potassium-ion batteries. *Energy Storage Mater.* **22**, 120–127 (2019).
24. Chen, C., Yang, Y., Tang, X., Qiu, R., Wang, S., Cao, G., and Zhang, M. Graphene-Encapsulated FeS_2 in Carbon Fibers as High Reversible Anodes for Na^+/K^+ Batteries in a Wide Temperature Range. *Small* **15**, 1804740 (2019).
25. Li, B., Masse, R., Liu, C., Hu, Y., Li, W., Zhang, G., and Cao, G. Kinetic surface control for improved magnesium-electrolyte interfaces for magnesium ion batteries. *Energy Storage Mater.* **22**, 96–104 (2019).
26. Aurbach, D., Lu, Z., Schechter, A., Gofer, Y., Gizbar, H., Turgeman, R., Cohen, Y., Moshkovich, M., and Levi, E. Prototype systems for rechargeable magnesium batteries. *Nature* **407**, 724–727 (2000).
27. Mao, M., Gao, T., Hou, S., and Wang, C. A critical review of cathodes for rechargeable Mg batteries. *Chem. Soc. Rev.* **47**, 8804–8841 (2018).
28. Kim, H., Hong, J., Park, K., Kim, H., Kim, S., and Kang, K. Aqueous rechargeable Li and Na ion batteries. *Chem. Rev.* **114**, 23, 11788–11827 (2014).
29. Xing, Z., Wang, S., Yu, A., and Chen, Z. Aqueous intercalation-type electrode materials for grid-level energy storage: Beyond the limits of lithium and sodium. *Nano Energy* **50**, 229–244 (2018).
30. Xia, C., Guo, J., Lei, Y., Liang, H., Zhao, C., and Alshareef, H.N. Rechargeable Aqueous Zinc-Ion Battery Based on Porous Framework Zinc Pyrovanadate Intercalation Cathode. *Adv. Mater.* **30**, 1705580 (2018).
31. Liu, J., Xu, C., Chen, Z., Ni, S., and Shen, Z. X. Progress in aqueous rechargeable batteries. *Green Energy Environ.* **3**, 20–41 (2018).
32. Bin, D., Wang, F., Tamirat, A. G., Suo, L., Wang, Y., Wang, C., and Xia, Y. Progress in Aqueous Rechargeable Sodium-Ion Batteries. *Adv. Energy Mater.* **8**, 1703008 (2018).
33. Jiang, L., Lu, Y., Zhao, C., Liu, L., Zhang, J., Zhang, Q., Shen, X., *et al.* Building aqueous K-ion batteries for energy storage. *Nat. Energy* **4**, 495–503 (2019).

34. Jia, X., Liu, C., Neale, Z. G., Yang, J., and Cao, G. Active Materials for Aqueous Zinc Ion Batteries: Synthesis, Crystal Structure, Morphology, and Electrochemistry. *Chem. Rev.* **120**, 7795–7866 (2020).
35. Huang, J., Guo, Z., Ma, Y., Bin, D., Wang, Y., and Xia, Y. Recent Progress of Rechargeable Batteries Using Mild Aqueous Electrolytes. *Small Methods* **3**, 1800272 (2019).
36. Wang, F., Fan, X., Gao, T., Sun, W., Ma, Z., Yang, C., Han, F., Xu, K., and Wang, C. High-Voltage Aqueous Magnesium Ion Batteries. *ACS Cent. Sci.* **3**, 1121–1128 (2017).
37. Yuan, D., Zhao, J., Manalastas, W., Kumar, S., and Srinivasan, M. Emerging rechargeable aqueous aluminum ion battery: Status, challenges, and outlooks. *Nano Mater. Sci.* **2**, 248-263 (2020).
38. Konarov, A., Voronina, N., Jo, J. H., Bakenov, Z., Sun, Y.K. and Myung, S.T. Present and Future Perspective on Electrode Materials for Rechargeable Zinc-Ion Batteries. *ACS Energy Lett.* **3**, 2620–2640 (2018).
39. Goodenough, J. B., and Kim, Y. Challenges for Rechargeable Li Batteries. *Chem. Mater.* **22**, 587–603 (2010).
40. Liu, C., Neale, Z. G., and Cao, G. Understanding electrochemical potentials of cathode materials in rechargeable batteries. *Mater. Today* **19**, 109–123 (2016).
41. Xu, K. Nonaqueous Liquid Electrolytes for Lithium-Based Rechargeable Batteries. *Chem. Rev.* **104**, 4303–4418 (2004).
42. Edström, K., Gustafsson, T., and Thomas, J. The Cathode-Electrolyte Interface in a Li-Ion Battery. in *Lithium-Ion Batteries: Solid-Electrolyte Interphase* 337–364 (Imperial College Press, London, 2004).
43. Liu, C., and Cao, G. Fundamentals of Rechargeable Batteries and Electrochemical Potentials of Electrode Materials. in *Nanomaterials for Energy Conversion and Storage* 397–451 (World Scientific, 2018).
44. Yadav, G.G., Wei, X., Huang, J., Gallaway, J.W., Turney, D.E., Nyce, M., Secor, J., and Banerjeea, S. A conversion-based highly energy dense Cu^{2+} intercalated Bi-birnessite/Zn alkaline battery. *J. Mater. Chem. A Mater.* **5**, 15845–15854 (2017).

45. Fu, J., Cano, Z.P., Park, M.G., Yu, A., Fowler, M., and Chen, Z. Electrically Rechargeable Zinc–Air Batteries: Progress, Challenges, and Perspectives. *Adv. Mater.* **29**, 1604685 (2017).
46. Fang, G., Zhou, J., Pan, A., and Liang, S. Recent Advances in Aqueous Zinc-Ion Batteries. *ACS Energy Lett.* **3**, 2480–2501 (2018).
47. Guduru, R. K., and Icaza, J. C. A Brief Review on Multivalent Intercalation Batteries with Aqueous Electrolytes. *Nanomaterials (Basel)* **6**, 41 (2016).
48. Kang, Z., Wu, C., Dong, L., Liu, W., Mou, J., Zhang, J., Chang, Z., Jiang, B., *et al.* 3D Porous Copper Skeleton Supported Zinc Anode toward High Capacity and Long Cycle Life Zinc Ion Batteries. *ACS Sustain. Chem. Eng.* **7**, 3364–3371 (2019).
49. Li, W., Wang, K., Cheng, S., and Jiang, K. A long-life aqueous Zn-ion battery based on $Na_3V_2(PO_4)_2F_3$ cathode. *Energy Storage Mater.* **15**, 14–21 (2018).
50. Chao, D., Zhu, C., Song, M., Liang, P., Zhang, X., Tiep, N.H., Zhao, H., Wang, J., Wang, R., *et al.* A High-Rate and Stable Quasi-Solid-State Zinc-Ion Battery with Novel 2D Layered Zinc Orthovanadate Array. *Adv. Mater.* **30**, 1803181 (2018).
51. Wang, X., Wang, F., Wang, L., Li, M., Wang, Y., Chen, B., Zhu, Y., *et al.* An Aqueous Rechargeable Zn//Co_3O_4 Battery with High Energy Density and Good Cycling Behavior. *Adv. Mater.* **28**, 4904–4911 (2016).
52. Li, H., Liu, Z., Liang, G., Huang, Y., Huang, Y., Zhu, M., Pei, Z., Xue, Q., Tang, Z., *et al.* Waterproof and Tailorable Elastic Rechargeable Yarn Zinc Ion Batteries by a Cross-Linked Polyacrylamide Electrolyte. *ACS Nano* **12**, 3140–3148 (2018).
53. Wang, L., Li, N., Wang, T., Yin, Y., Guo, Y., and Wang, C. Conductive graphite fiber as a stable host for zinc metal anodes. *Electrochim. Acta* **244**, 172–177 (2017).
54. Sun, K.E.K., Hoang, T.K.A, Doan, T.N.L., Yu, Y., Zhu, X., Tian, Y., and Chen, P. Suppression of Dendrite Formation and Corrosion on Zinc Anode of Secondary Aqueous Batteries. *ACS Appl. Mater. Interfaces* **9**, 9681–9687 (2017).
55. Sun, K.E.K., Hoang, T.K.A., Doan, T.N.L., Yu, Y., and Chen, P. Highly Sustainable Zinc Anodes for a Rechargeable Hybrid Aqueous Battery. *Chem. Eur. J.* **24**, 1667–1673 (2018).

56. Mainar, A.R., Colmenares, L.C., Grande, H.J., and Blázquez, J.A. Enhancing the Cycle Life of a Zinc–Air Battery by Means of Electrolyte Additives and Zinc Surface Protection. *Batteries* **4**, 46 (2018).
57. Drillet, J.F., Adam, M., Barg, S., Herter, A., Koch, D., Schmidt, V., and Wilhelm, M. Development of a Novel Zinc/Air Fuel Cell with a Zn Foam Anode, a PVA/KOH Membrane and a MnO_2/SiOC-Based Air Cathode. *ECS Trans.* **28**, 13–24 (2010).
58. Zhang, X. G. Fibrous zinc anodes for high power batteries. *J. Power Sources* **163**, 591–597 (2006).
59. Yang, C., and Lin, S. Improvement of high-rate capability of alkaline Zn–MnO_2 battery. *J. Power Sources* **112**, 174–183 (2002).
60. Xue, T., and Fan, H. From aqueous Zn-ion battery to Zn-MnO_2 flow battery: A brief story. *J. Energy Chem.* **54**, 194–201 (2021).
61. Kim, U.H., Kuo, L.Y., Kaghazchi, P., Yoon, C.S., and Sun, Y.K. Quaternary Layered Ni-Rich NCMA Cathode for Lithium-Ion Batteries. *ACS Energy Lett.* **4**, 576–582 (2019).
62. Han, B., Key, B., Lapidus, S.H., Garcia, J.C., Iddir, H., Vaughey, J.T., Dogan, F. From Coating to Dopant: How the Transition Metal Composition Affects Alumina Coatings on Ni-Rich Cathodes. *ACS Appl. Mater. Interfaces* **9**, 41291–41302 (2017).
63. Yang, Z., Li, Z., Huang, Y., Zhang, M., Liu, C., Zhang, D., and Cao, G. Artificial interface stabilized $LiNi_{0.80}Co_{0.15}Al_{0.05}O_2$@Polysiloxane cathode for stable cycling lithium-ion batteries. *J. Power Sources* **471**, 228480 (2020).
64. Qian, J., Wu, C., Cao, Y., Ma, Z., Huang, Y., Ai, X., and Yang, H. Prussian Blue Cathode Materials for Sodium-Ion Batteries and Other Ion Batteries. *Adv. Energy Mater.* **8**, 1702619 (2018).
65. Yang, D., Xu, J., Liao, X., He, Y., Liu, H., and Ma, Z. Structure optimization of Prussian blue analogue cathode materials for advanced sodium ion batteries. *Chem. Commun.* **50**, 13377–13380 (2014).
66. Shen, L., Wang, Z., and Chen, L. Prussian Blues as a Cathode Material for Lithium Ion Batteries. *Chem. Eur. J.* **20**, 12559–12562 (2014).
67. Yu, S.H., Shokouhimehr, M., Hyeon, T., and Sung, Y.E. Iron Hexacyanoferrate Nanoparticles as Cathode Materials for Lithium and Sodium Rechargeable Batteries. *ECS Electrochem. Lett.* **2**, A39–A41 (2013).

68. Kundu, D., Oberholzer, P., Glaros, C., Bouzid, A., Tervoort, E., Pasquarello, A., and Niederberger, M. Organic Cathode for Aqueous Zn-Ion Batteries: Taming a Unique Phase Evolution toward Stable Electrochemical Cycling. *Chem. Mater.* **30**, 3874–3881 (2018).

69. Zhao, Q., Huang, W., Luo, Z., Liu, L., Lu, Y., Li, Y., Li, L., Hu, J., Ma, H., and Chen, J. *et al.* High-capacity aqueous zinc batteries using sustainable quinone electrodes. *Sci. Adv.* **4**, eaao1761 (2018).

70. Hu, P., Yan, M., Zhu, T., Wang, X., Wei, X., Li, J., Zhou, L., Li, Z., Chen, L., and Mai, L. Zn/V_2O_5 Aqueous Hybrid-Ion Battery with High Voltage Platform and Long Cycle Life. *ACS Appl. Mater. Interfaces* **9**, 42717–42722 (2017).

71. Wan, F., and Niu, Z. Design Strategies for Vanadium-based Aqueous Zinc-Ion Batteries. *Angew. Chem. Int. Ed.* **58**, 16358–16367 (2019).

72. Tang, H., Peng, Z., Wu, L., Xiong, F., Pei, C., and An, Q. Vanadium-Based Cathode Materials for Rechargeable Multivalent Batteries: Challenges and Opportunities. *Electrochem. Energy Rev.* **1**, 169–199 (2018).

73. Ma, L., Li, N., Long, C., Dong, B., Fang, D., Liu, Z., Zhao, Y., Li, X., Fan, J., Chen, S., Zhang, S., and Zhi, C. Achieving Both High Voltage and High Capacity in Aqueous Zinc-Ion Battery for Record High Energy Density. *Adv. Funct. Mater.* **29**, 1906142 (2019).

74. Meng, J., Yang, Z., Chen, L., Qin, H., Cui, F., Jiang, Y., and Zeng, X. Energy storage performance of CuO as a cathode material for aqueous zinc ion battery. *Mater. Today Energy* **15**, 100370 (2020).

75. Fang, G., Liang, S., Chen, Z., Cui, P., Zheng, X., Pan, A., Lu, B., Lu, X., and Zhou, J. Simultaneous Cationic and Anionic Redox Reactions Mechanism Enabling High-Rate Long-Life Aqueous Zinc-Ion Battery. *Adv. Funct. Mater.* **29**, 1905267 (2019).

76. Wan, F., Zhang, Y., Zhang, L., Liu, D., Wang, C., Song, L., Niu, Z., and Chen, J. Reversible Oxygen Redox Chemistry in Aqueous Zinc-Ion Batteries. *Angew. Chem. Int. Ed.* **58**, 7062–7067 (2019).

77. Hu, P., Hu, P., Vu, T.D., Li, M., Wang, S., Ke, Y., Zeng, X., Mai, L., and Long, Y. Vanadium Oxide: Phase Diagrams, Structures, Synthesis, and Applications. *Chem. Rev.* **123**, 4353–4415 (2023).

78. Surnev, S., Ramsey, M. G., and Netzer, F. P. Vanadium oxide surface studies. *Prog. Surf. Sci.* **73**, 117–165 (2003).

79. Zavalij, P. Y., and Whittingham, M. S. Structural chemistry of vanadium oxides with open frameworks. *Acta Crystallogr. B* **55**, 627–663 (1999).

80. Lamsal, C., and Ravindra, N. M. Optical properties of vanadium oxides-an analysis. *J. Mater. Sci.* **48**, 6341–6351 (2013).

81. Zylbersztejn, A., and Mott, N. F. Metal-insulator transition in vanadium dioxide. *Phys. Rev. B* **11**, 4383–4395 (1975).

82. Le, T. K., Pham, P. V., Dong, C., Bahlawane, N., Vernardou, D., Mjejri, I., Rougier, A., and Kim, S. W. Recent advances in vanadium pentoxide (V_2O_5) towards related applications in chromogenics and beyond: fundamentals, progress, and perspectives. *J. Mater. Chem. C Mater.* **10**, 4019–4071 (2022).

83. Bystrom, A., Wilhelmi, K.A., and Brotzen, O. Vanadium pentoxide-a compound with five-coordinated vanadium atoms. *Acta. Chem. Scand.* **4**, 1119 (1950).

84. Haber, J., Witko, M., and Tokarz, R. Vanadium pentoxide I. Structures and properties. *Appl. Catal. A Gen.* **157**, 3–22 (1997).

85. Enjalbert, R., and Galy, J. A refinement of the structure of V_2O_5. *Acta Crystallogr. C* **42**, 1467–1469 (1986).

86. Wu, C., Feng, F., and Xie, Y. Design of vanadium oxide structures with controllable electrical properties for energy applications. *Chem. Soc. Rev.* **42**, 5157–5183 (2013).

87. Moretti, A., and Passerini, S. Bilayered Nanostructured $V_2O_5{\cdot}nH_2O$ for Metal Batteries. *Adv. Energy Mater.* **6**, 1600868 (2016).

88. Livage, J., Barboux, P., Badot, J. C., and Baffier, N. Ionic Properties of Vanadium Pentoxide Gels. *MRS Proceedings* **121**, 167 (1988).

89. Livage, J. Interface properties of vanadium pentoxide gels. *Mater. Res. Bull.* **26**, 1173–1180 (1991).

90. Kristoffersen, H. H., and Metiu, H. Structure of $V_2O_5{\cdot}nH_2O$ Xerogels. *J. Phys. Chem. C* **120**, 3986–3992 (2016).

91. Aldebert, P., Baffier, N., Gharbi, N., and Livage, J. Layered structure of vanadium pentoxide gels. *Mater. Res. Bull.* **16**, 669–676 (1981).

92. Zakharova, G. S., and Volkov, V. L. Intercalation compounds based on vanadium(V) oxide xerogel. *Russ. Chem. Rev.* **72**, 311–325 (2003).

93. Kristoffersen, H. H., and Metiu, H. Structure of $V_2O_5 \cdot nH_2O$ Xerogels. *J. Phys. Chem. C* **120**, 3986–3992 (2016).

94. Petkov, V., Trikalitis, P. N., Bozin, E. S., Billinge, S.J. L. Vogt, T., and Kanatzidis, M. G. Structure of $V_2O_5 \cdot nH_2O$ Xerogel Solved by the Atomic Pair Distribution Function Technique. *J. Am. Chem. Soc.* **124**, 10157–10162 (2002).

95. Livage, J. Vanadium pentoxide gels. *Chem. Mater.* **3**, 578–593 (1991).

96. Bailey, J. K., Pozarnsky, G. A., and Mecartney, M. L. The direct observation of structural development during vanadium pentoxide gelation. *J. Mater. Res.* **7**, 2530–2537 (1992).

97. Gharbi, N., Sanchez, C., Livage, J., Lemerle, J., Nejem, L., and Lefebvre, J. Mixed-valence poly(vanadic acid) gels. *Inorg. Chem.* **21**, 2758–2765 (1982).

98. Livage, J. Synthesis of polyoxovanadates via "chimie douce". *Coord. Chem. Rev.* **178–180**, 999–1018 (1998).

99. Livage, J. Hydrothermal Synthesis of Nanostructured Vanadium Oxides. *Materials* **3**, 4175–4195 (2010).

100. Fontenot, C. J., Wiench, J. W., Pruski, M., and Schrader, G. L. Vanadia Gel Synthesis via Peroxovanadate Precursors. 1. In Situ Laser Raman and 51^V NMR Characterization of the Gelation Process. *J. Phys. Chem. B* **104**, 11622–11631 (2000).

101. Alonso, B., and Livage, J. Synthesis of Vanadium Oxide Gels from Peroxovanadic Acid Solutions: A 51^V NMR Study. *J. Solid State Chem.* **148**, 16–19 (1999).

102. Livage, J., Baffier, N., Pereira-Ramos, J. P., and Davidson, P. Vanadium Pentoxide Gels from Liquid Crystals to Lithium Batteries. *MRS Proceedings* **369**, 179 (1994).

103. Livage, J. Optical and electrical properties of vanadium oxides synthesized from alkoxides. *Coord. Chem. Rev.* **190–192**, 391–403 (1999).

104. Liu, C., Tian, M., Wang, M., Zheng, J., Wang, S., Yan, M., Wang, Z., Yin, Z., Yang, J., and Cao, G. Catalyzing zinc-ion intercalation in hydrated vanadates for aqueous zinc-ion batteries. *J. Mater. Chem. A Mater.* **8**, 7713–7723 (2020).

105. Tian, M., Liu, C., Zheng, J., Jia, X., Jahrman, E. P., Seidler, G.T., Long, D., Atif, M., Alsalhi, M., and Cao, G. Structural engineering of hydrated vanadium oxide cathode by K^+ incorporation for high-capacity and long-cycling aqueous zinc ion batteries. *Energy Storage Mater.* **29**, 9–16 (2020).

106. Tepavcevic, S., Xiong, H., Stamenkovic, V. R., Zuo, X., Balasubramanian, M., Prakapenka, V. B., Johnson, C. S., and Rajh, T. Nanostructured bilayered vanadium oxide electrodes for rechargeable sodium-ion batteries. *ACS Nano* **6**, 530–538 (2012).

107. Liu, Z., Sun, H., Qin, L., Cao, X., Zhou, J., Pan, A., Fang, G., and Liang, S. Interlayer Doping in Layered Vanadium Oxides for Low-cost Energy Storage: Sodium-ion Batteries and Aqueous Zinc-ion Batteries. *ChemNanoMat* **6**, 1553–1566 (2020).

108. Yan, M., He, P., Chen, Y., Wang, S., Wei, Q., Zhao, K., Xu, X., *et al.* Water-Lubricated Intercalation in $V_2O_5{\cdot}nH_2O$ for High-Capacity and High-Rate Aqueous Rechargeable Zinc Batteries. *Adv. Mater.* **30**, (2018).

109. Zong, Q., Wu, Y., Liu, C., Wang, Q., Zhuang, Y., Wang, J., Tao, D., Zhang, Q., and Cao, G. Tailoring layered transition metal compounds for high-performance aqueous zinc-ion batteries. *Energy Storage Mater.* **52**, 250–283 (2022).

110. Wang, Q., Tang, S., Wang, Z., Wu, J., Bai, Y., Xiong, Y., Yang, P., Wang, Y., Tan, Y., Liu, W., Xiong, X., and Lei, Y. Electrolyte Tuned Robust Interface toward Fast-Charging Zn–Air Battery with Atomic Mo Site Catalyst. *Adv. Funct. Mater.* **33**, 2307390 (2023).

111. Li, B., Zhang, X., Wang, T., He, Z., Lu, B., Liang, S., and Zhou, J. Interfacial Engineering Strategy for High-Performance Zn Metal Anodes. *Nanomicro Lett.* **14**, 6 (2021).

112. Kundu, D., Vajargah, S. H., Wan, L., Adams, B., Prendergast, D., and Nazar L. F. Aqueous: Vs. nonaqueous Zn-ion batteries: Consequences of the desolvation penalty at the interface. *Energy Environ. Sci.* **11**, 881–892 (2018).

113. Jia, X., Tian, R., Liu, C., Zheng, J., Tian, M., and Cao, G. Stability and kinetics enhancement of hydrated vanadium oxide via sodium-ion pre-intercalation. *Mater. Today Energy* **28**, 101063 (2022).

114. Li, Y., Zhang, D., Huang, S., and Yang, H. Y. Guest-species-incorporation in manganese/vanadium-based oxides: Towards high performance aqueous zinc-ion batteries. *Nano Energy* **85**, 105969 (2021).

115. Liu, C., Neale, Z., Zheng, J., Jia, X., Huang, J., Yan, M., Tian, M., Wang, M., Yang, J., and Cao, G. Expanded hydrated vanadate for high-performance aqueous zinc-ion batteries. *Energy Environ. Sci.* **12**, 2273–2285 (2019).

116. Xing, L., Zhang, C., Li, M., Hu, P., Zhang, X., Dai, Y., Pan, X., Sun, W., Li, S., Xue, J., An, Q., and Mai, L. Revealing excess Al^{3+} preinsertion on altering diffusion paths of aluminum vanadate for zinc-ion batteries. *Energy Storage Mater.* **52**, 291–298 (2022).
117. Zhao, Q., Song, A., Ding, S., Qin, R., Cui, Y., Li, S., and Pan, F. Preintercalation Strategy in Manganese Oxides for Electrochemical Energy Storage: Review and Prospects. *Adv. Mater.* **32**, 2002450 (2020).
118. Ma, L., Li, N., Long, C., Dong, B., Fang, D., Liu, Z., Zhao, Y., Li, X., Fan, J., Chen, S., Zhang, S., and Zhi, C. Achieving Both High Voltage and High Capacity in Aqueous Zinc-Ion Battery for Record High Energy Density. *Adv. Funct. Mater.* **29**, 1906142 (2019).
119. Zhao, X., Mao, L., Cheng, Q., Liao, F., Yang, G., Lu, X., and Chen, L. Interlayer Engineering of Preintercalated Layered Oxides as Cathode for Emerging Multivalent Metal-ion Batteries: Zinc and Beyond. *Energy Storage Mater.* **38**, 397–437 (2021).
120. Liu, S., Zhu, H., Zhang, B., Li, G., Zhu, H., Ren, Y., Geng, H., Yang, Y., Liu, Q., and Li, C. C. Tuning the Kinetics of Zinc-Ion Insertion/Extraction in V_2O_5 by In Situ Polyaniline Intercalation Enables Improved Aqueous Zinc-Ion Storage Performance. *Adv. Mater.* **32**, 2001113 (2020).
121. Liu, J., Wang, J., Xu, C., Jiang, H., Li, C., Zhang, L., Lin, J., and Shen, Z. Advanced Energy Storage Devices: Basic Principles, Analytical Methods, and Rational Materials Design. *Adv. Sci.* **5**, 1700322 (2018).
122. Choi, W., Shin, H.C., Kim, J. M., Choi, J.Y., and Yoon, W.S. Modeling and Applications of Electrochemical Impedance Spectroscopy (EIS) for Lithium-ion Batteries. *J. Electrochem. Sci. Technol.* **11**, 1–13 (2020).
123. Shi, M., Chen, Z., and Sun, J. Determination of chloride diffusivity in concrete by AC impedance spectroscopy. *Cem. Concr. Res.* **29**, 1111–1115 (1999).
124. Weppner, W., and Huggins, R. A. Determination of the Kinetic Parameters of Mixed-Conducting Electrodes and Application to the System Li_3Sb. *J Electrochem. Soc.* **124**, 1569–1578 (1977).
125. Kemeny, M., Ondrejka, P., and Mikolasek, M. Comprehensive Degradation Analysis of NCA Li-Ion Batteries via Methods of Electrochemical Characterisation for Various Stress-Inducing Scenarios. *Batteries* **9**, (2023).

126. Liu, C., Neale, Z., Zheng, J., Jia, X., Huang, J., Yan, M., Tian, M., Wang, M., Yang, J., and Cao, G. Expanded hydrated vanadate for high-performance aqueous zinc-ion batteries. *Energy Environ. Sci.* **12**, 2273–2285 (2019).

127. Clites, M., and Pomerantseva, E. Bilayered vanadium oxides by chemical pre-intercalation of alkali and alkali-earth ions as battery electrodes. *Energy Storage Mater.* **11**, 30–37 (2018).

128. Lee, S.H., Cheong, H. M., Seong, M. J., Liu, P., Tracy, C.E, Mascarenhas, A., Pitts, J.R., Deb, S. K. Raman spectroscopic studies of amorphous vanadium oxide thin films. *Solid State Ion.* **165**, 111–116 (2003).

129. Sanchez, C., Livage, J., and Lucazeau, G. Infrared and Raman study of amorphous V2O5. *J. Raman Spectrosc.* **12**, 68–72 (1982).

130. Lee, J., Badie, S., Srimuk, P., Ridder, A., Shim, H., Choudhury, S., Nah, Y.C., and Presser, V. Electrodeposition of hydrated vanadium pentoxide on nanoporous carbon cloth for hybrid energy storage. *Sustain. Energy Fuels* **2**, 577–588 (2018).

131. Chen, W., Mai, L., Peng, J., Xu, Q., and Zhu, Q. Raman spectroscopic study of vanadium oxide nanotubes. *J. Solid State Chem.* **177**, 377–379 (2004).

132. Londoño-Calderón, C. L., Vargas-Hernández, C., and Jurado, J. F. Desorption influence of water on structural, electrical properties and molecular order of vanadium pentoxide xerogel films. *Rev. mex. fís.* **56**, 411–415 (2010).

133. Kristoffersen, H. H., and Metiu, H. Structure of $V_2O_5 \cdot nH_2O$ Xerogels. *J. Phys. Chem. C* **120**, 3986–3992 (2016).

134. Avansi Jr, W., Ribeiro, C., Leite, E. R., and Mastelaro, V. R. Vanadium Pentoxide Nanostructures: An Effective Control of Morphology and Crystal Structure in Hydrothermal Conditions. *Cryst. Growth Des.* **9**, 3626–3631 (2009).

135. Yao, T., Oka, Y., and Yamamoto, N. Layered structures of vanadium pentoxide gels. *Mater. Res. Bull.* **27**, 669–675 (1992).

136. Benayad, A., Martinez, H., Gies, A., Pecquenard, B., Levasseur, A., and Gonbeau, D. XPS investigations achieved on the first cycle of V_2O_5 thin films used in lithium microbatteries. *J. Electron Spectros. Relat. Phenomena.* **150**, 1–10 (2006).

137. Segall, M. D., Lindan, P. J. D., Probert, M. J., Pickard, C. J., Hasnip, P. J., Clark, S. J., and Payne, M. C. First-principles simulation: ideas, illustrations and the CASTEP code. *J. Phys. Condens. Matter.* **14**, 2717–2744 (2002).

138. Hohenberg, P., and Kohn, W. Inhomogeneous Electron Gas. *Phys. Rev.* **136**, B864–B871 (1964).

139. Perdew, J. P., Burke, K., and Ernzerhof, M. Generalized Gradient Approximation Made Simple. *Phys. Rev. Lett.* **77**, 3865–3868 (1996).

140. Dudarev, S. L., Botton, G. A., Savrasov, S. Y., Humphreys, C. J., and Sutton, A. P. Electron-energy-loss spectra and the structural stability of nickel oxide: An LSDA+U study. *Phys. Rev. B* **57**, 1505–1509 (1998).

141. Xiao, R., Xie, J., Luo, T., Huang, L., Zhou, Y., Yu, D., Chen, C., and Liu, Y. Phase Transformation and Diffusion Kinetics of V_2O_5 Electrode in Rechargeable Li and Mg Batteries: A First-Principle Study. *J. Phys. Chem. C* **122**, 1513–1521 (2018).

142. Grimme, S. Semiempirical GGA-type density functional constructed with a long-range dispersion correction. *J Comput Chem* **27**, 1787–1799 (2006).

143. Eftekhari, A. Energy efficiency: a critically important but neglected factor in battery research. *Sustain. Energy Fuels* **1**, 2053–2060 (2017).

144. Xia, C., Guo, J., Li, P., Zhang, X., and Alshareef, H. N. Highly Stable Aqueous Zinc-Ion Storage Using a Layered Calcium Vanadium Oxide Bronze Cathode. *Angew. Chem. Int. Ed.* **57**, 3943–3948 (2018).

145. Tang, B., Fang, G., Zhou, J., Wang, L., Lei, Y., Wang, C., Lin, T., Tang, Y., and Liang, S. Potassium vanadates with stable structure and fast ion diffusion channel as cathode for rechargeable aqueous zinc-ion batteries. *Nano Energy* **51**, 579–587 (2018).

146. Zhang, N., Jia, M., Dong, Y., Wang, Y., Xu, J., Liu, Y., Jiao, L., and Cheng, F. Hydrated Layered Vanadium Oxide as a Highly Reversible Cathode for Rechargeable Aqueous Zinc Batteries. *Adv. Funct. Mater.* **29**, 1807331 (2019).

147. He, P., Zhang, G., Liao, X., Yan, M., Xu, X., An, Q., Liu, J., and Mai, L. Sodium Ion Stabilized Vanadium Oxide Nanowire Cathode for High-Performance Zinc-Ion Batteries. *Adv. Energy Mater.* **8**, 1702463 (2018).

148. Sambandam, B., Soundharrajan, V., Kim, S., Alfaruqi, M. H., Jo, J., Kim, S., Mathew, V., Sun, Y., and Kim, J. Aqueous rechargeable Zn-ion batteries: an imperishable and high-

energy $Zn_2V_2O_7$ nanowire cathode through intercalation regulation. *J. Mater. Chem. A Mater.* **6**, 3850–3856 (2018).

149. Yang, X., and Rogach, A. L. Electrochemical Techniques in Battery Research: A Tutorial for Nonelectrochemists. *Adv. Energy Mater.* **9**, 1900747 (2019).
150. Buenaño, X., Canoira, L., Martin Sánchez, D., and Costafreda, J. Zeolitic tuffs for acid mine drainage (AMD) treatment in Ecuador: breakthrough curves for Mn^{2+}, Cd^{2+}, Cr^{3+}, Zn^{2+}, and Al^{3+}. *Environ. Sci. Pollut. Res.* **24**, 6794–6806 (2017).
151. Ashjian, H., Le, Q., Marler, D., Shim, J., and Wong, S. Naphthalene alkylation process. Preprint at (1991).
152. Ramos, S., Barnes, A. C., Neilson, G. W., and Capitan, M. J. Anomalous X-ray diffraction studies of hydration effects in concentrated aqueous electrolyte solutions. *Chem. Phys.* **258**, 171–180 (2000).
153. Manikandan, R., Raj, C. J., Rajesh, M., Kim, B. C., Park, S., and Yu, K. H. Vanadium Pentoxide with H_2O, K^+, and Na^+ Spacer between Layered Nanostructures for High-Performance Symmetric Electrochemical Capacitors. *Adv. Mater. Interfaces* **5**, 1800041 (2018).
154. Zanarini, S., Di Lupo, F., Bedini, A., Vankova, S., Garino, N., Francia, C., and Bodoardo, S. Three-colored electrochromic lithiated vanadium oxides: the role of surface superoxides in the electro-generation of the red state. *J. Mater. Chem C Mater.* **2**, 8854–8857 (2014).
155. Evans Jr., H. T., Post, J. E., Ross, D. R., and Nelen, J. A. The crystal structure and crystal chemistry of fernandinite and corvusite. *Can Mineral* **32**, 339–351 (1994).
156. Baffier, N., Znaidi, L., and Badot, J.C. Ionic hydration number in V_2O_5 intercalated xerogels $M(H_2O)V_2O_5$. *J. Chem. Soc., Faraday Trans.* **86**, 2623–2628 (1990).
157. Bondarenka, V., Grebinskij, S., Kaciulis, S., Mattogno, G., Mickevicius, S., Tvardauskas, H., Volkov, V., and Zakharova, G. XPS study of vanadium–yttrium hydrates. *J. Electron Spectros. Relat. Phenomena* **120**, 131–135 (2001).
158. Ameen, S., Akhtar, M. S., Kim, Y. S., and Shin, H. S. Synthesis and electrochemical impedance properties of CdS nanoparticles decorated polyaniline nanorods. *Chem. Eng. J.* **181–182**, 806–812 (2012).

159. Zhang, Y., Huang, R., Wang, X., Wang, Z., Song, B., Du, Y., Lu, Q., Chen, X., and Sun, J. Facile large-scale preparation of vanadium pentoxide-polypyrrole composite for aqueous zinc-ion batteries. *J. Alloys Compd.* **907**, 164434 (2022).

160. Tong, Y., Su, S., Li, X., Liang, B., Peng, J., Hou, J., and Luo, M. Synergistic iron ion and alkylammonium cation intercalated vanadium oxide cathode for highly efficient aqueous zinc ion battery. *J. Power Sources* **528**, 231226 (2022).

161. Wang, Q., Feng, Q., Lei, Y., Tang, S., Xu, L., Xiong, Y., Fang, G., Wang, Y., Yang, P., Liu, J., Liu, W., and Xiong, X. Quasi-solid-state Zn-air batteries with an atomically dispersed cobalt electrocatalyst and organohydrogel electrolyte. *Nat. Commun.* **13**, 3689 (2022).

162. Sawatzky, G. A., and Post, D. X-ray photoelectron and Auger spectroscopy study of some vanadium oxides. *Phys. Rev. B* **20**, 1546–1555 (1979).

163. Ureña-Begara, F., Crunteanu, A., and Raskin, J.P. Raman and XPS characterization of vanadium oxide thin films with temperature. *Appl. Surf. Sci.* **403**, 717–727 (2017).

164. Bondarenka, V. Valance of vanadium in hydrated compounds. *Lith. J. Phys.* **47**, 333–342 (2007).

165. Hryha, E., Rutqvist, E., and Nyborg, L. Stoichiometric vanadium oxides studied by XPS. *Surf. Interface Anal.* **44**, 1022–1025 (2012).

166. De Jesus, L. R., Horrocks, G. A., Liang, Y., Parija, A., Jaye, C., Wangoh, L., Wang, J., Fischer, D. A., Piper, L. F. J., Prendergast, D., and Banerjee, S. Mapping polaronic states and lithiation gradients in individual V_2O_5 nanowires. *Nat. Commun.* **7**, 12022 (2016).

167. Goodacre, D., Blum, M., Buechner, C., Hoek, H., Gericke, S., Jovic, V., Franklin, J., Kittiwatanakul, S., Söhnel, T., Bluhm, H., Smith, K. Water adsorption on vanadium oxide thin films in ambient relative humidity. *J. Chem. Phys.* **152**, 044715 (2020).

168. Gökce, H., and Bahçeli, S. Vibrational Analysis of Trimethylphenyl Ammonium Chloride. *Z. Naturforsch.* **64**, 127–131 (2009).

169. Hu, T., Feng, Z., Zhang, Y., Liu, Y., Sun, J., Zheng, J., Jiang, H., Wang, P., Dong, X., and Meng, C. "Double guarantee mechanism" of Ca^{2+}-intercalation and rGO-integration ensures hydrated vanadium oxide with high performance for aqueous zinc-ion batteries. *Inorg. Chem. Front.* **8**, 79–89 (2021).

170. Hu, T., Liu, Y., Zhang, Y., Chen, M., Zheng, J., Tang, J., Meng, C. 3D hierarchical porous $V_3O_7 \cdot H_2O$ nanobelts/CNT/reduced graphene oxide integrated composite with synergistic effect for supercapacitors with high capacitance and long cycling life. *J. Colloid Interface Sci.* **531**, 382–393 (2018).

171. O'Dwyer, C., Navas, D., Lavayen, V., Benavente, E., Santa Ana, M. A., González, G., Newcomb, S. B., and Sotomayor Torres, C. M. Nano-Urchin: The Formation and Structure of High-Density Spherical Clusters of Vanadium Oxide Nanotubes. *Chem. Mater.* **18**, 3016–3022 (2006).

172. Ruiz-Hitzky, E., and Casal, B. Interlayer adsorption of ammonia and pyridine in V_2O_5 xerogel. *J. Chem. Soc., Faraday Trans. 1* **82**, 1597–1604 (1986).

173. Soltane, L., and Sediri, F. Hydrothermal synthesis and characterization of mesoporous rod-like hybrid organic-inorganic nanocrystalline based vanadium oxide. *Ceram. Int.* **40**, 1531–1538 (2014).

174. Dong, J., Jiang, Y., Wei, Q., Tan, S., Xu, Y., Zhang, G., Liao, X., Yang, W., Li, Q., An, Q., and Mai, L. Strongly Coupled Pyridine- $V_2O_5 \cdot nH_2O$ Nanowires with Intercalation Pseudocapacitance and Stabilized Layer for High Energy Sodium Ion Capacitors. *Small* **15**, 1900379 (2019).

175. Xu, X., Qian, Y., Wang, C., Bai, Z., Wang, C., Song, M., Du, Y., *et al.* Enhanced charge transfer and reaction kinetics of vanadium pentoxide for zinc storage via nitrogen interstitial doping. *Chem. Eng. J.* **451**, 138770 (2023).

176. Occhiuzzi, M., Cordischi, D., and Dragone, R. Reactivity of some vanadium oxides: An EPR and XRD study. *J. Solid State Chem.* **178**, 1551–1558 (2005).

177. Zheng, Y., Yao, Z., Shadike, Z., Lei, M., Liu, J., and Li, C. Defect-Concentration-Mediated T-Nb_2O_5 Anodes for Durable and Fast-Charging Li-Ion Batteries. *Adv. Funct. Mater.* **32**, 2107060 (2022).

178. Eftekhari, A. Energy efficiency: a critically important but neglected factor in battery research. *Sustain. Energy Fuels* **1**, 2053–2060 (2017).

179. Wang, M., Zhang, J., Zhang, L., Li, J., Wang, W., Yang, Z., Zhang, L., Wang, Y., Chen, J., Huang, Y., Mitlin, D., and Li, X. Graphene-like Vanadium Oxygen Hydrate (VOH) Nanosheets Intercalated and Exfoliated by Polyaniline (PANI) for Aqueous Zinc-Ion Batteries (ZIBs). *ACS Appl. Mater. Interfaces* **12**, 31564–31574 (2020).

180. Zhu, K., Wu, T., and Huang, K. $NaCa_{0.6}V_6O_{16}\cdot 3H_2O$ as an Ultra-Stable Cathode for Zn-Ion Batteries: The Roles of Pre-Inserted Dual-Cations and Structural Water in V_3O_8 Layer. *Adv. Energy Mater.* **9**, 1901968 (2019).

181. Zhang, F., Sun, X., Du, M., Zhang, X., Dong, W., Sang, Y., Wang, J., Li, Y., Liu, H., and Wang, S. Weaker Interactions in Zn^{2+} and Organic Ion-pre-intercalated Vanadium Oxide toward Highly Reversible Zinc-ion Batteries. *Energy Environ. Mater.* **4**, 620–630 (2021).

182. Zhang, S., Chen, L., Dong, D., Kong, Y., Zhang, J., Liu, J., and Liu, Z. $A_mV_2O_5$ with Binary Phases as High-Performance Cathode Materials for Zinc-Ion Batteries: Effect of the Pre-Intercalated Cations A and Reversible Transformation of Coordination Polyhedra. *ACS Appl. Mater. Interfaces* **14**, 24415–24424 (2022).

183. Feng, B., Sun, D., Wang, H., Tan, S., and Zhang, H. A simple method for the synthesis of $KV_3O_8\cdot 0.42H_2O$ nanorod and its lithium insertion/deinsertion properties. *Int. J. Electrochem. Sci.* **8**, 1095–1102 (2013).

184. Bin, D., Huo, W., Yuan, Y., Huang, J., Liu, Y., Zhang, Y., Dong, F., Wang Y., and Xia, Y. Organic-Inorganic-Induced Polymer Intercalation into Layered Composites for Aqueous Zinc-Ion Battery. *Chem.* **6**, 968–984 (2020).

185. Zavalij, P. Y., and Whittingham M. S. Structural chemistry of vanadium oxides with open frameworks. *Acta Crystallogr. B* **55**, 627–663 (1999).

186. Verma, V., Kumar, S., Manalastas Jr., S., Zhao, J., Chua, R., Meng, S., Kidkhunthod, P., and Srinivasan, M. Layered $VOPO_4$ as a Cathode Material for Rechargeable Zinc-Ion Battery: Effect of Polypyrrole Intercalation in the Host and Water Concentration in the Electrolyte. *ACS Appl. Energy Mater.* **2**, 8667–8674 (2019).

187. Lai, J., Zhu, H., Zhu, X., Koritala, H., and Wang, Y. Interlayer-Expanded $V_6O_{13}\cdot nH_2O$ Architecture Constructed for an Advanced Rechargeable Aqueous Zinc-Ion Battery. *ACS Appl. Energy Mater.* **2**, 1988–1996 (2019).

188. Du, M., Liu, C., Zhang, F., Dong, W., Zhang, X., Sang, Y., Wang, J., Guo, Y., Liu, H., and Wang S. Tunable Layered $(Na,Mn)V_8O_{20}\cdot nH_2O$ Cathode Material for High-Performance Aqueous Zinc Ion Batteries. *Adv. Sci.* **7**, 2000083 (2020).

189. Mar, L. G., Timbrell, P. Y., and Lamb, R. N. An XPS study of zinc oxide thin film growth on copper using zinc acetate as a precursor. *Thin Solid Films* **223**, 341–347 (1993).

190. Liang, H., Cao, Z., Ming, F., Zhang, W., Anjum, D. H., Cui, Y., Cavallo, L., and Alshareef, H. N. Aqueous Zinc-Ion Storage in MoS_2 by Tuning the Intercalation Energy. *Nano Lett.* **19**, 3199–3206 (2019).

191. Ye, J., Li, P., Zhang, H., Song, Z., Fan, T., Zhang, W., Tian, J., Huang, T., Qian, Y., Hou, Z., Shpigel, N., Chen, L., and Dou, S. Manipulating Oxygen Vacancies to Spur Ion Kinetics in V_2O_5 Structures for Superior Aqueous Zinc-Ion Batteries. *Adv. Funct. Mater.* **33**, 2305659 (2023).

192. Leng, W., Liu, X., and Gong, Y. Chromium vanadate with unsaturated coordination sites for high-performance zinc-ion battery. *Chem. Eng. J.* **431**, 134034 (2022).

193. Feng, Z., Sun, J., Liu, Y., Jiang, H., Hu, T., Cui, M., Tian, F., Meng, C., and Zhang, Y. Polypyrrole-intercalation tuning lamellar structure of $V_2O_5{\cdot}nH_2O$ boosts fast zinc-ion kinetics for aqueous zinc-ion battery. *J. Power Sources* **536**, 231489 (2022).

194. Zheng, J., Liu, C., Tian, M., Jia, X., Jahrman, E. P., Seidler, G. T., Zhang, S., Liu, Y., Zhang, Y., Meng, C., Cao., G. Fast and reversible zinc ion intercalation in Al-ion modified hydrated vanadate. *Nano Energy* **70**, 104519 (2020).

195. Sun, W., Wang, F., Hou, S., Yang, C., Fan, X., Ma, Z., Gao, T., Han, F., Hu, R., Zhu, M., and Wang, C. Zn/MnO2 Battery Chemistry with H^+ and Zn^{2+} Coinsertion. *J. Am. Chem. Soc.* **139**, 9775–9778 (2017).

196. Hwang, J., Ejsmont, A., Freund, R., Goscianska, J., Schmidt, B. V. K. J., and Wuttke, S. Controlling the morphology of metal–organic frameworks and porous carbon materials: metal oxides as primary architecture-directing agents. *Chem. Soc. Rev.* **49**, 3348–3422 (2020).

197. Cabana, A., and Sandorfy, C. The infrared spectra of solid methylammonium halides. *Spectrochimica Acta* **18**, 843–861 (1962).

198. Bukleski, M., Dimitrovska-Lazova, S., and Aleksovska, S. Vibrational spectra of methylammonium iodide and formamidinium iodide in a wide temperature range. *Maced. J. Chem. Chem. Eng.* **38**, 237–252 (2019).

199. Ouasri, A., Rhandour, A., Dhamelincourt, M. C., Dhamelincourt, P., and Mazzah, A. Vibrational study of $(CH_3)_4NSbCl_6$ and $[(CH_3)_4N]_2SiF_6$. *Spectrochim. Acta. A Mol. Biomol. Spectrosc.* **58**, 2779–2788 (2002).

200. Bottger, G. L., and Geddes, A. L. The infrared spectra of the crystalline tetramethylammonium halides. *Spectrochimica Acta* **21**, 1701–1708 (1965).

201. Bozkurt, E., Ucar, I., Kartal, I., Karabulut, B., and Bekdemir, Y. Structural, spectroscopic and EPR studies of tetraethylammonium tetramethylammonium tetrabomocuprate (II) complex. *Z. Kristallogr. Cryst. Mater.* **224**, 163–168 (2009).

202. Qian, A., Zhuo, K., Shin, M. S., Chun, W. W., Choi, B. N., and Chung, C.H. Surfactant Effects on the Morphology and Pseudocapacitive Behavior of $V_2O_5{\cdot}nH_2O$. *ChemSusChem* **8**, 2399–2406 (2015).

203. Sanchez, C., Livage, J., and Lucazeau, G. Infrared and Raman study of amorphous V_2O_5. *J. Raman Spectrosc.* **12**, 68–72 (1982).

204. Šurca, A., and Orel, B. IR spectroscopy of crystalline V_2O_5 films in different stages of lithiation. *Electrochim Acta* **44**, 3051–3057 (1999).

205. O'Dwyer, C., Lavayen, V., Newcomb, S. B., Santa Ana, M. A., Benavente, E., González, G., and Sotomayor Torres, C. M. Vanadate Conformation Variations in Vanadium Pentoxide Nanostructures. *J. Electrochem. Soc.* **154**, K29 (2007).

206. Zhou, X., Wu, G., Wu, J., Yang, H., Wang, J., Gao, G., Cai, R., and Yan, Q. Multiwalled carbon nanotubes–V_2O_5 integrated composite with nanosized architecture as a cathode material for high performance lithium ion batteries. *J. Mater. Chem. A Mater.* **1**, 15459–15468 (2013).

207. Barbosa, G. N., Graeff, C. F. O., ans Oliveira, H. P. Thermal annealing effects on vanadium pentoxide xerogel films. *Eclética Química* **30**, 7–15 (2005).

208. Inagaki, M., Nakamura, T., and Shimizu, A. Soft process for the intercalation of ammonium cations into vanadium oxide. *J. Mater. Res.* **13**, 896–900 (1998).

209. Frankcombe, T. J., and Liu, Y. Interpretation of Oxygen 1s X-ray Photoelectron Spectroscopy of ZnO. *Chem. Mater.* **35**, 5468–5474 (2023).

210. Bondarenka, V., Grebinskij, S., Mickevičius, S., Tvardauskas, H., and Kačiulis, S. Determination of vanadium valence in hydrated compounds. *J. Alloys Compd.* **382**, 239–243 (2004).

VITA

Education Background:

Doctor of Philosophy: Materials Science and Engineering	University of Washington
	2019/09 – 2024/06
Master of Science: Materials Science and Engineering	University of Washington
	2017/09– 2019/03
Master of Science: Advanced Engineering Materials	University of Manchester
	2014/09 –2015/11
Bachelor of Engineering: Materials Forming and Control Engineering	Northeastern University
	2010/08 –2014/06